POLITECNICO DI TORINO
Master's Degree in Civil Engineering

Structural Health Monitoring using innovative smart devices: numerical and experimental study

Master's Thesis
23th July 2020

Supervisor:
Prof. Francesco Tondolo

Candidate:
Claudio Bandinelli

Table of contents

List of Figures

Abstract

Structural health monitoring is increasingly required in the field of infrastructure, both because standards expressly require it and because current guidelines for bridge maintenance and monitoring refer to it for existing works. Indeed, a perspective approach to functional materials and structures pushes toward monitoring systems effective since the construction stages and up to its end of life. Monitoring systems are divided into two main groups: those embedded into the structure and those attached superficially to the structure. The first one, being inside the structure, are better protected, but difficult to replace in case of damage; the latter are subject to external environmental aggression, but easy to replace. Currently, new structural health monitoring systems are under continuous development to detect stresses inside the structures, in order to have accurate, easy to install and low-cost tools. One of these new technologies is the "S3 System" (Tondolo, 2016), which is currently under study; it is a system embedded in the structure, which consists of a reinforcement steel bar in which a sealed cavity filled with a fluid is made. This cavity hosts a low-cost MEMS (Micro Electro-Mechanical Systems) sensor, able to measure pressure and temperature variation, with which it is possible to calculate the volume variation of the cavity itself, that is correlated to the axial deformation of the bar. Along this master's thesis, the work carried out in previous studies (Battistoni, 2018) was continued and implemented, where the "smart" reinforcing bar instrumented with this technology was modeled with finite element software, with the aim of investigating the operation of the "S3 System" and the behavior of the integrated reinforcing bar together with the measuring instrument and the relative machining necessary for its insertion. A campaign of experimental tests was also carried out on a "smart" bar, equipped with sensors of the "S3 System", carrying out long-term monitoring of pressure and temperature, where, through the processing of experimental data, the theoretical assumptions could be verified. From the results of this work, in the future studies may lead to a more effective design to improve the global system. Currently there is a demand for this instrument for geotechnical works such as tunnels, but the studies have confirmed the validity of this new smart technology, which in the future could become an automatically integrated system for any type of structure.

Riassunto

Il monitoraggio strutturale è sempre più richiesto nell'ambito delle infrastrutture, sia perché le norme lo richiedono espressamente, sia perché le attuali linee guida per la manutenzione e il monitoraggio di ponti ne fanno riferimento per le opere esistenti. Infatti, un approccio prospettico ai materiali e alle strutture funzionali spinge verso sistemi di monitoraggio efficaci sin dalle fasi di costruzione e fino alla fine del ciclo di vita. I sistemi di monitoraggio si distinguono in due grandi gruppi: quelli incorporati nella struttura e quelli attaccati superficialmente alla struttura. I primi essendo all'interno della struttura stessa sono più protetti, ma di difficile sostituzione in caso di danneggiamento; i secondi invece, sono soggetti ad aggressioni ambientali esterne, ma con semplicità di sostituzione. Attualmente sono in continuo sviluppo nuovi sistemi di monitoraggio strutturale per rilevare le sollecitazioni interne alle strutture, con il fine di avere strumenti accurati, di facile installazione e basso costo. Una di questa nuove tecnologie è il "Sistema S3" (Tondolo, 2016), che attualmente è sotto studio; è un sistema incorporato nella struttura, che consiste in una barra d'armatura di acciaio, nella quale viene realizzata una cavità sigillata riempita con un fluido. Tale cavità ospita un sensore MEMS (Micro Electro-Mechanical Systems) di basso costo, in grado di misurare la variazione di pressione e temperatura, con le quali è possibile risalire alla variazione di volume della cavità stessa che è correlata alla deformazione assiale della barra. Durante questa tesi magistrale è stato proseguito e implementato il lavoro effettuato negli studi precedenti (Battistoni, 2018), dove la barra di armatura "smart" strumentata con questa tecnologia è stata modellata con un software agli elementi finiti, con il fine di investigare il funzionamento del "Sistema S3" ed il comportamento della barra d'armatura integrata insieme allo strumento di misura con le relative lavorazioni necessarie al suo inserimento. È stata anche realizzata una campagna di prove sperimentali su una barra "smart", strumentata con sensori del "Sistema S3", effettuando un monitoraggio di lungo periodo su pressione e temperatura, dove tramite l'elaborazione dei dati sperimentali si sono potute verificare le assunzioni teoriche. Dai risultati di questo lavoro, gli studi successivi potranno portare ad una progettazione più efficace, per migliorare il sistema globale. Attualmente c'è richiesta di questo strumento per opere di tipo geotecnico come gallerie, ma dagli studi effettuati si conferma la validità di questa nuova tecnologia, che in un futuro potrebbe diventare un sistema integrato automaticamente in un qualsiasi tipo di struttura.

Introduction

The common structures such as bridges, dams, buildings and so on, during the service period, are influenced from the coupling effect of load fatigue, environment corrosion and material aging will lead to the cumulative damage and the resistance decay. These problems can reduce the ability to resist catastrophes, which in the last decades have been hit a lot of geographic part of the world; for these motivation and because the heritage of old important structure are present in different country, the public opinion push to turn the attention to the delicate concept of structural health.

Traditionally the structural health assessment has been performed with visual inspection or by information measured using portable device, but with their problems and poor information about the structure, there is the needed to improve this technique. Under this circumstance, since the 1980s, structural health monitoring technology has gradually expanded from the aviation, aerospace and mechanical fields to civil engineering.

For this, the structural health monitoring is getting one of the most important innovative part of the civil engineering, where the theory research met the new smart technologies.

A monitoring system has three basic components: a sensor system; a data processing system, including data acquisition, transmission and storage; and, finally, a system for evaluating the health of the structure, including analysis techniques and algorithms that allow specific assessments to be made of the state of the structure based on the measured data. So, the goal of the SHM is to understand the current situation of the structure, doing a long-period monitoring. Is possible to do two type of monitoring system: permanent monitoring that represents a system on the target structure that continuously collect data and the periodic monitoring that represents the installation of a sensor network recording the physical and mechanical parameters, but only for a limited time. The current monitoring systems can embed in the structure or attached superficially on the structure. The first one has a better protection but are difficult to replace in case of damage, the second one is subjected to harsh environment but easy to replace. The trend is to have a permanent monitoring to control the entirely life of the structure.

In the first chapter are summary the currently innovative smart devices able to use in structural health monitoring. Big part of these devices is under laboratory study.

One of these smart technologies is the "S3 system" (Tondolo, 2016), which is currently under development and it is object of the studies along this thesis. This new technology is an embedded system able to do a permanent monitoring on the new and/or existing structures. The measurement units are integrated inside the reinforcement bars and they are able to detect the steel deformations.

The smart steel bar is modelled with a F.E.M. software in order to investigate the S3 system functioning and the behaviour of the reinforcement bar integrated with the measurement unit. Different models are built, and the “smart” bar has been subjected to a mechanical action and temperature effect to catch its behaviour. Numerical results are compared with the experimental data obtained by campaign carried out on steel bars equipped with “S3 System” in a non-controlled environment.

Chapter 1
1. Structural Health Monitoring in Civil Engineering

Structural health monitoring (SHM) is increasingly applied worldwide both on existing structures, to allow for a continuous assessment of their quality and reliability and on new structures to control the construction process and the design assumption. In particular, the goals for the new structures is to integrate the monitoring system inside the structures as for geotechnical works; but in the latter, this monitoring system is used exclusively in the construction phase until the testing; the trend is to make the structures are monitored even beyond and that the both instrumentation used for the construction process can continue its work during the structure's life-time, rather than imagine a monitoring architecture system that must be post-installed at the end of construction phases.

Especially the concrete structure that are continuously exposure to severe conditions associated with the environment, loading, effects of aggressive actions, corrosion of embedded metal, frost, overload, concretes resistance to volume changes, abrasion/erosion, and chemical actions that may deteriorate the concrete infrastructure.
Concrete is the second most consumed material on the earth, provides constructing of durable, affordable, functional and attractive structures from buildings to roads, runways, bridges, dams, tunnels, and sewage systems. But the deterioration problem can occur during his whole life cycle, change a lot of physical parameters such as pressure, load, humidity and temperature.
Thus, monitoring the concrete structure should be the right choice to maintain the properly work of infrastructure and can save huge amounts of capital. The main parameters that should be monitored are:

- Temperature;
- Humidity;
- Corrosion rate:
- pH;
- Strain/stress/crack;

These five key parameters play an important role in structural safety as well as the long-term durability, sustainability, and strength of an infrastructure. Reach extreme values of these parameters can contribute to structural failure (Taheri, 2019).
Monitoring these parameters, can help to identify the source and the level of damage.
Structural health monitoring of concrete can be performed using destructive and non-destructive methods.

- Destructive techniques, such as chemical analysis, necessitate sample extraction and preparation. They are time-consuming, expensive, and provide results only after laboratory investigation.
- Non-destructive techniques (NDT) including the Rebound hammer test, acoustic emission, and ultrasonic inspection, are easier, more economical, and can provide results without the need for sample extraction.

In the last years are developing a lot of number of new devices to monitoring the structures; SHM evaluation technologies can be classified into five levels based on their performance and degree of complexity, as illustrated in the following figure. Many NDT evaluations, including ultrasonic inspection, which support only the detection of local-based damages (such as crack detection) can be classified as level I or II. Sensors, depending on their working principle, can be classified into level II to level V. Smart composites, self-sealing concrete and smart structures are classified into level IV and V. These technologies are still under developing, but they are expected to become the future of SHM (Taheri, 2019).

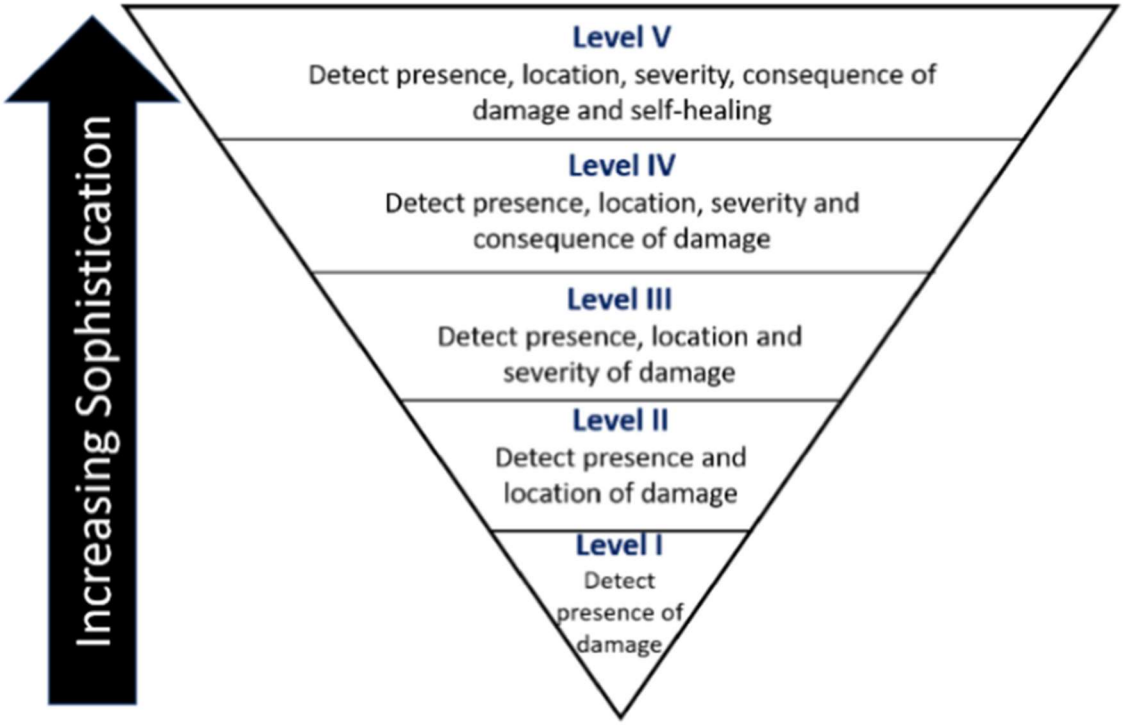

Fig. 1: SHM classification based on their performance and degree of complexity

How can we have seen above, monitoring a structure could be done with different method and technique. But the main different about the functionally of device's monitoring is if they do a permanent or periodic monitoring. We know that there are many tools that are used for both monitoring, but the main different is the approach of the monitoring system.

The permanent monitoring represents a system on the target structure that continuously collect data about physical and mechanical parameters to assess the structure condition in operation. The basis and the main advantage of this system is the possibility of integrating automated data processing procedures able to process, even in real time, so to understand when there is something of unexpected and/or abnormal conditions in the structural behavior. In particular, when happen the natural catastrophe events, such as earthquakes or floods, can be assessed either in near real time for emergency management, or for diagnostic and maintenance purposes. The big problem about that is the high effective cost, the complex design and in particular to control the large volumes of data that must be process (Rainieri, 2019).

The periodic monitoring represents the installation of a sensor network recording the physical and mechanical parameters, but only for a limited time, such as few hours to some weeks, obviously depending on the objective of the assessment. This is a no real safety valuation of the structure, but can provide data and information that, complemented by visual inspections, can effectively support the assessment of the structural health. The same measurement system used for monitoring can be installed on a different structure, so distributing its overall cost on a large number of applications (Rainieri, 2019).

1.1 Classic monitoring system

In this part, we will see the main classic monitoring systems, that are of common use to measure the physical and mechanical parameters of the interest structures.

1.1.1 Vibrating wire sensor

Vibrating wire sensors are a class of sensors that are very popular in geotechnical and structural monitoring.

The structure of the sensor is composed by a tensioned steel wire, hermetically sealed, that is coupled with an electromagnetic coil. When the external force is applied on the instrument, happened a change of tension inside the wire that of consequence change the wire's resonant frequency, that it is read by electro-magnet. This mechanism is used in a variety of sensor configurations to measure static strain, stress, pressure, tilt, and displacement.

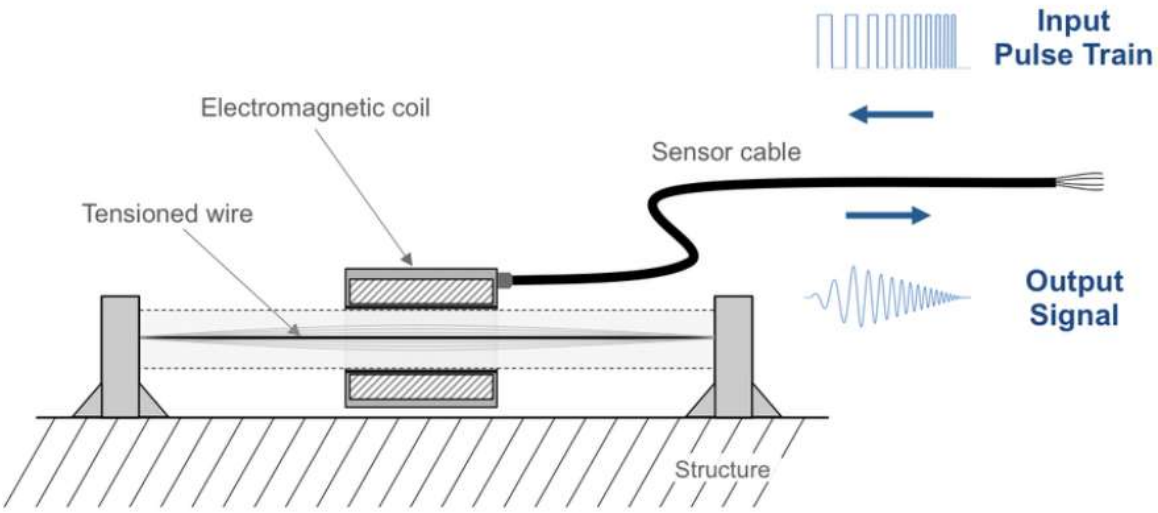

Fig. 2: Basic operation of Vibrating Wire Sensor

1.1.2 Linear variable differential transformer (LVDT)

LVDT is one of the most common devices installed in the construction sector for measuring relative displacements.

The transducer is composed by a hollow metal tube containing three windings arranged with parallel axes and with a mobile ferromagnetic cylindrical core inside.
The central winding is called primary and the others are called secondary. The primary one is connected to an AC voltage generator, while the output voltage is measured at the ends of the secondary ones. The coils are an electrical signal according to the position of the mobile core inside, practically its operating principle is that of mutual inductance.

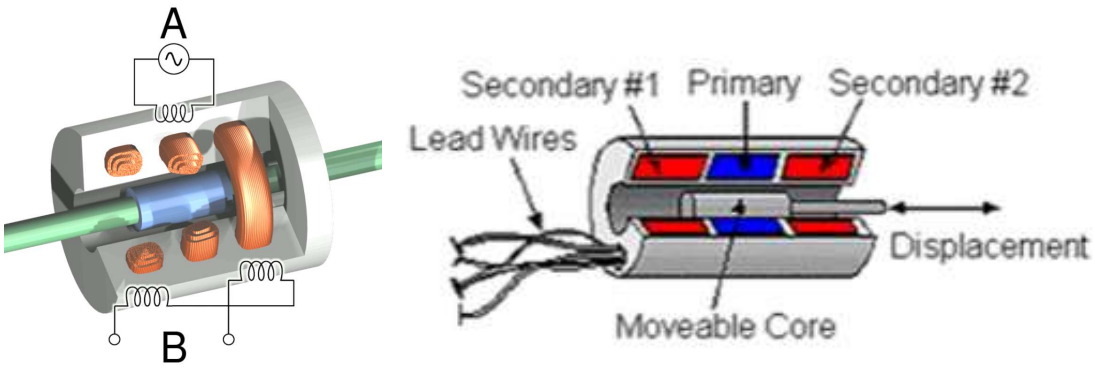

Fig. 3: Section of LVDT device

1.1.3 Metallic Strain gauge

Metallic Strain gauge is one of the most famous devices to measure the strain, in a lot of engineering fields. The gauge is attached to the object, whose we want measures the deformation, with a suitable adhesive.

When the object is deforming, the foil follows the object, and it deforms as well. So, the elastic deformation is measure thanks to the variation of the electrical resistance of the device.
An important parameter is the sensitivity to strain, expressed by the gauge factor GF, that is the ratio of the fractional change in electrical resistance to the fractional change in strain; this value is usually around 2 (Battistoni, 2018).

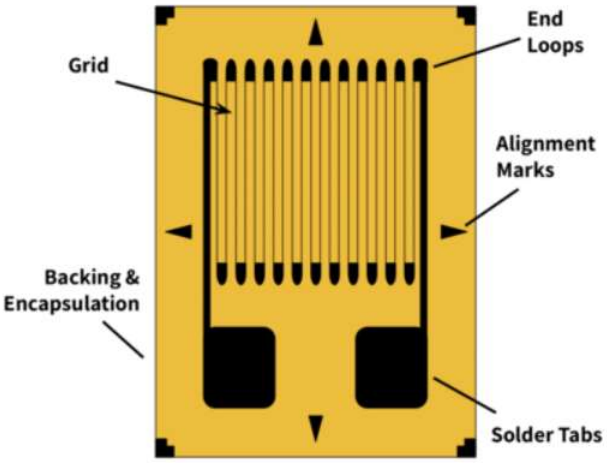

Fig. 4: Metallic Strain Gauge Diagram

The variation of electrical resistance is usually measured using a Wheatstone bridge that is composed by four resistive arms with an excitation voltage VEX, that is applied across the bridge. Due to of the active element in the Wheatstone bridge, the orientation of the strain gages and the type of measured strain, is possible to have three types of strain gage configuration: quarte, half and full-bridge strain gauge (Battistoni, 2018).

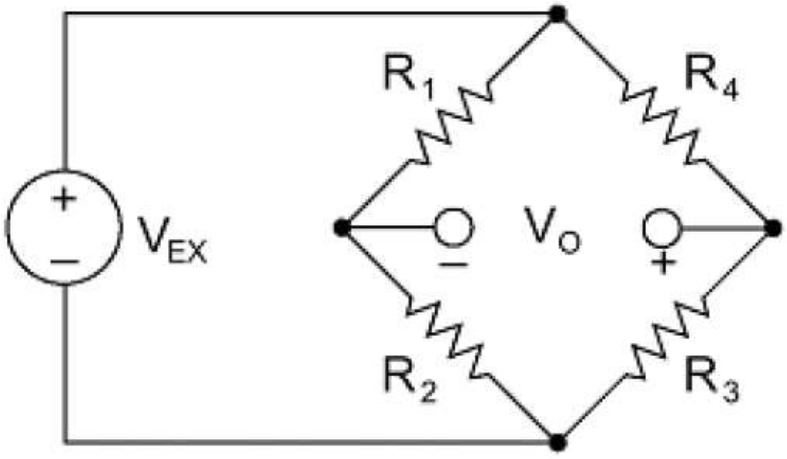

Fig. 5: Wheatstone Bridge circuit

1.1.4 Fiber optical sensor

In the last years, there are many areas where is expected to occur a rapid growth of fiber optics sensors applications. From the world of medical instrumentation, telecommunications and aerospace to structural health monitoring and damage assessment systems in civil structures. The fiber optical technologies are one of the fastest growing areas in SHM and are of the common use in this sector.

As is possible to see from the following figure, the fiber optical sensor are divide in three big categorized due to of type of technologies: Grating-based sensor, Interferometric sensor and Distributed sensor.

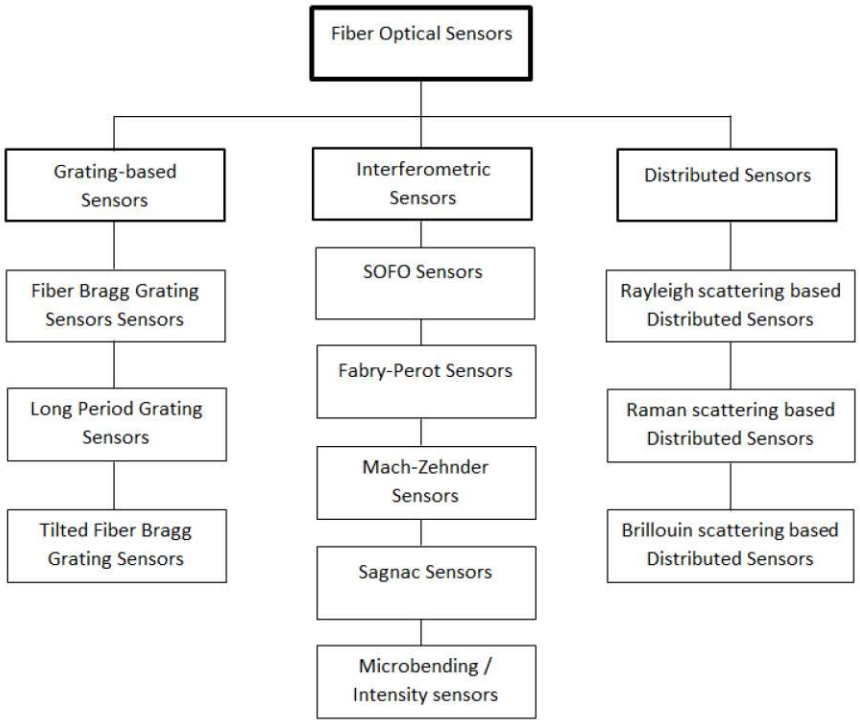

Fig. 6: Overview of fiber optic sensor technologies

Each typology has different characteristic and functionality; in the follow subchapter we will see, how this different sensor works, and which are the most common in civil engineering monitoring applications, with some device example.

1.1.4.1 Interferometric sensor

It is created by an intrinsic or extrinsic interferometric cavity along an optical path. Physical changes in structures are reflected by the changes of the optical phase difference between two interference light waves. The most common instruments used in the structural health monitoring are SOFO interferometric sensor and Fabry-Perot interferometric sensor.

The Fabry-Perot is a point sensor, very similar to a conventional sensor like a vibration wire. Measuring something at one location and the optical fiber is a wire that bring the light from the instrument to the sensor, the sensor modifies the light and then we send it back to the instrument. So, the fiber is only uses as a way of transmitting the data (Inaudi, 2017). Fabry-Perot interferometric sensors follow the Fabry-Perot interferometry principle which is based on a cavity, because there is an air gap between two fiber that are really close and when the light goes into the fiber, one part of the light will be reflected by the first mirror and another part of the light will be reflected by second mirror. The interference shifts the model based on the change in the optical path and depending on the length of the FP cavity. The length can be affected by pressure change and temperature change (e.g. environmental change) (Dutta, 2019).

For FPI sensors, the intensity of the interference signal I is given by the following formulation:

$$I = 2 \cdot I_1 \cdot I_2 \cdot \sqrt{I_1 \cdot I_2} \cdot \cos(4\pi Z / \lambda + \varphi)$$

- I_1 and I_2 are the reflection at the reflection interfaces of the cavity;
- φ the initial phase of the interference;
- λ is the optical wavelength;
- Z is the difference of the optical path;

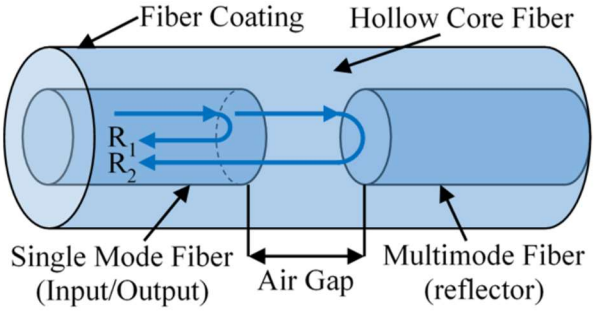

Fig. 7: Working principle of FPI Sensor

One famous technology is the of the common “is the Extrinsic Fabry-Perot Interfermoter (EFPI) that is constituted by a capillary silica tube containing two cleaved optical fibres facing each other, but leaving an air gap of a few microns or tens of microns between them" (Battistoni, 2018).
This sensor is a 70 mm long with 12.5 mm of diameter and it is designed to be embedded in concrete (Smartec, 2020).

Fig. 8: EFPI Strain transducer by Smartec

In the following picture is possible to see the main specification of the EFPI sensor.

Range	±1500 με (other ranges available upon request)
Resolution	0.01% F.S.
Operating temperature	−40 to +55°C, operating temperature is fiber optic cable dependent
EMI/RFI susceptibility	Intrinsic immunity
Gauge dimensions Diameter Length	 12.5 mm 70 mm
Fiber optic cable	CFF-UD3-1F
Connector	ST

Fig. 9: Technical specification of EFPI Strain transducer by Smartec

Another example of this technology is a gauge made with fiber optical cable with a miniature Fabry-Perot strain sensor. The Fabry-Perot is embedded into a composite carbon fiber to get a very stable sensor. It allows both static and dynamic measurement (Geokon, 2020).

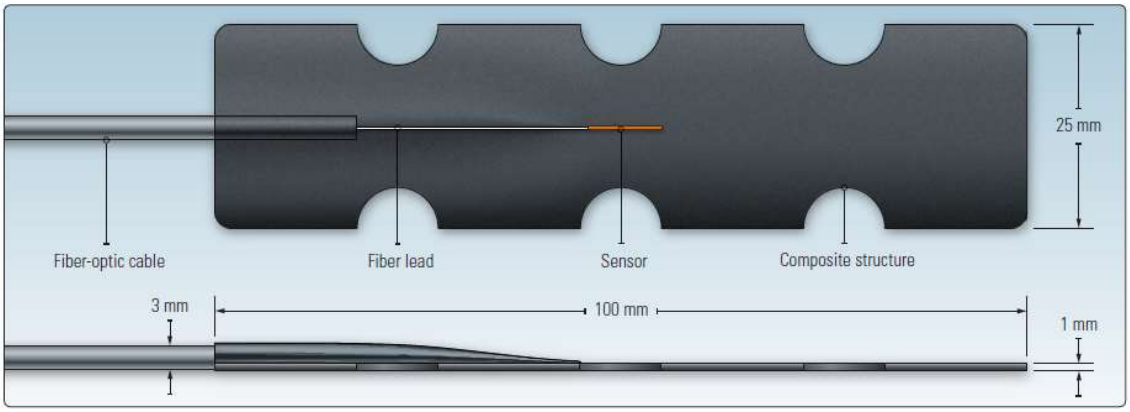

Fig. 10: Model FP4000 Fiber Optic Strain Gauge by Geokon

In the following picture is possible to see the main specifications of this miniature Fabry-Perot strain sensor.

	FP4000-1.0	FP4000-2.5	FP4000-5.0
Standard Ranges	−1000 to +1000 με	−2500 to +2500 με	−5000 to +5000 με
Resolution	0.15 με	0.30 με	0.50 με
Gauge Factor Accuracy[1]	±3% F.S.	±3% F.S.	±10% F.S.
Temperature Sensitivity	0.85-1.22 με/°C		
Transverse Strain Sensitivity	transverse strain insensitive		
Temperature Operating Range	−40 °C to +80 °C		
EMI/RFI Susceptibility	complete immunity		
Cable Length[2]	1.5 m (standard)		
Optical Connector	SC (standard)		
Signal Conditioner Compatibility	all Opsens WLPI signal conditioners		
L × W × H	100 × 25 × 1 mm		

Fig. 11: Technical specification of Model FP FP4000 Fiber Optic Strain Gauge by Geokon

SOFO interferometric sensors are the most successful low coherent interferometric sensors for SHM and are long gauge fiber optic sensors. In this case the fiber itself become the sensor (Inaudi, 2017).
The classic SOFO sensor is composed by two part: an active and passive one. The active part consists of the reference and the measurement fiber and it able to measure the deformation between its two anchors; the distance of these two points, can close 25 centimeters or as far as 10 meters apart.
Instead, the passive part is insensitive to a deformation, because it is used to connect the sensor to the reading unit. It is temperature insensitivity, high precision and stability (Smartec, 2020).

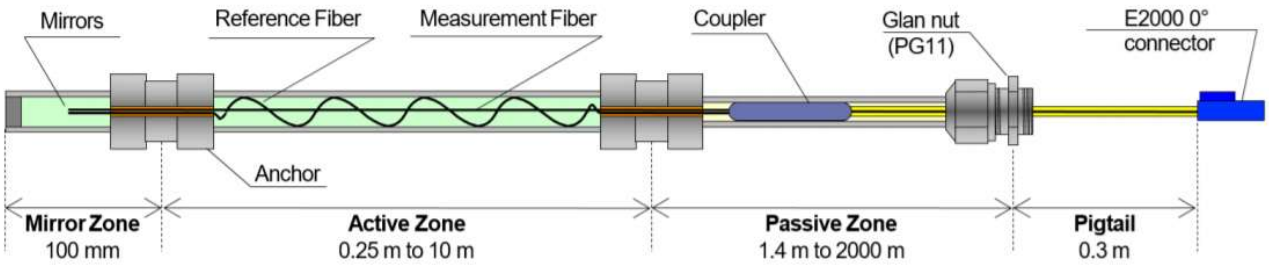

Fig. 12: SOFO Deformation Sensor by Smartec

In the following picture is possible to see the main specifications of the SOFO sensor.

Length of active zone (LA, measurement basis):	25 cm to 10 m, standard lengths
Length of passive zone (connecting cable):	1 m to 100 m Customized lengths up to 2000 m upon request
Measurement range:	0.5% of LA in shortening, 1% of LA in elongation
Measurement precision:	0.2% of the measured deformation or better
Measurement resolution:	2 µm RMS
Connecting cable protection options (see specific datasheet for details):	Standard (recommended for embedding or surface mounting in normal conditions) Stainless steel protecting tube (recommended in harsh conditions) Simple cable without protecting tube (recommended for laboratory conditions)
Operating temperature:	Standard active zone: -50 °C to +110 °C Special active zone (upon request): -50 °C to +170 °C Passive zone: -40 °C to +80 °C
Waterproof:	5 bars (15 bars with extra protection on anchoring points)
Calibration:	Not required

Fig. 13: Technical specification of SOFO Deformation Sensor by Smartec

1.1.4.2 Grating-based Sensors

The most uses sensor is the Fiber Bragg Grating (FBG) sensor, that has some discrete location where is possible to get the sensing and the fiber connect those locations, back to the instrument; for this, it is a classified as quasi-distributed sensor. So, we have many points sensor along the length of the fiber. It is relatively similar to Fabry-Perot like working, but we have a multiple sensor (Inaudi, 2017).

Fiber optic sensors consist of different refractive indices in the fiber core. It acts as a mirror that reflects light for a specific wavelength (λ_B). Wavelengths other than λ_B are not reflected. Therefore, it can be assumed that as the refractive index inside the fiber core changes, the reflected wavelength changes. The bragg grating acts as a deformation calculation sensor when attached to a structure because the structure transmits its deformation to the optical fiber by changing the grating pitch and causing the reflected wavelength to change. By analyzing the reflected wavelength, it is possible to trace the deformations themselves. As we have already said, the variation of the refractive index of the fiber core makes a certain wavelength λ_B reflect. Any variation of the refractive index along the optical path of light causes a small reflection by it. This happens at each line of the periodic structure imprinted in the core (Dutta, 2019).
The wavelength λ_B can be calculated with the follow formulation:

$$\lambda_B = 2 * n_{eff} * \Lambda$$

- n_{eff} : index of refraction
- Λ: grating period

Instead the variation of the wavelength of Bragg Grating can be obtain with the follow equation:

$$\Delta\lambda_B = \lambda_B * [(\alpha + \xi)\Delta T + (1 - p_e) * \Delta\varepsilon]$$

- $\Delta\varepsilon$: strain variation;
- ΔT: temperature change;
- α: coefficient of the thermal expansion;
- ξ: thermooptic coefficient;
- p_e: strain-optic coefficient;

It should be noted that the reflected wavelength also varies as a function of temperature due to the expansion of the glass of which the fiber itself is made and the variation in the refractive index. Therefore, it can be used to measure the temperature variation, but if it has a high incidence, a calibration will be needed for the subsequent calculation of the deformations.

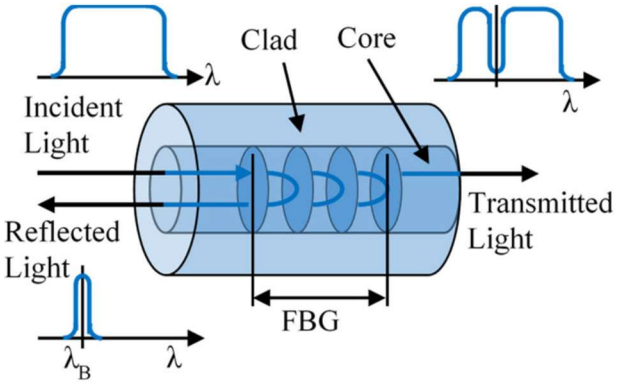

Fig. 14: Working principle of FBG Sensor

One FBG device is The MuST FBG deformation sensor that it is a transducer able to transform the static or dynamic distance variation into a change of reflected wavelength. It is built with two part: an active part and passive one. The active part is made to measure the deformation between its two ends, transforming this deformation into a wavelength shift of the Fiber Bragg Grating. The passive part is used only to connect the active part to a reading unit. The sensor is available in single-end, double-end and chained configuration. It is possible to embed the sensor inside the concrete or surface mounted.

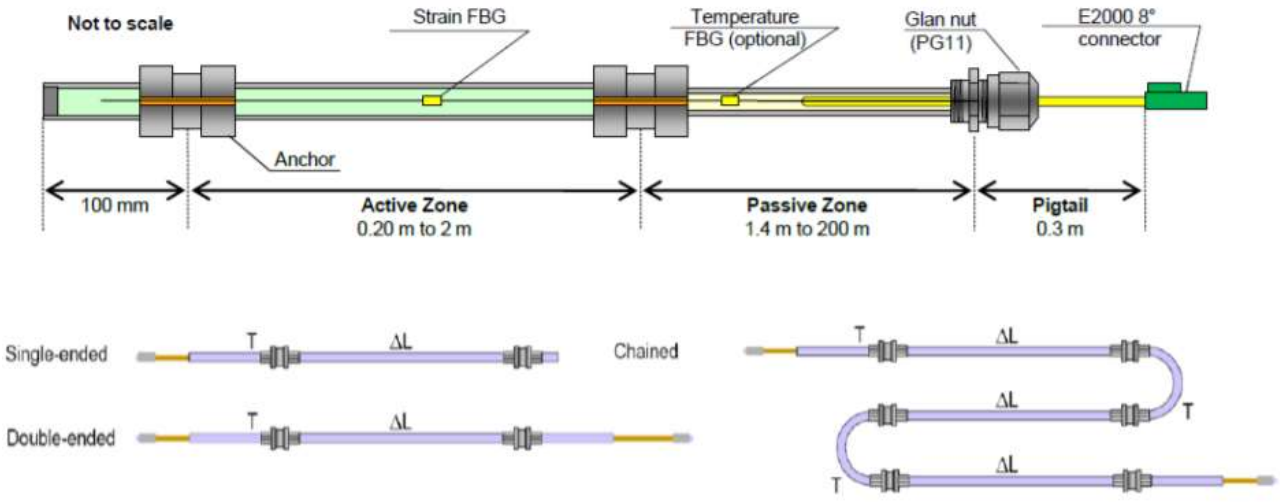

Fig. 15: The MuST FBG deformation sensor by Smartec

In the following picture is possible to see the main specifications of the FBG sensor.

Length of active zone (LA, measurement basis):	20 cm to 2m
Length of passive zone (connecting cable):	1 to 200 m (longer distances available on request)
Pre-tensioning of the measurement fiber:	0.5% of the length of active zone (others on special request)
Measurement range:	Strain: 0.5 % in shortening, 0.75 % in elongation Temperature: -40 °C to +80 °C
Measurement resolution/ Accuracy:	0,2 με / 2 με (using SMARTEC Reading Units)
Connecting cable protection options (see specific datasheet for details):	Standard cable: Gray (for embedding or surface mounting in normal conditions) Stainless steel reinforced cable: Black (recommended in harsh conditions) Simple unprotected cable: Yellow (only for laboratory conditions)
Optical connectors:	E-2000 AC (8°)
Operating temperature:	Passive zone: -40 °C to +80 °C Standard active zone: -50 °C to +110 °C Special active zone (upon request): -50 °C to +170 °C
Waterproof:	5 bars (15 bars with extra protection on anchoring points)

Fig. 16: Technical specification of The MuST FBG deformation sensor by Smartec

1.1.4.3 Distributed sensor

Disturbed sensor is able to measure the strain and temperature from every meter along the fiber. The measurement principle is relatively simple, because the light goes down an optical fiber at the given wavelength (λ_0); most of the light will simply travel through the fiber, but there is always at every location along the fiber a very small amount of light that gets scattered with the glass and gets diffused; part of that light comes back in towards the source of the light itself and during the analyse of data is possible to find, the original wavelength (λ_0) with new components that contain information about the temperature and the strain in the location where the scattering occurred. It is possible to understand the point where the scattering occurs with an post technique that measuring the time of the flight of the returned pulses (Inaudi, 2017).

There are many technologies, which have the capability to catch backscattering components and to transform them in strain or temperature measurements; the main common are the optical time domain reflectometry and optical time domain analysis technologies and they are commonly based on Brillouin scattering (BOTDR and BOTDA) or on Raylegh scattering (OTDR), while Raman scattering can be used only for temperature measurements (Battistoni, 2018).

On example for strain measurement is the SMARTape strain sensor, that using Brillouin scattering (BOTDR/BOTDA) to monitoring the deformation over long distances. The SMARTape sensor consists of a single mode optical fiber embedded in a Glass Fiber Reinforced Polymer / Epoxy tape. It is designed to be embedded or used for surface installation on smooth surface. It can resist in harsh environment and often used in civil and Oil&Gas engineering applications (Smartec, 2020).

Fig. 17: SMARTape strain sensor by Smartec

In the following picture is possible to see the main specifications of the SMARTape sensor with his dimension in the transversal section.

Temperature compensation:	not compensated
Calibration:	during production
Strain range:	max. -1 % compression to +1 % elongation (depending on installation manner)
Maximal length:	~ 800 m / reel , more upon request
Dimensions (W x H):	~ 9.90 mm x 0.32 mm
Weight:	~ 3.8 kg/km
Tensile strength:	≥ 400 MPa (ASTM D3916)
Elongation at break:	≥ 2.5 % (ASTM D3916)
Min bending radius:	~ 100 mm operating in long-term ~ 50 mm installation and storage
Hydrostatic pressure:	$3x10^7$ kPa (300 bars)
Fiber Types	
Fiber support (strain):	SMF 9 / 125 mm ITU-T G.652.D compliant
Fiber attenuation (cabled @ 20 °C):	≤ 1.2 dB @ 1310 nm ≤ 1 dB @ 1550 nm
Number of fibers:	1

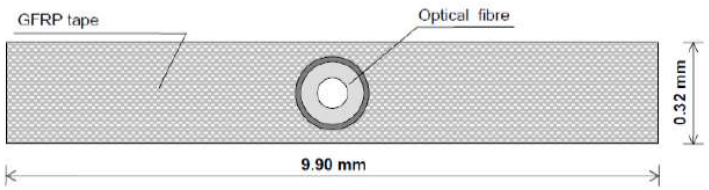

Fig. 18: Technical specifications and transvers section of SMARTape strain sensor by Smartec

Another example, that allows to catch the deformation and the temperature, thanks to the use both Brillouin scattering (BOTDR/BOTDA) and Raman scattering (ROTDR), is the SMARTprofile II. It is built with two bonded and two free single mode optical fibers (BOTDA / BOTDR) and two free multi mode fibers (ROTDR) embedded in a polyethylene thermoplastic profile. “The bonded single mode fibers are used for strain monitoring with BOTDA / BOTDR system, while the free single mode fibers are used to create an optical loop for BOTDA measurement or for temperature measurements with BOTDA / BOTDR system and to compensate temperature effects on the bonded fibers. The two additional multi-mode fibers are insensitive to mechanical strain and used for temperature measurement to compensate temperature effects through Raman system” (Smartec, 2020).

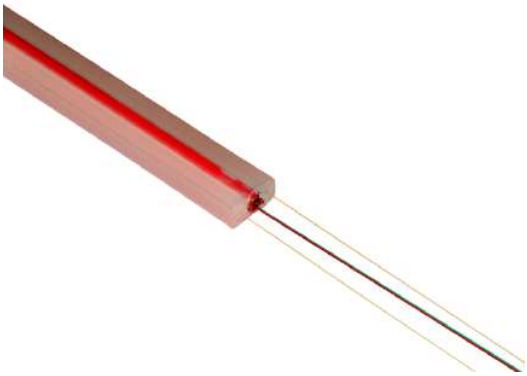

Fig. 19: SMARTprofile II by Smartec

In the following picture is possible to see the main specifications of the SMARTprofile II sensor with his dimension and transversal section.

Temperature compensation:	through single mode temperature fibers with DiTeSt BOTDA / BOTDR, if strain ≤ 0.2 % through multi mode temperature fibers with DiTemp ROTDR, insensitive to mechanical strain
Calibration:	during production
Strain range:	-1.5 % to +1.5 %
Maximal length:	700 m / reel, more upon request
Dimensions (W x H):	8.0 mm x 4.0 mm
Weight:	22 ± 0.5 kg/km
Max tensile strain:	1.5 %
Min bending radius:	400 mm (long term)
Hydrostatic pressure:	300 kPa (bar)
Fiber Types	
Fiber support (strain):	2 SMF 9 / 125 um Polymide coated ITU-T G.652.D compliant
Fiber support (temperature):	2 SMF 9 / 125 um Acrylate coated ITU-T G.652.D compliant 2 MMF 50 / 125 um Acrylate coated ITU-T G.651 compliant
Fiber attenuation (cabled @ 20 °C):	≤ 1.2 dB @ 1310 nm - SMF strain ≤ 1.0 dB @ 1550 nm - SMF strain ≤ 0.4 dB @ 1310 nm - SMF temperature ≤ 0.3 dB @ 1550 nm - SMF temperature ≤ 3.0 dB @ 850 nm - MMF temperature ≤ 1.0 dB @ 1300 nm - MMF temperature
Number of fibers:	2 SMF strain fibers + 2 SMF temperature fibers + 2 MMF temperature fibers

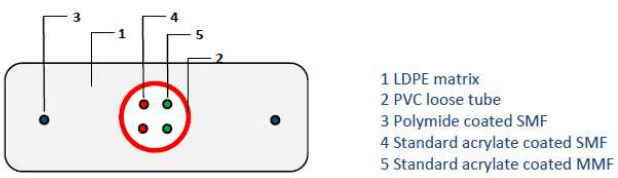

Fig. 20: Technical specifications and transvers section of SMARTprofile II by Smartec

1.2 Innovative smart devices in structural health monitoring

In the previous chapter, we have seen some of the classic measurement systems and some of destructive and non-destructive techniques. However, these techniques do not provide continuous health monitoring data requiring and readily used instruments to measure strain and displacement; they are not suitable to be utilized in a real-life scenario inside the concrete, precisely for this reason the use of innovative smart sensors can help to solve this problem.
A precisely definition of smart technology can be summarized as follows:

"A "smart" technology is one in which "the system systematically reports on the condition of the structure by automatically making engineering-based judgments, records a history of past patterns and intensities, and provides early warning for excessive conditions or for impending failure without requiring human intervention." These features make the system capable of providing and "facilitating self-diagnostic, real-time, continuous sensing, advanced remote sensing, self-organizing, self-identification, or self-adaptation (decision-making and alarm-triggering) functions." Furthermore, the user is not burdened with demanding operational and maintenance tasks" (Ceylan, 2011).

So, to have a smart technology is very important for the future application, but the good monitoring system must have also the following features:

- Low cost unit;
- Easy installation;
- User-friendly way to analyse data;

In the last years, much projects have begun to find new methods to understand the physical characteristic of structure, try following all points above.
In this section we will see some of the new smart devices that are able to use in the assessment of state in concrete structures. Most of these innovative techniques are still under laboratory study, instead other technologies are already development and applied in the full-scale of structure.

1.2.1 Rebar Strainmeters and "Sister Bar"

Rebar Strainmeters and "Sister Bar", are two bars able to measure the strain of the concrete structures. They are designed to be embedded inside the concrete. The main different between Rebar Strainmeters and Sister Bar, is that the first one is used as a bar and become an integral part of the rebar cage, indeed there are some sizes to match the size of the rebar cage; instead the second one is attached to the other bar of rebar cage and it is available in only one size; for this motivation her name is "Sister". The Geokon company have made two different model that are illustrated in the following part.
The firsts models are bars that have a vibration wire strain gauge sensor, that is fixed axially inside a short central length of round steel bar. This central section is de-bondend from the surrounding concrete by means of plastic coating and is extended by welding a length of rebar to each end; is included a thermistor to measure a temperature change. They are fully waterproof and if the cable is adequately protected, they are safe from the concrete placement (Geokon, 2020).

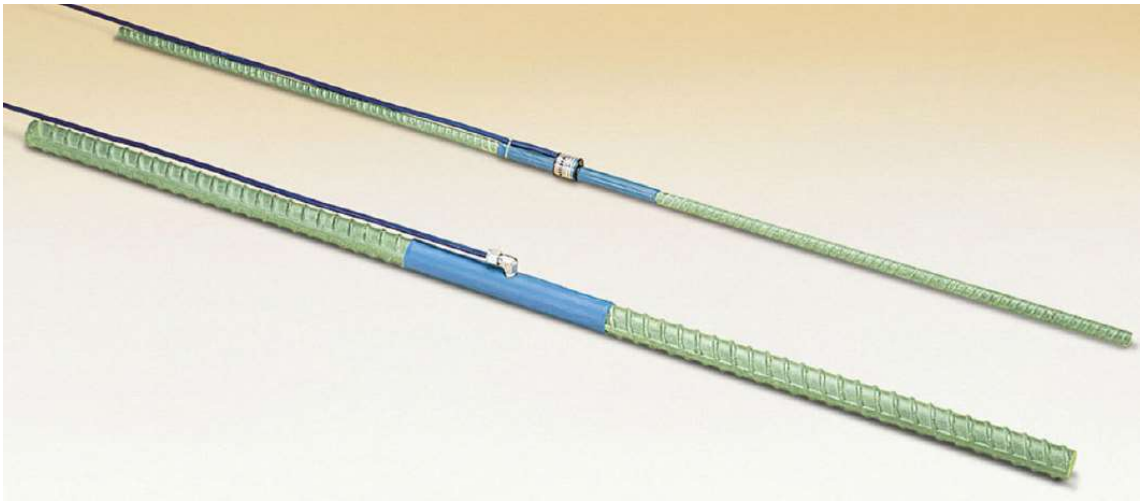

Fig. 21: Model 4911 "Sister Bar" and Model 4911A Rebar Strainmeters by Geokon

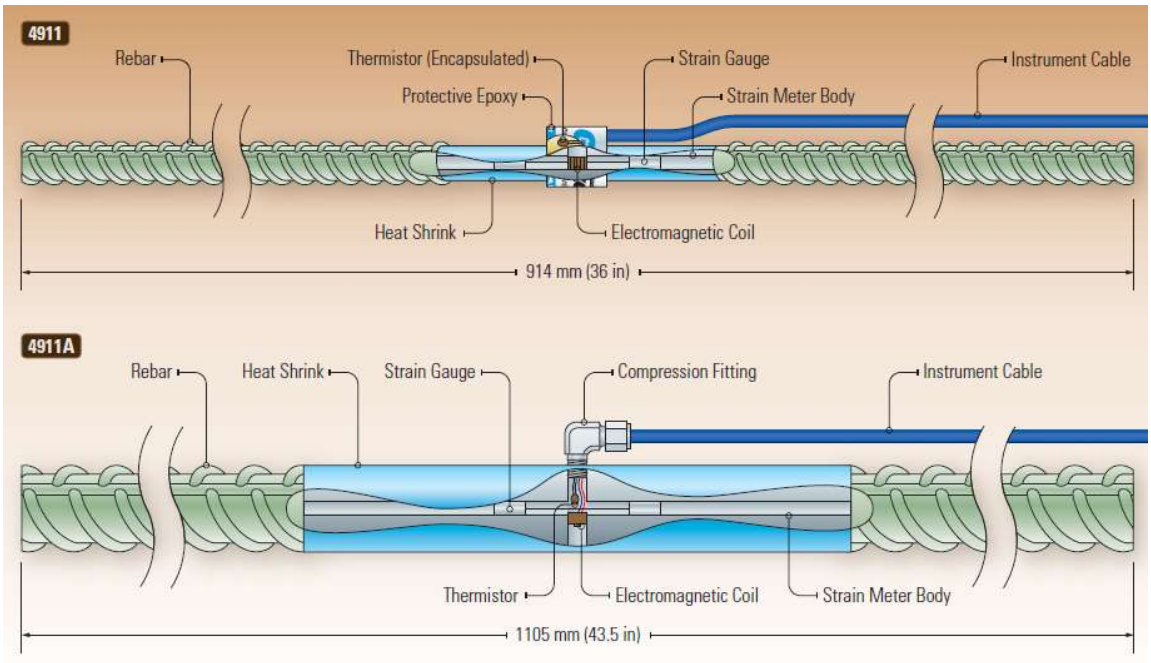

Fig. 22: Components of Model 4911 "Sister Bar" and Model 4911A Rebar Strainmeters by Geokon

The main technical specifications are reported following:

	4911	4911A
Standard Range	3000 με	3000 με
Resolution	0.4 με	0.4 με
Accuracy[1]	±0.25% F.S.	±0.25% F.S.
Nonlinearity	< 0.5% F.S.	< 0.5% F.S.
Temperature Range[2]	–20°C to +80°C	–20°C to +80°C
Rebar Sizes	#4 (Sister Bar)	#6, 7, 8, 9, 10, 11, 14
Length	914 mm	1105 mm

Fig. 23: Technical Specification of Model 4911 "Sister Bar" and Model 4911A Rebar Strainmeters by Geokon

The other similar solution is comprised of two lengths of grade 60 rebar welded to a central section of high-strength steel to which 4 electrical resistance strain gauges are attached in a full Wheatstone bridge circuit. Again, in this case the central section is de-bondend from the surrounding concrete by means of a plastic sleeve (Geokon, 2020).

Fig. 24: Model 3911 "Sister Bar" and Model 3911A rebar Strainmeters by Geokon

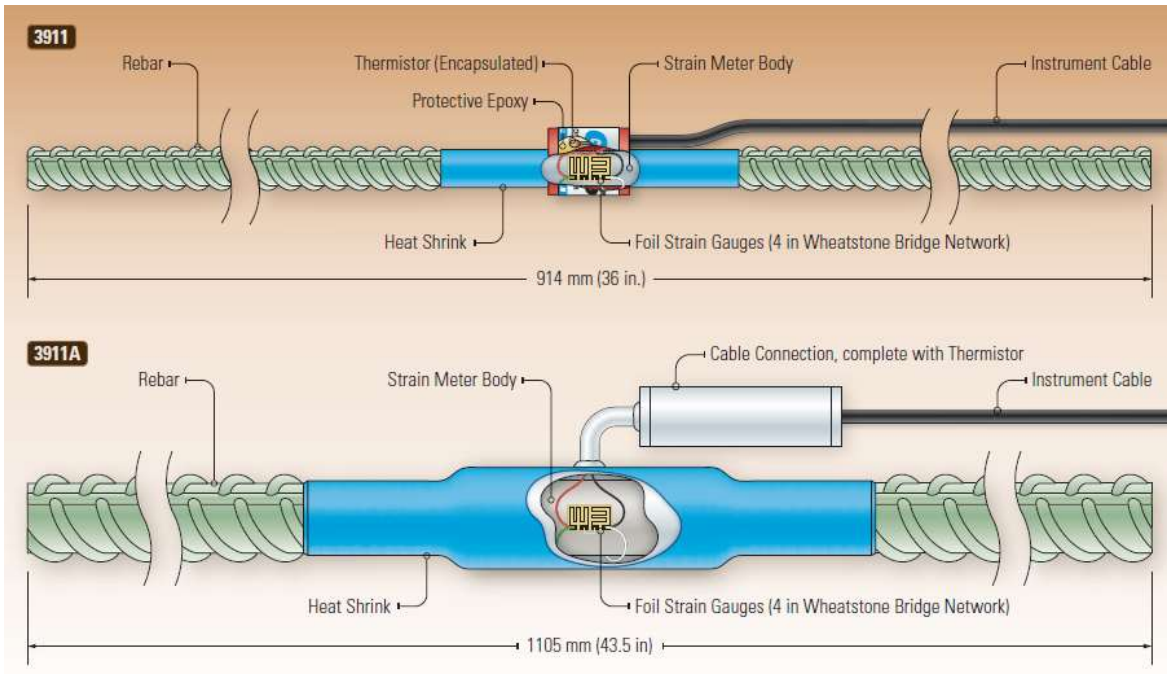

Fig. 25: Components of Model 3911 "Sister Bar" and Model 3911A rebar Strainmeters by Geokon

The main technical specifications about these devices are reported following:

	3911	3911A
Standard Range	3000 με	3000 με
Sensitivity	0.025% F.S.	0.025% F.S.
Accuracy[1]	±0.25% F.S.	±0.25% F.S.
Linearity	0.25% F.S.	0.25% F.S.
Bridge Resistance	350 Ω	350 Ω
Temperature Range[2]	–20 °C to +80 °C	–20 °C to +80 °C
Rebar Sizes	#4 (Sister Bar)	#5, 6, 7, 8, 9, 10, 11, 14
Length	914 mm	1105 mm

Fig. 26: Technical specification of Model 3911 "Sister Bar" and Model 3911A rebar Strainmeters by Geokon

In the following figure is possible to see some examples of installation of the Rebar Strainmeters and the “Sister Bar”.

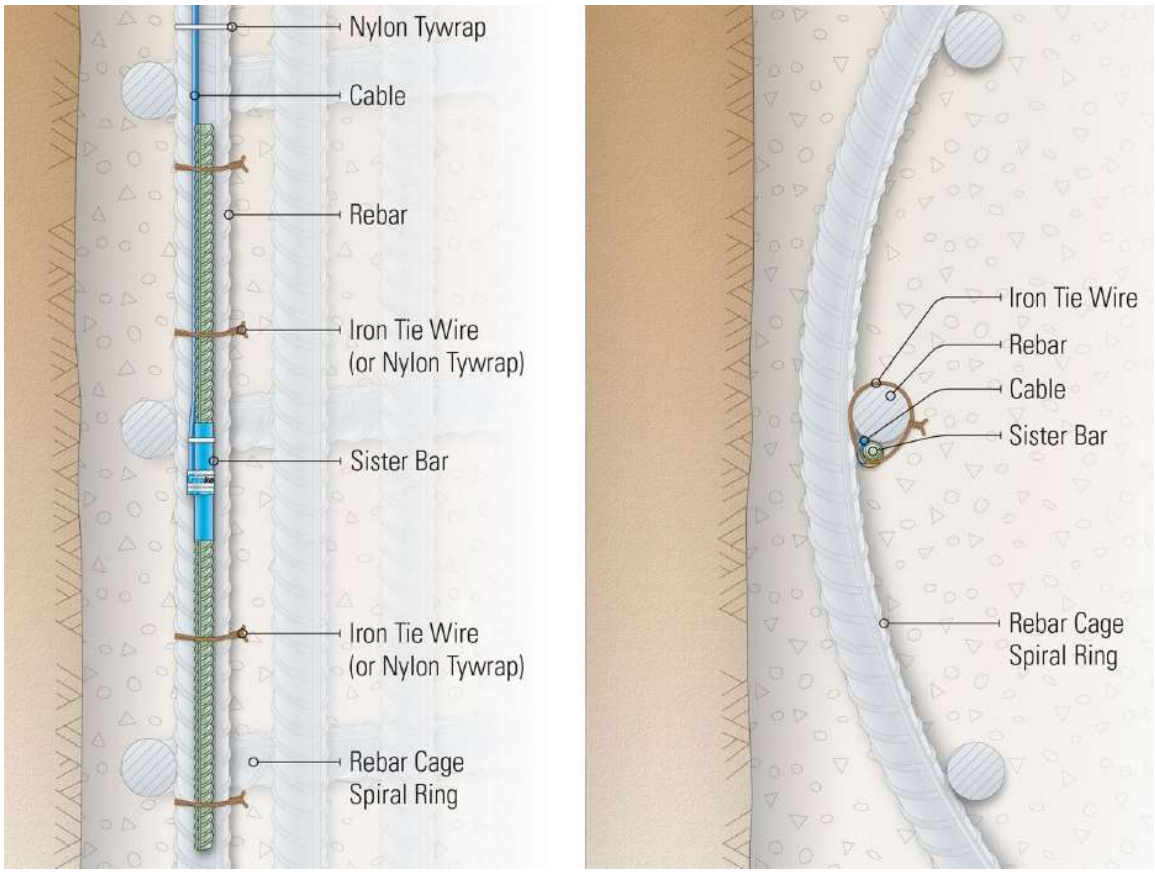

Fig. 27: Sister Bar installation detail by Geokon

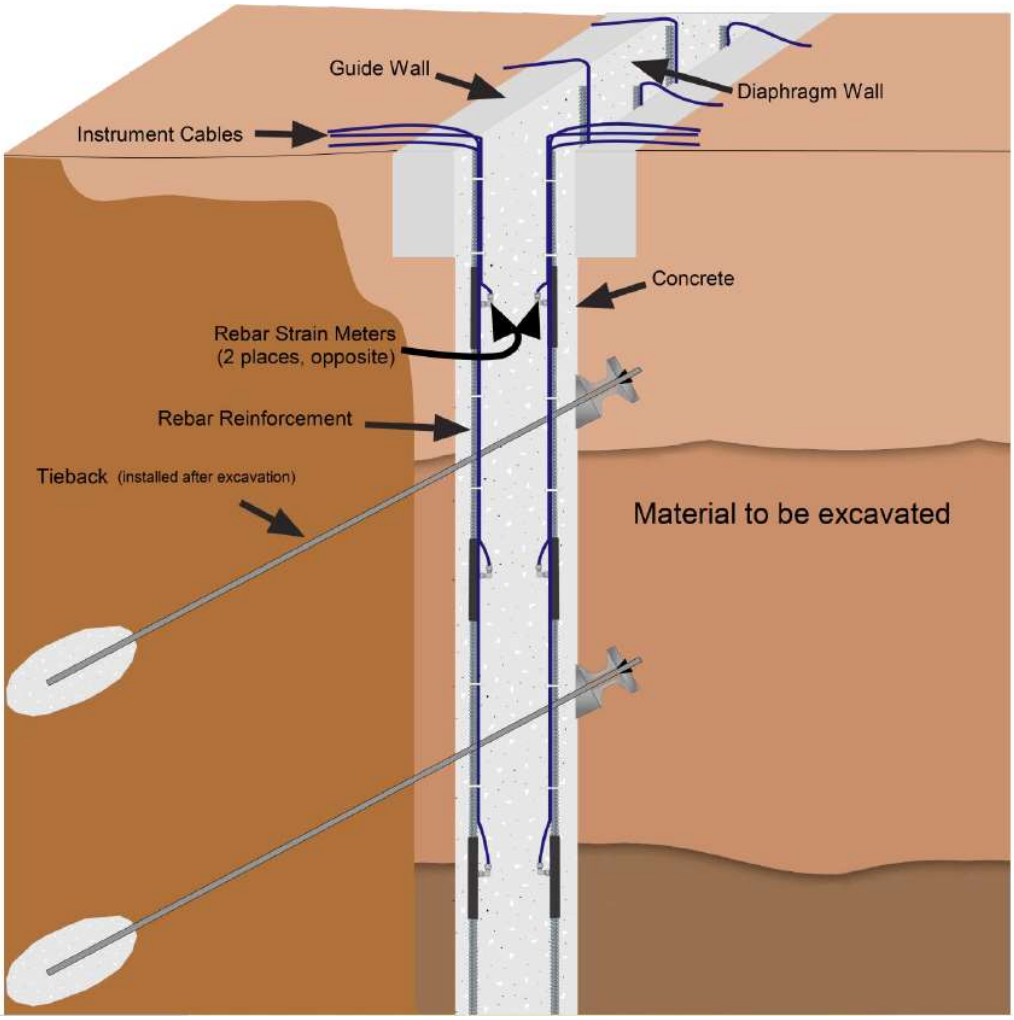

Fig. 28: Rebar Strainmeters installation detail by Geokon

1.2.2 Visible light sensing

Measure bridge displacement, without the need for stationary point is a very important characteristic. There are some different approaches and the most famous are:

- GPS sensor;
- Radar interferometry;
- Laser vibrometers;
- Vision-based displacement system;

But all of these techniques have different problem; the GPS-based method are simple but have a limited accuracy and can be very sensitive to electromagnetic noise, environment interference, and weather conditions; Radar-based system have a good accuracy, but require an expensive equipment and it is subject to radiofrequency interference and noise. Laser vibrometers has a good precision but it could also be dangerous to human health that is present in the structures under inspection in-service data collection. Vision-based techniques, like digital image correlation (DIC) are promising, but the measurement can be significantly impacted by weather conditions and/or vibrations due to passing traffic and humans (Abuella, 2019).

Following this concept, there is another innovative technique called visual light sensing (VLS). It is a new methodology that uses three elements:

- The light emitting diode (LED);
- A photodetector (PD);
- A reflective material and data acquisition unit (DAQ);

All these instruments are necessary to measure the displacement of the structure. The light source is attached to the structure at the point of interest, while the photodetector would capture the changes of light in intensity; this happen when the light source vibrates with the structure. So, the light intensity signal is recorded using the data acquisition module. Practically to calculate the small displacement of the structure, the system uses the change of the power received at the photodetector, thanks the following relation:

$$P_r = KD^{-\gamma}$$

- P_r is the signal power at PD;
- K is a constant that depends on the PD settings;
- D is the distance between the transmitter (LED light source) and receiver (PD);
- γ is the path-loss exponent which depends on the environmental conditions;

With the calibration process, is possible finding the value of K and γ; to estimate the variation of distance, a least square (LS) algorithm is used to fit the P_r samples collected over a time step duration (Δt) to a straight line whose slope is considered to be equivalent to the change in distance ($\delta d \delta t$) (i.e., displacement rate). To calculate the displacement have been used two estimation method: single time-window and multiply time-window. The displacement is calculated also with an LVTD and the results are compared with the VLS. According with the laboratory tests the biggest different between the results obtained with LVDT and VLS is about 7%. Further, the total system's cost is more or less 500 $ (Abuella, 2019). However, this type of device are under studying and more testing and analysis are still required to validate the feasibility of the system for use in outdoor environments (Abuella, 2019).

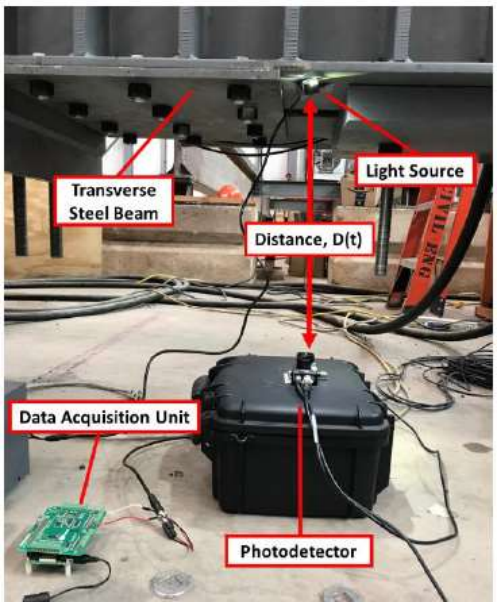

Fig. 29: Setup used to collect the data during the laboratory test

1.2.3 Skin-like smart sensor: Soft elastomeric capacitive sensor

"The soft elastomeric capacitive (SEC) sensor is a flexible flat parallel plate capacitor which consists of a high dielectric polystyrene-co-ethylene-co-butylene-co-styrene (SEBS), mixed with TiO_2 composite, enclosed between 64x64 mm^2 conductive electrodes composed of a mixture of SEBS and carbon black" (Rácz, 2016).

The sensor is attached against the monitored mechanical structure and when some mechanical deformation appear on the structure, the capacitor stretch making the changes in electrode area and dielectric thickness cause a capacitance change as given by the following equation: $C = C_0(1 + \varepsilon_T)$.

Therefore, the capacity change is calculated as follow:

$$\Delta C = C - C_0 = \varepsilon_T C_0$$

- C is the stretch capacity;
- ε_T is the transverse strain;

The capacitance change is measured as a change in the resonant frequency of a relaxation oscillator circuit that is connected to an Arduino Mega 2560 microcontroller board for data recording and processing. The capacitive sensor is mounted on two acrylic plates that are separated manually to stretch the sensor. According with the laboratory study, is possible to see the existence of a linear relationship between the stretch length and the frequency change. In fact, when the sensor stretch in one direction, the average frequency shifts caused by each millimeter stretch. This sensor has the potential to detect sub-100 micron cracks. (Rácz, 2016)

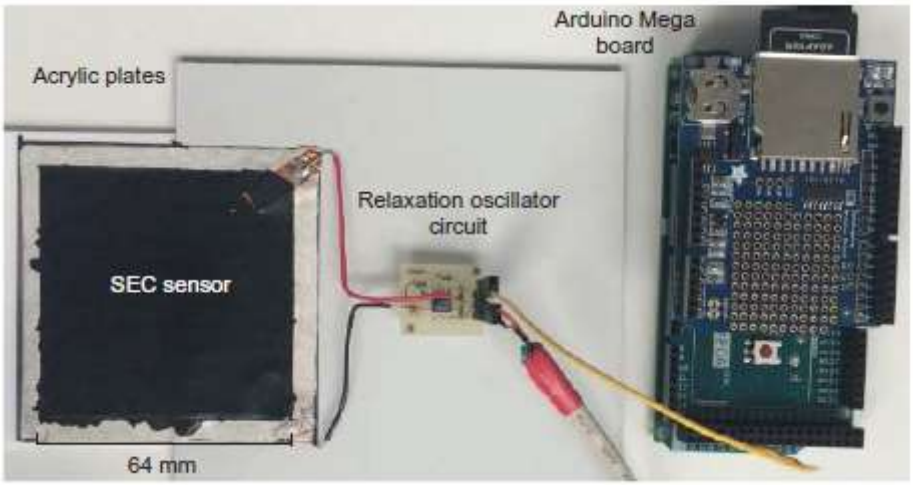

Fig. 30: The soft elastomeric capacitor based sensor system showing the sensor, the relaxation oscillator circuit and the Arduino microcontroller board

1.2.4 The Piezo-Floating Gate (PFG) sensing platform

The PFG Sensing Platform consists of two major components:

- Piezoelectric disc: is a transducer that generated voltage when deformed, so it allows for the conversion of kinetic to electrical energy. This transfer of energy doesn't require any external power source to be applied and could be good to make a self-powered sensing system. The choice of the dimension and the type of transducer are important to ensure the functionality of the sensor and also the harvested voltage can be adjusted to a specific strain level (Pochettino, 2019).
- Piezo Floating-Gate Sensor core: "The PFG sensor, cumulatively records the strains and accelerations affecting a structure through the principle of Hot Impact Ionized Electron Injection, which is the ability of electrons that flow through the channel of a Metal Oxide Semiconductor Field Effect Transistor (MOSFET) to break through the silicon-silicon dioxide barrier when a sufficient electric potential is applied across the terminals of the device". The operational energy for the PFG sensor is asynchronously harvested from the sensing signal itself, as a result the sensor can continuously operate and record events without the need for extrinsic powering (Pochettino, 2019).

These components are used in conjunction to create a self-powered data logger for sensing and recording the strains or acceleration applied to infrastructure.
So, in order to allow for the sensors to be read from while the structure is still in operation, a wireless interface has been integrated with the PFG sensor core and piezoelectric disks to make a quasi-self-powered wireless sensing system that can achieve a life about 20 years. (Pochettino, 2019).

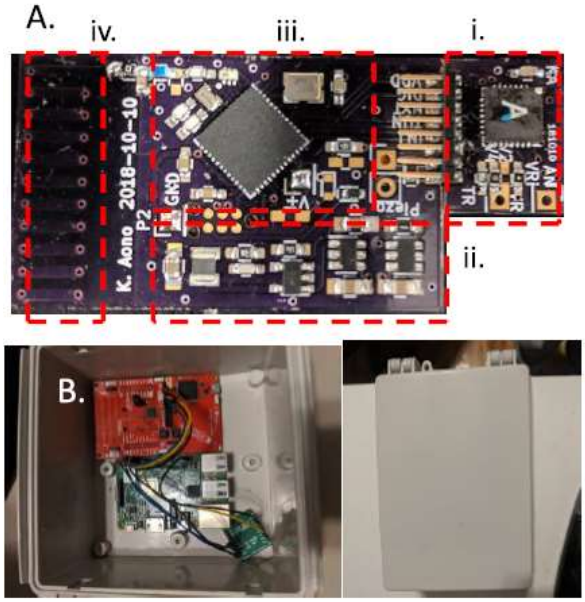

Fig. 31: A shows a prototype for the i-IoT sensor node highlighting the i) PFG sensor core, ii) timer and regulation circuitry, iii) RF MCU, and iv) antenna. B contains an image of the reader system

1.2.5 Liquid Level Sensing System (LLSS)

This technique is usually used to understand the bridge displacement, for both short-term and long-term monitoring.

To measure the deflection, the pipeline is mounted on main girder of the bridge and filled with a liquid like water. The pressure transmitter, that are connected with the pipeline, are placed at the point of interest P_i, where the first point is set on the pier. When the deflection appears, due to the loading on the structure, the pressure in the pipeline changes, cause by the changes in liquid level. So, this change of pressure is collected and transformed in deflection with algorithms (Ye, 2019).
In the following pictures we can see the example of the complete system.

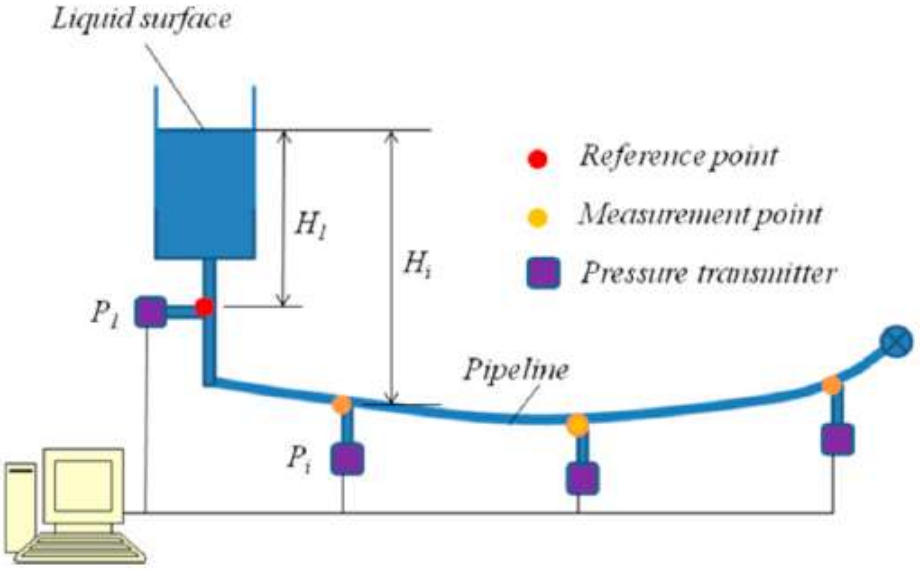

Fig. 32: Layout of a typical liquid level sensing system

The static deflection is obtained from the following equation:

$$u_{i,t} = \frac{\Delta P_{i,t}}{\rho g} = \frac{P_{i,t} - P_{i,1}}{\rho g}$$

This method has been used for more than 40 years, and the applications of static deflection measurement for large-scale bridges have proved its validity. In the recent years, few studies on dynamic deflection measurement has been made with LLSS (Ye, 2019).
But with the dynamic, the structural vibration gives a contribution it the pressure change, so is needed to add a correction term to the previous formulation. The total pressure change is resume with the final formulation as follow:

$$u = u_{i,t} + \Delta u_{i,i}$$

The main problem with this technique is about the installation of the system, where is possible to do some mistakes in construction process.

1.2.6 Stress sensor for concrete: self-sensing concrete

The classic method for measuring the working stress of concrete is the stress release method. The basic principle is to drill or cut in the concrete stress measurement area, so that the stress is released, the strain before and after the stress release is measured, and the stress of the concrete is obtained after calculation. The main problem with this technique, is about the influence of external vibration and can obtain inaccurate measured. (Liu, 2019)

So, to understand the value of the stress inside the concrete structure, one technique that is developing in these last years is the self-sensing concrete.
It means the materials with intrinsic sensing properties, such as carbon nanofibers (CNF), carbon nanotube (CNT), semi-conductive or conductive nanoparticles that are mixed into concrete (Taheri, 2019).
More of these new sensor uses the piezoelectric material. It will generate electric charge when it is subjected to a stress or strain (the direct piezoelectric effect); the piezoelectric material will also produce a stress or strain when an electric field is applied to a piezoelectric material in its poled direction (the converse piezoelectric effect). Due to this special piezoelectric property, piezoelectric material can be utilized as both an actuator and a sensor; this property enables the multi-functionality of the smart aggregates.

In the following part, we will see some innovative technique about self-sensing concrete, that are under study from the researcher.

1.2.6.1 The MMCC (magnetic microwire in cement-based composite) sensor

The MMCC sensor, is a non-destructive testing method to understand the mechanical characteristic of the concrete. It was created to study the possibility of contact-less measurement of compressive stress in a cement-based composite by using an embedded amorphous magnetic microwire embedded as simple aggregates inside the concrete structure (Olivera, 2014).

The amorphous magnetic has really tiny dimensions (around 1–100 μm in diameter) and these microwires consist of a metallic nucleus (10–80 μm in diameter) covered by a glass coating (2–20 μm thickness). They are produced by simultaneously melting the metallic nucleus with the insulating coating and then rapidly cooling it in water to achieve an amorphous structure with a unique distribution of strong internal mechanical stresses. The mechanical stresses created during this process fabrication, together with magnetostriction, determine the strength of magnetoelastic anisotropy. Indeed, the domain structure of amorphous microwires with positive magnetostriction consists of one single axial domain in the inner part of the microwire, which is surrounded by a radial domain structure just below the surface. Additionally, small closure domains appear at the ends of the microwire to decrease the stray fields (Olivera, 2014).

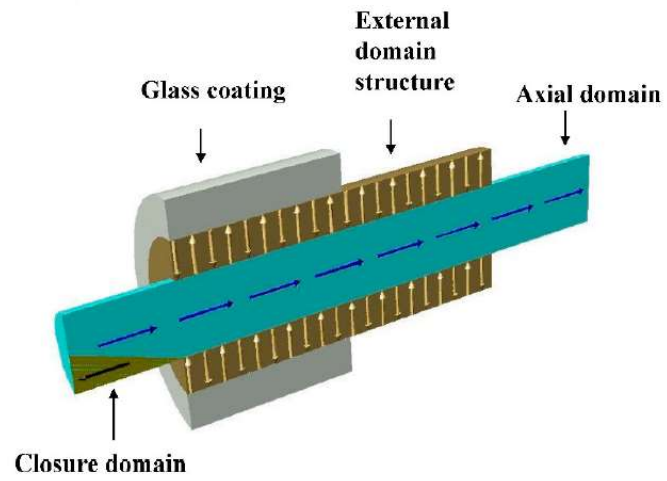

Fig. 33: Schematic domain structure of positive magnetostriction microwire

The microwire has a length of 60 mm and it is inserted into the axis of a mortar cylinder. After this the mortar cylinder is insert in the cement. In the following pictures is possible to see the making process of the sensor.

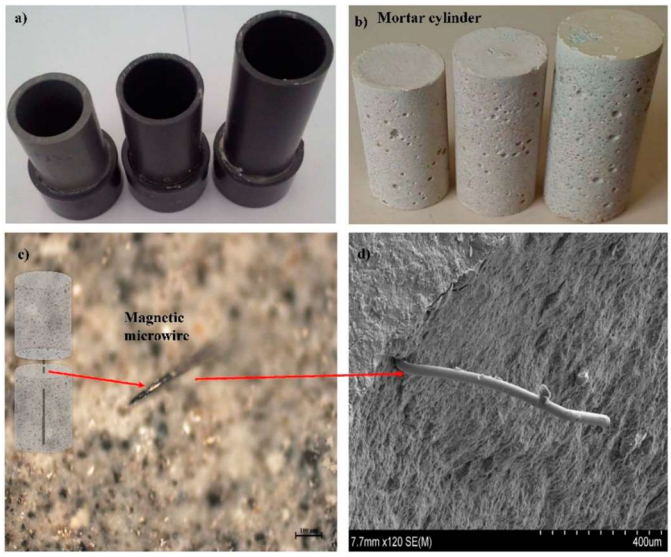

Fig. 34: (a)Molds for MMCC sensors; (b) mortar cylinder with an embedded microwire; and (c) and (d) optical and electronic micrograph, respectively, of the embedded microwire

The work principle of this sensor consists of a stress sensitivity of the magnetization reversal of a ferromagnetic microwire, that measures variations of magnetic properties resulting from stress variations. The use of magnetic microwires allows creating a built-in stress/strain sensor inside the material without affecting its mechanical behaviour. Thanks to the performance of the MMCC sensor, two stress sensing properties of the switching field value of the embedded sensor under uniaxial compression were selected: peak amplitude and peak position (Olivera, 2014).

According with the laboratory test, is possible to see the change of peak amplitude and peak position under compressive load. Therefore, the sensitivity values amplitude and position within the application range were 5 mV/MPa and 2.5 μs/MPa, respectively.

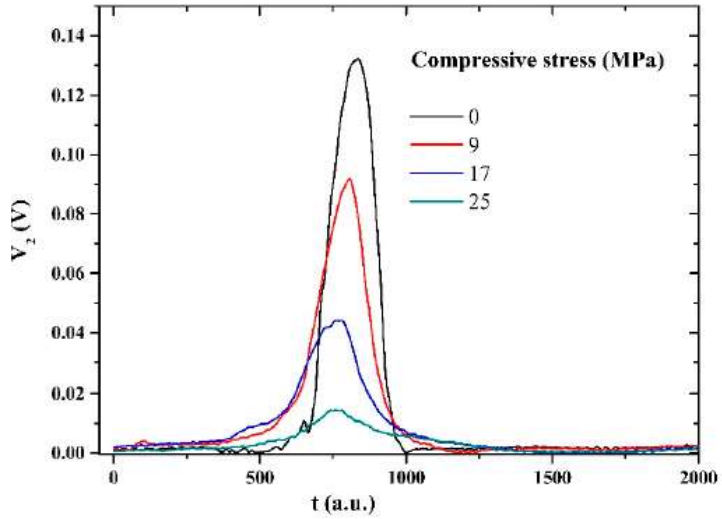

Fig. 35: Change of shape (peak amplitude and peak position) of the voltage from the pick-up coil (V2) under applied compressive stress.

1.2.6.2 Cement paste stress sensor

The cement paste stress sensor is formed with the PZT patch that is capsulated to make it waterproof and barrier the irrelevant electromagnetic interference. In one cement paste sensor there are two PZT sheet; because they can be influenced of the boundary echo on the signal, their position must be as far as possible from the edge. As is illustrated in the following figure, between position the two piezoelectric sheet is selected to be 60 mm (Liu, 2019).

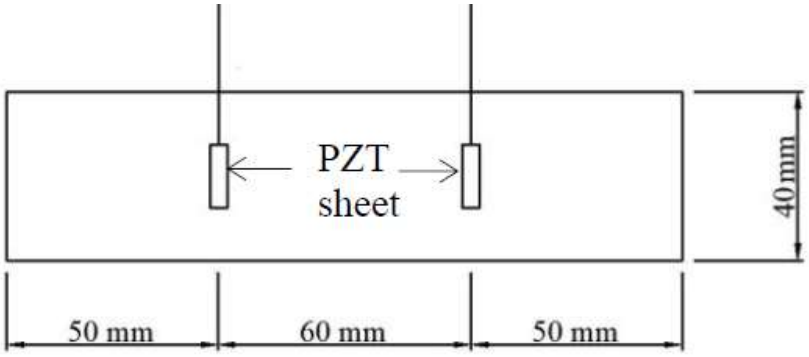

Fig. 36: Scheme of cement paste stress sensor

The cement past sensor is embedded inside the concrete element to understand the level of stress inside, under loading.

The important element is the peak area A, that is defined as the absolute integral of the amplitude of the received signal from 0 to 0.065 milliseconds. Indeed, to get the stress inside the concrete, is necessary to understand the change of the peak area of the sensor under different loads; from the laboratory result have been provided that the relative peak area has a significant correlation with the stress. As the stress increases, the relative peak area decreases continuously. In summary, the relative peak area can be used as a parameter to monitor the working stress of concrete (Liu, 2019).

According with the result of the laboratory tests, is possible to see that the average error of the predicted stress using the relative peak area under low stress is higher than that under high stress. Further, when the average stress of the section is larger than 15 MPa, the average error of the predicted stress is around 10% by using the relative peak area. In conclusion the monitoring the stress inside the concrete has a higher accuracy when the level of the stress is larger than 15 MPa (Liu, 2019).

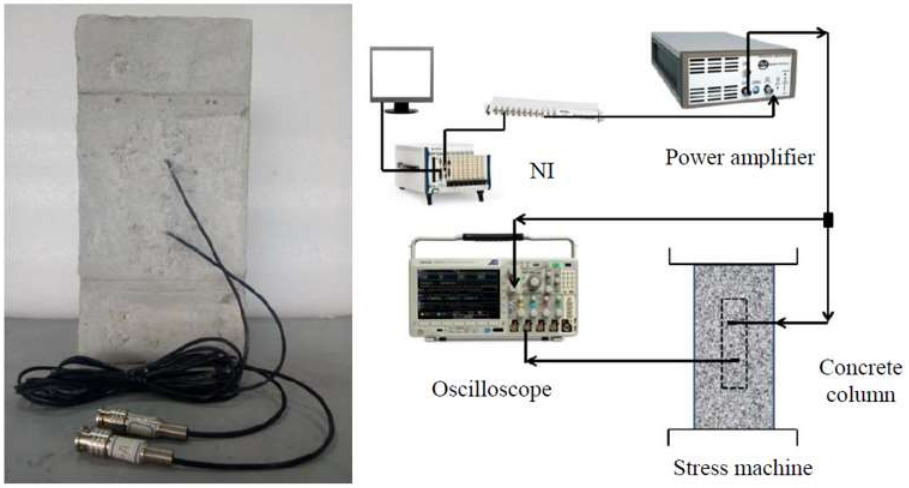

Fig. 37: Concrete column with stress sensor imbedded and relative monitoring system

1.2.6.3 Fiber-cement piezoelectric composite sensor

This sensor is composed from a cube with a size of 5cm*5cm*5cm, where inside there are eight circular piezoelectric lead zirconate titanate (PZT) ceramic sheets that are located at the center of a cube. The diameter of the used circular piezoelectric sheet is 25mm and his thickness is 0.5 mm, respectively. The sheets are connected together in series and the gap between the piezoelectric plates is 2 mm (Lezgy-Nazargah, 2019).

The employed matrix material is a new composite material consisting of five components of Portland cement, resin, water, fine silica, and polymeric fibers. This new employed matrix has high compressive strength which is essential for the proper performance of the sensor at high level of stresses. Thanks to the presence of polymeric fibers in the mix design of the composite matrix, the fabricated sensor has not brittle behaviour. The presence of resin in the matrix has been increased the waterproof characteristic of the fabricated sensor and prevents the penetration of moisture into sensitive piezoelectric sheets. The strength of matrix material is about 14 MPa. In the fabrication process of the sensor, the piezoelectric circular plates were first fixed at the center of the mold and then the cement-resin-fiber composite matrix was poured into the mold (Lezgy-Nazargah, 2019).

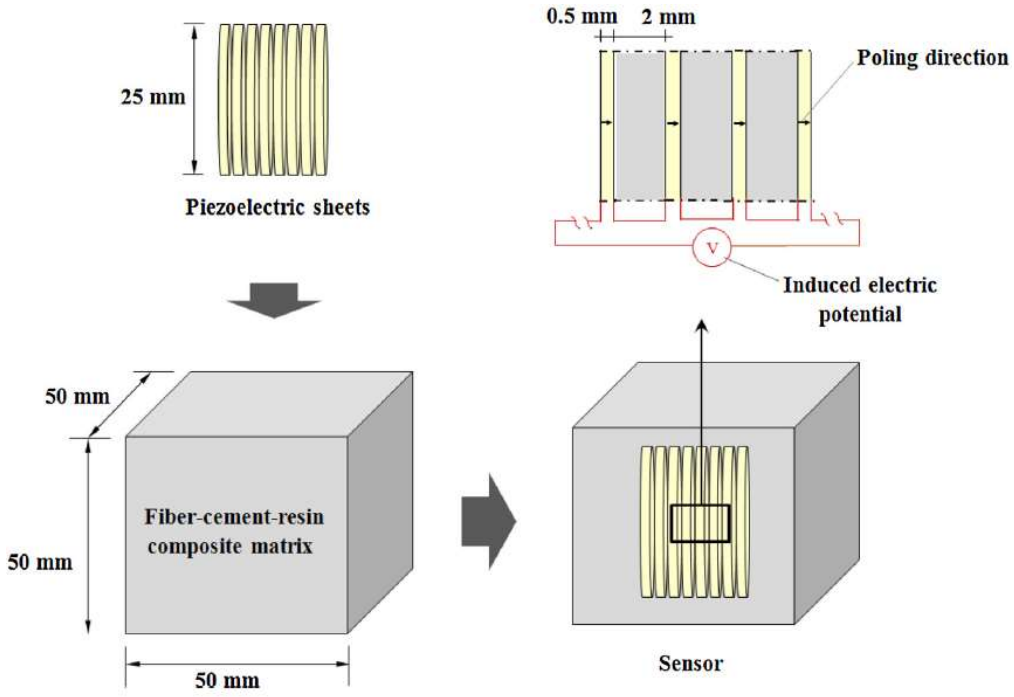

Fig. 38: Schematic details and steps for the fabrication of the proposed sensor

Under the dynamic compression loadings, the sensor charge outputs are transferred to voltage using an amplifier. The amplified voltages are acquired and recorded by a dynamic data logger system. The experimental results show that the fabricated sensor has high measurement accuracy over a wide range of frequencies. It shows a linear relationship between the output voltage and applied load in the range of the vibrating frequency of the common concrete structures (0.5–50 Hz) (Lezgy-Nazargah, 2019).

1.2.6.4 A PZT-based smart aggregate for compressive seismic stress monitoring

The proposed smart aggregate (SA) consists of a piece of PZT patch connected with a piece of two-wire cable and a pair of marble cubes. The size of the PZT patch is 15 mm x 15 mm, and the thickness is 0.3 mm. The PZT patch was connected to the two-wire cable on its two sides at the position close to one of its edges through soldering. The marble was cut into a pair of size 25x25x12 mm^3. Then the PZT patch is insert between the marble cube pair though epoxy. After the epoxy was cured, the thickness of the epoxy layer is measured to be about 0.45 mm. Piezoceramic transducers are very fragile and can be easily damaged by the vibrator during the casting of concrete structures, so the PZT patch is embedded in order to protect it (Hou, 2012).

The compressive strength of commonly used concrete is generally not higher than 60 MPa. At this stress level, the PZT material is in the elastic stage.

The choice to have a marble-based SA is it more stable in mechanical behaviour in comparison with the cement-based SA. Moreover, the PZT patch in the marble-based SA can be easily fixed during its fabrication. These features, give a higher accuracy for stress measurement than the cement-base SA (Hou, 2012)

According with the laboratory result, the proposed smart aggregate is able to monitor the seismic stresses of low and middle rise building subject to a moderate earthquake. This is due to some limitation about the coupling the SA and a commercially available charge amplifier, because the sensing system for dynamic compressive stress has lower limit of frequency response of 0.5 Hz and upper limit of stress amplitude of 6.3 MPa. To amplify the application of this monitoring system to a lower frequency response and the higher dynamic stresses more studies should be development in the future (Hou, 2012).

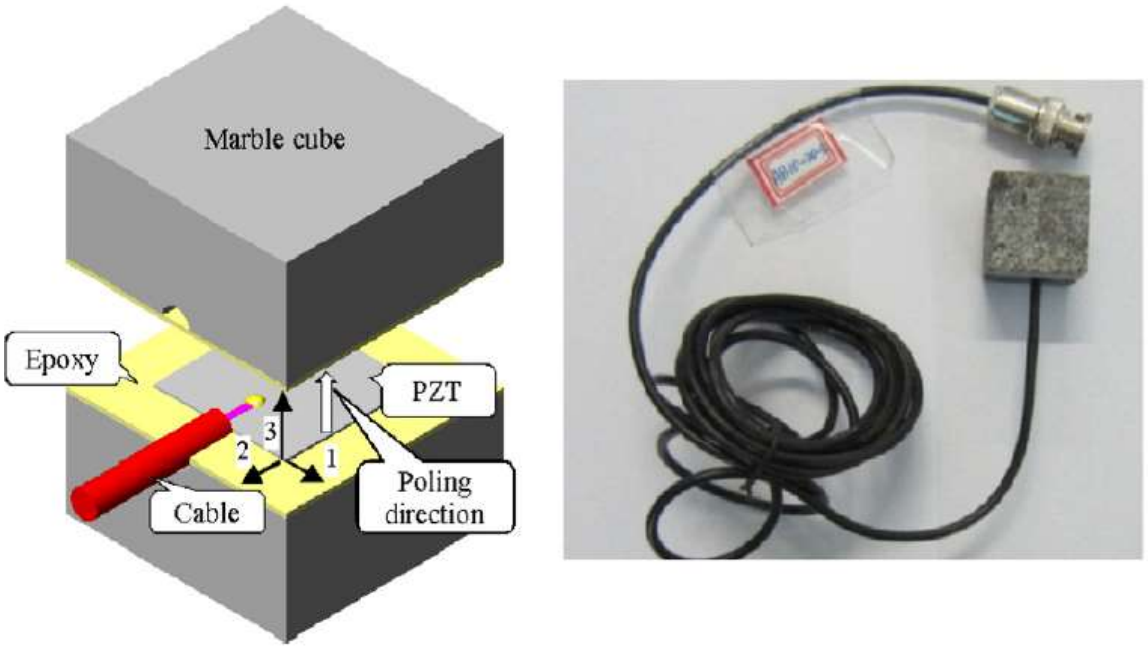

Fig. 39: Schematic and photo of smart aggregate

1.3 A new era with MEMS in SHM

MEMS (Micro Electro-Mechanical Systems) have been developed in many areas including the medical and automotive industries.
Although MEMS are new to civil engineering world and could have a good future in the field of structural health monitoring, because there are a lot of number of research project that are exploring how apply MEMS technology to enhance the monitoring system. So, the idea to incorporating MEMS sensor technology into SHM of structure and infrastructure, could bring a lot of potential benefits.

We can classify the MEMS sensor in three broad categories:

- Sensor: they are transducers that convert mechanical, thermal, or other forms of energy into electrical energy;
- Actuators: this device is the opposite of the sensor and they convert the electrical energy in mechanical, thermal, or other forms of energy;
- Passive structures: the devices in which no transducing occurs;

In function of a type of sensor above, we can have the passive system that requires the use of a reader or interrogator to transmit an electromagnetic field to activate the sensor to begin transmitting data, or active system that are equipped with an internal battery that transmits information to the reader at a specified time interval.
Furthermore, MEMS sensor have the capabilities to measure a variety of different properties such as pH, corrosion, strain, accelerometers, pressure sensors, temperature sensor and flow and if are incorporated into a wireless sensor network beside help inspection by providing data from within the structure, would potentially allow inspector to retrieve real-time structures data (Ceylan, 2011).
One of the big advantages to employ MEMS, is because they have a really small size, inexpensive cost (when mass produced), and low power consumption (Nagayama, 2007)

Chapter 2
2. Significance of the work

In the previous chapter, we have seen some new smart technology for structural health monitoring. One of this new technology is “S3 System”, actually under study and topic of this master thesis. The “S3 System” is an embedded system and it is based on a Patent (Tondolo, 2016); it consists in a classic steel bar for reinforced concrete, with a circular cavity obtained as a transversal drilled hole, filled with a fluid and hosting an ordinary low-cost embedded Micro Electro-Mechanical Systems (MEMS) sensor. The sensor LPS25H (STMicroelectronics®) is very small (about 2.5x2.5x1 mm3) and it is mounted on an hard PCB contained inside the cavity, which is closed by an electrical feed-through element, designed to let a soft PCB pass through it in order to allow signals transmission and power supply. The cavity is hermetically sealed, and the sensor is connected by the soft PCB to a converter board linked to an acquisition system. The system works thanks to the MEMS sensor that is able to measure the variation of temperature and pressure inside the cavity, and with measures, using the perfect gas law, is possible to evaluate the cavity volume variations that it is correlated with the bar axial deformation.

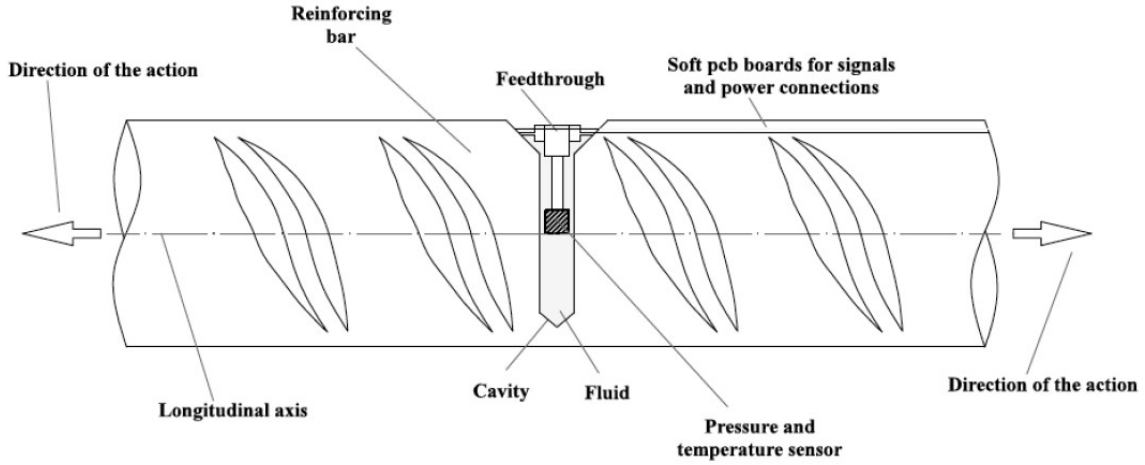

Fig. 40: Longitudinal view of the “smart” steel bar

The presence of the cavity is a reduction of the section of reinforcing steel bar; it represents a critical point for stress increase and concentration that could be a reduction of resistance and/or ductility of bar itself. So, one of the most important parameters is the stress intensity factor (Kt), that must be studied. In the chapter 3 we have been analysing this aspect; at the beginning to verify the validation of the theoretical formulation, we have made a numerical model of a simple rectangular plate with a hole in tension. The problem was focused of the dimension and the form of the hole to look for the best solution namely to reduce the stress near the hole. Having had a good response with theoretical and numerical formulation, we have done the same work, but on the numerical model that want to simulate the real form of the “smart” bar. In the chapter 4 the focus of the work has been how to improve the sensibility of the instrument; currently the devices have a sensibility about 1 με; so, is necessary at least to reach this sensibility.

From the moment that minimum value of pressure that the MEMS sensor used in the “S3 System” is able to catch is 1 Pa, is needed that for each με on the bar, the variation of pressure inside the cavity has to be at least 1 Pa. After we have done a numerical model with only air inside the cavity; we have seen that in this situation is very difficult to have the request sensibility when the bar is subjected to a mechanical action. A possible solution could to fill partially the cavity with an incompressible fluid like oil, to bring the pressure to have a higher value in presence of mechanical action. So, we have analysed how much was the percentage of the oil inside the cavity to reach the wanted sensibility and we have built a corresponding numerical model to verify the theoretical assumption with the numerical result. This study has been in elastic field of the “smart” bar and we have seen what happens to the pressure inside the cavity when the reinforcing bar starts to evidence plasticity. Until this point, we have analysed the only mechanical action on the “smart” bar but is a very important to understand the effect of temperature on the entirely system. It is very important because the common structures are subjected to daily variation of temperature that could bring some deformation in the structure. In our case, a variation of temperature brings a variation of volume of the cavity and consequentially a variation of pressure inside the fluid it is. Is needed to understand how much the variation of pressure is, due to temperature effect to separate the latter from the effect of mechanical action, that is to be measured. So, we have done before a numerical analysis to understand how much the pressure change is, due to an only temperature effect comparing the result with the theoretical assumption and after we have done a combined analysis with both mechanical and temperature action. Both studies with only temperature effect and both temperature and mechanical action, was done with the cavity empty (only air inside) and with the cavity filled with a percentage of oil. From the results we have seen the benefit of the presence of incompressible fluid inside the cavity. In the last chapter the results are reported from the experimental campaign carried out on the 50 cm “smart” steel bar length, equipped with three sensors of the “S3 system” subject only to ambient temperature variation in a non-controlled environment. We perform a long-term monitoring, able to collect the variation of pressure and temperature inside the fluid cavity, to compare the experimental result with the numerical result.

Chapter 3
3. Numerical study: Stress intensity factor

When in a structure is present a discontinuity, the stress around this could increase, causing a previous damage of the structure in this point. The increase of the stress depends of the form of the imperfection and how the structure is loaded. The most important parameter is characterized from the stress intensity factor (K_t). A precisely definition of this is:

$$K_t = \frac{\text{Highest value of stress at a discontinuity}}{\text{Nominal stress at minimum cross} - \text{section}}$$

Kirsh (1898) was the first that found the solution of this problem. He studied the effect of circular hole inside of an infinity plate in tension. From the results, he found that the stress near the hole, in the direction of the load was three time higher than the stress in other point of the plate.

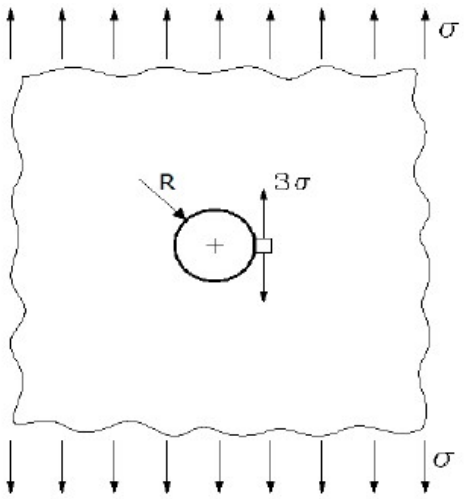

Fig. 41: Plate with circular hole

The K_t is influenced from the dimension of the plate, both thick and width. How we have seen before, If we have an infinity plate, the theoretical value of stress intensity factor is 3, but in the reality, minor is a cross section of the plate where there is the hole, biggest is the value of the stress intensity factor; the K_t could became bigger than 3.

In the following pictures we can see that the σ_{max} occurs at A and B points and the value K_t change with w (width of the plate) and h (thick of the plate).

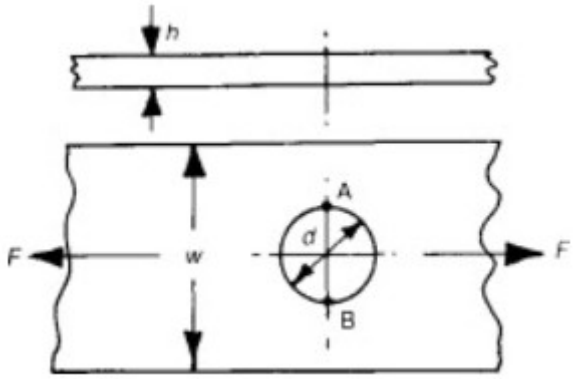

d/w	0.00	0.10	0.20	0.30	0.40	0.50	0.55
K	3.00	3.03	3.14	3.36	3.74	4.32	4.70

Fig. 42: Kt value of the plate in function of the width and the thick

After Kirsh (1898), there was Inglis (1913) that extended investigations on stress concentration to more general case like an elliptical hole. Analysing the interesting case, so when the hole is in direction of the load, having:

- $\beta = 0$;
- a = major axis;
- b = minor axis;

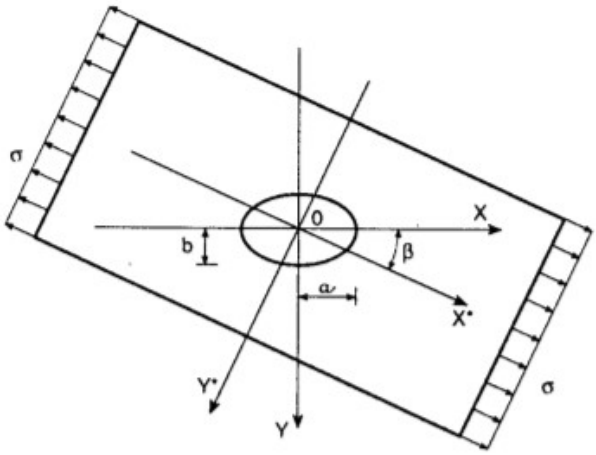

Fig. 43: Plate with elliptical hole

In this case, when the load is perpendicular to minor axis, we have this relation.

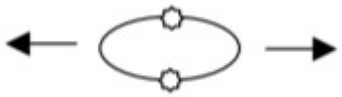

$$\sigma_{max} = \sigma\left(1 + 2\frac{b}{a}\right)$$

We can see that the value of stress intensity factor reduces a little and depend of the ratio from the two axes of the elliptical hole.

How we can see from the result obtained from Kirsh and Inglis, a little hole is a discontinuity that can increase the tension around itself. In our study, we have a simple reinforced bar with a little hole, where inside is hosting a MEMS device, how we have explained in the previous chapter. The cavity is a discontinuity; so, the stress near increase and could make a plasticization before the other points of the steel bar. The steel bar wouldn't work properly because it could damage before.

Is very important to understand how much higher the stress near the hole is, and is needed to find a way to reduce the K_t.

From the theory point one of the solutions to reduce the stress is to change the form of the hole, from circular to elliptical hole. If we are in the classic situation, where the steel bar is subjected to the stress along his axis, namely the stress is perpendicular to the minor axis of the elliptical hole (b), we can see that it's possible to reduce the stress intensity factor working with the ratio of two axis of the ellipse. In the following table is reported how the stress intensity factor can change, working on the axis of the ellipse, from the theoretical point.

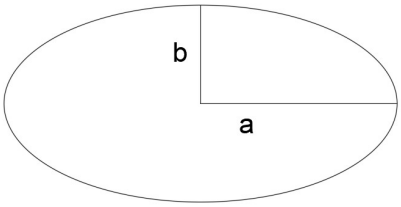

Fig. 44: Axes of elliptical hole

Axis	$K_{t\_theoretical}$
a = b	3.0
a = 2b	2.0
a = 3b	1.67
a = 4b	1.50
a = 10b	1.20
a = 20b	1.10

Stretching the major axes (a), we can see that a reduce of the stress intensity factor.

To understand if changing the form of the hole, the Kt value follows the theory considerations, we have created a plate FEM model with 2D elements, to control better the problem. After this analysis is extended also to the "smart" steel bar under study, built with 3D elements.

3.1 Plate with the hole in tension

To understand the stress behaviour near the hole and try to optimize his form, we have created different plate model with different form of the hole, and we have compared the results with the theory model (infinity plate).

We have made a rectangular shell plate with the dimension in Y direction like the steel bar under study. So, this plate is 20 mm large and as long as possible as to have a dissipation of the stress far of the hole. Doing different attempts, the length of 50 mm is a good solution. The measure of the plate is the following:

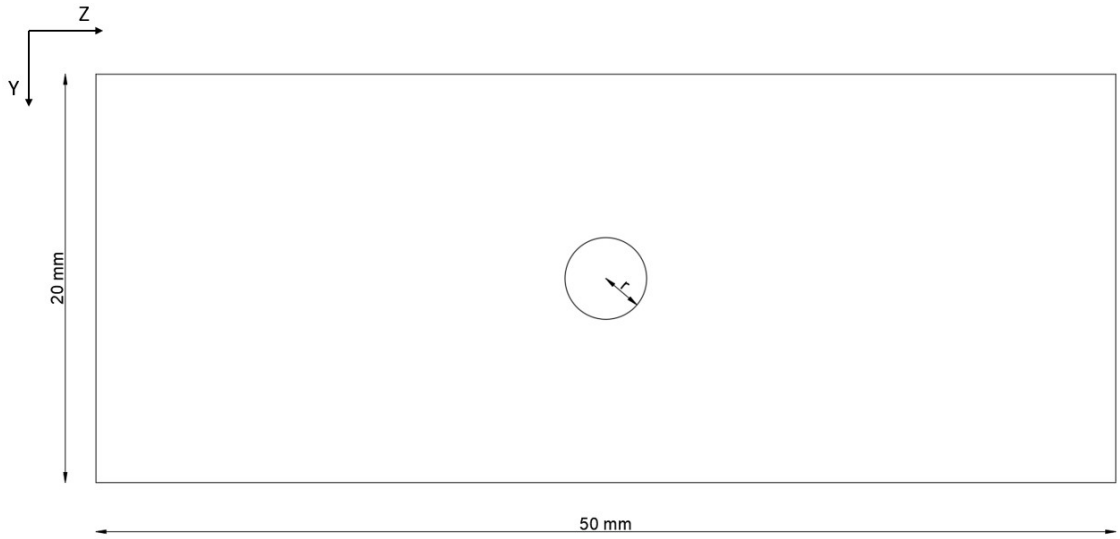

Fig. 45: Dimension of the plate under study

For this analysis we have chosen an "Isotropic linear elastic" material (steel) with the following input data:

- $E = 200000$ Mpa;
- $\nu = 0.3$

After this, an Element Group 1 is defined as a group of "2-D solid plane stress" with an element thickness of 1 mm. Thanks to the symmetry of the problem we have cut the plate by two planes (XZ-XY). On the opposite edge of the hole we have applied a pressure load of 25 MPa. The boundary conditions are defined in function of the symmetry cut plane with locking the Y and Z translation near the hole. At the end, the elements are generated with an "automatic mesh" tool and the size of element are defined with several attempts to have a solution as close as possible near the theory model.
We have made six different shape of hole in the steel plate as follow:

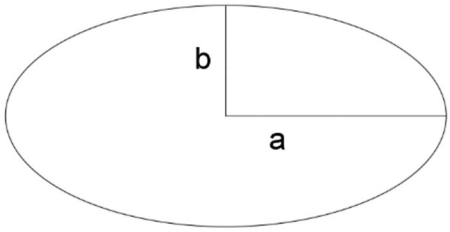

a [mm]	b [mm]	$K_{t\_theoretical}$
2	2	3
3	2	2.33
4	2	2
1.5	1.5	3
2.5	1.5	2.2
3.5	1.5	1.86

Fig. 46: Variation of Kt in function of the axis

We have applied a load pressure of 25 MPa on the edge far of the hole and being in the force control, the theoretical stress on the plate without the hole should be 25 MPa as the load. If the model works well the stress in the middle element of the plate, as far as possible from the hole and the application of the edge load, should be 25 MPa. In this model, with the small and regular element mesh the stress in the middle of the plate is effectively the same of the theory. So, to understand how much the stress intensity factor is, we have done the ratio with the max stress near the hole, from the FEM model and the theoretical stress of the plate.

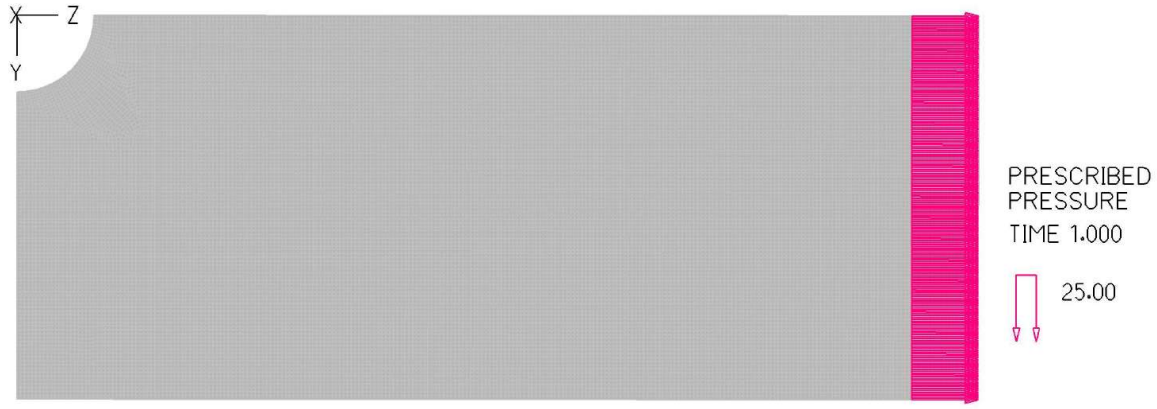

Fig. 47: One-quarter plate F.E.M model with load

Regard the element with the max stress, the FEM program give us two different value:

- The absolute max value in the element: max value on the gauss point;
- The average value in the element: average value on the gauss point;

In the following pictures we have reported the result from the FEM model.

3.1.1 Circular and elliptical hole 2 mm width

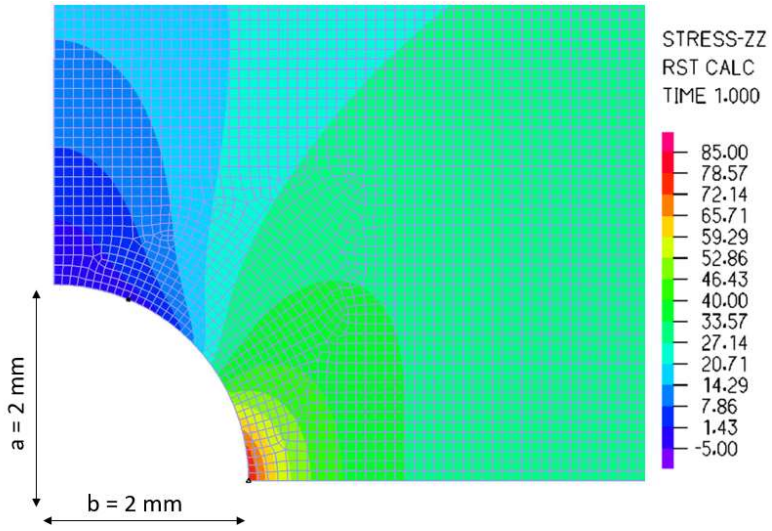

Fig. 48: Stress distribution of one-quarter plate with circular hole (a=2 mm; b=2 mm) YZ plane – detail

$\sigma_{theoretical}$ [MPa]	$\sigma_{average}$ [MPa]	K_t
25	74.35	2.97

$\sigma_{theoretical}$ [MPa]	σ_{max} [MPa]	K_t
25	82.20	3.29

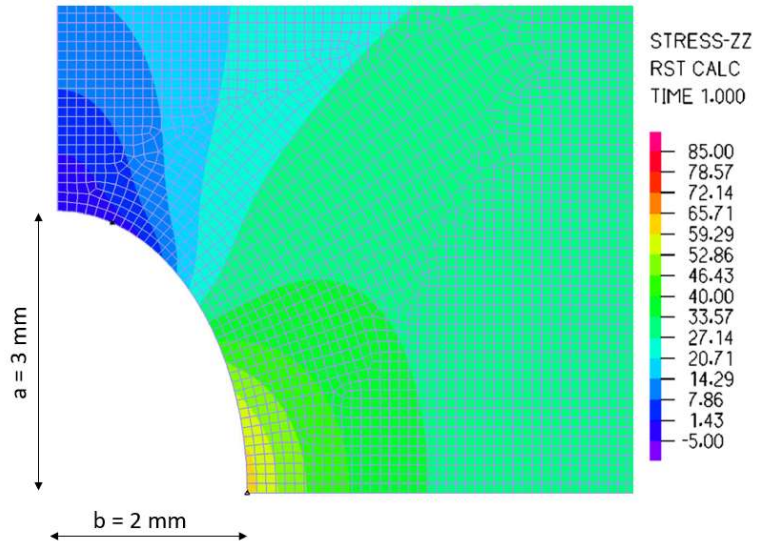

Fig. 49: Stress distribution of one-quarter plate with elliptical hole (a=3 mm; b=2 mm) YZ plane – detail

$\sigma_{theoretical}$ [MPa]	$\sigma_{average}$ [MPa]	K_t
25	60.60	2.42

$\sigma_{theoretical}$ [MPa]	σ_{max} [MPa]	K_t
25	64.02	2.56

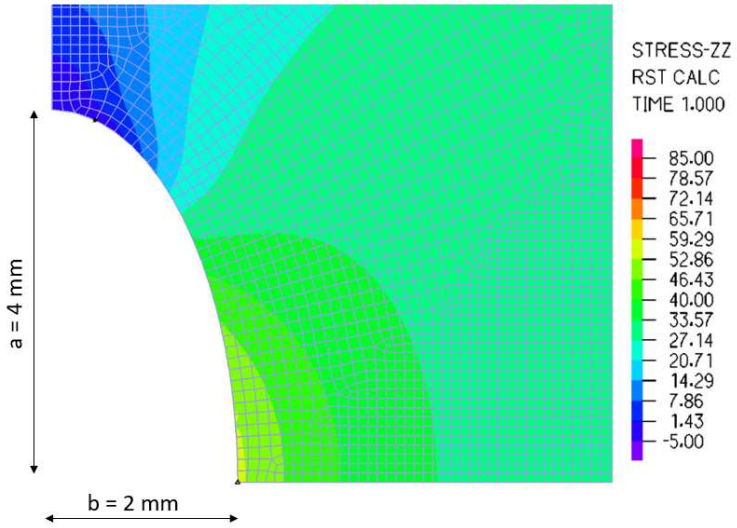

Fig. 50: Stress distribution of one-quarter plate with elliptical hole (a=4 mm; b=2 mm) YZ plane – detail

$\sigma_{theoretical}$[MPa]	$\sigma_{average}$[MPa]	K_t
25	53.40	2.14

$\sigma_{theoretical}$[MPa]	σ_{max}[MPa]	K_t
25	55.50	2.22

3.1.2 Circular and elliptical hole 1.5 mm width

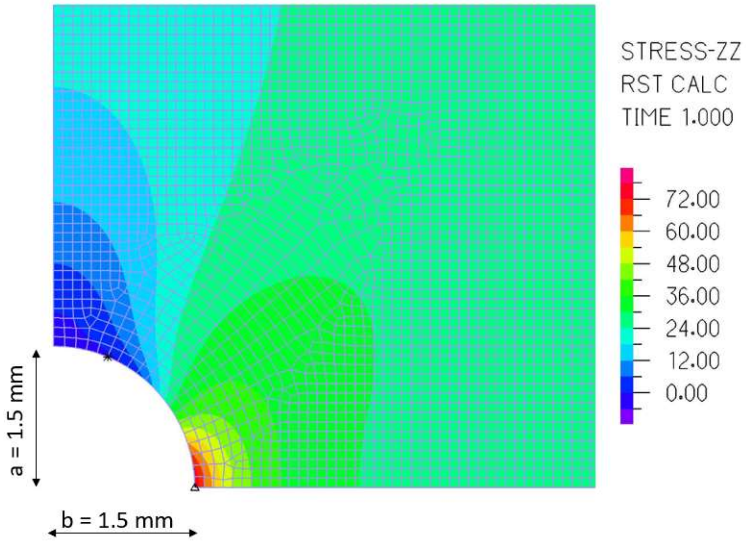

Fig. 51: Stress distribution of one-quarter plate with circular hole (a=1.5 mm; b=1.5 mm) YZ plane – detail

$\sigma_{theoretical}$[MPa]	$\sigma_{average}$[MPa]	K_t
25	71.08	2.84

$\sigma_{theoretical}$[MPa]	σ_{max}[MPa]	K_t
25	77.24	3.09

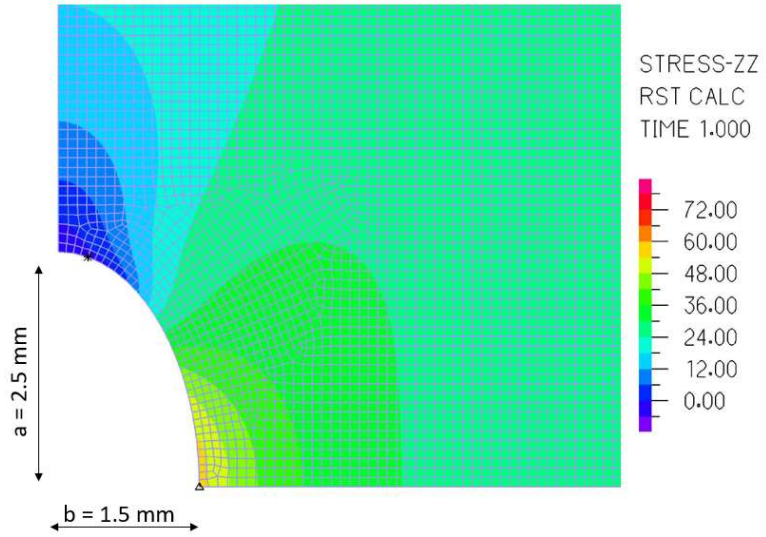

Fig. 52: Stress distribution of one-quarter plate with circular hole (a=2.5 mm; b=1.5 mm) YZ plane – detail

$\sigma_{theoretical}$[MPa]	$\sigma_{average}$[MPa]	K_t
25	55.64	2.23

$\sigma_{theoretical}$[MPa]	σ_{max}[MPa]	K_t
25	58.51	2.34

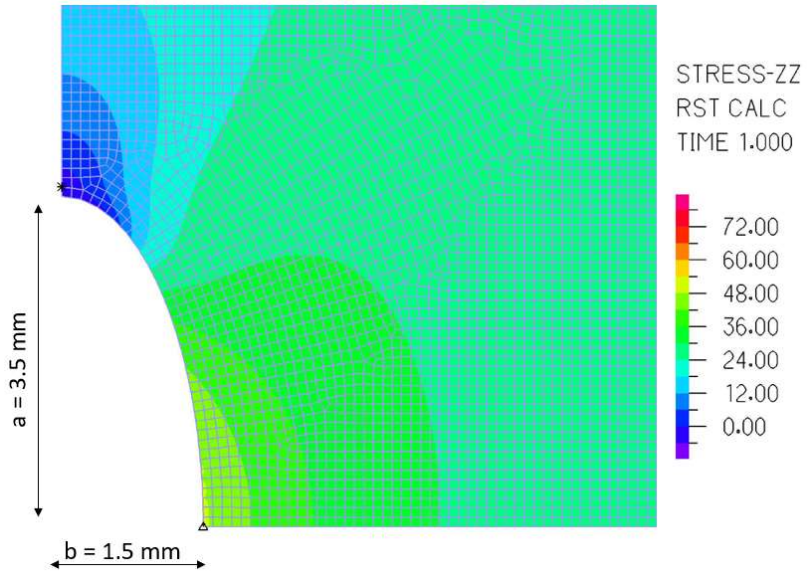

Fig. 53: Stress distribution of one-quarter plate with circular hole (a=3.5 mm; b=1.5 mm) YZ plane – detail

$\sigma_{theoretical}$[MPa]	$\sigma_{average}$[MPa]	K_t
25	48.10	1.93

$\sigma_{theoretical}$[MPa]	σ_{max}[MPa]	K_t
25	49.70	2.00

3.1.3 Slotted hole 2 mm and 1.5 mm width

How we can see from the numerical result, the value of the stress intensity factor is very similar to the theoretical model. The best solution should be to do an elliptical hole because the stress intensity factor reduces itself and lower the stress near the hole. However, in the "smart" steel bar, the hole is made by drilling the bar. Make an elliptical hole could be difficult so, another solution could be made a slotted hole that it is very simple to do than the elliptical hole. In this part, we are going to study the plate with the same condition of the previous part, but the elliptical hole is transformed in a slotted hole as following.

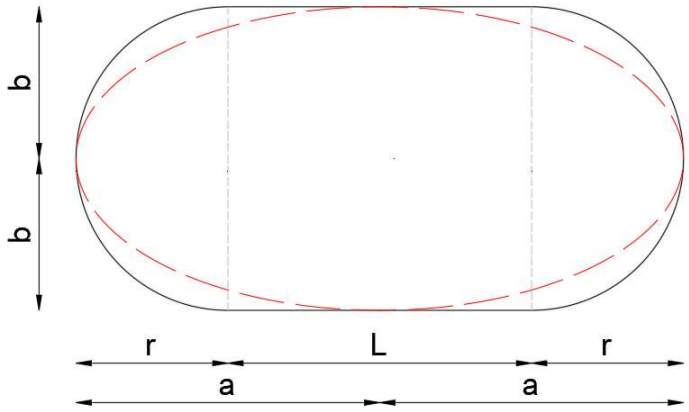

Fig. 54: From elliptical to slotted hole

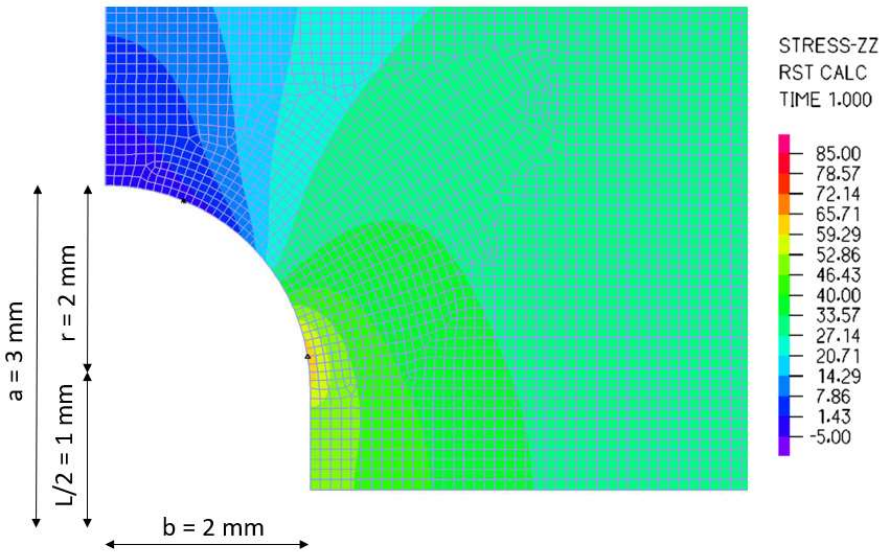

Fig. 55: Stress distribution of one-quarter plate with slotted hole (a=3 mm; b=2 mm; L/2=1 mm) YZ plane – detail

$\sigma_{theoretical}[MPa]$	$\sigma_{average}[MPa]$	K_t
25	61.57	2.46

$\sigma_{theoretical}[MPa]$	$\sigma_{max}[MPa]$	K_t
25	67.57	2.70

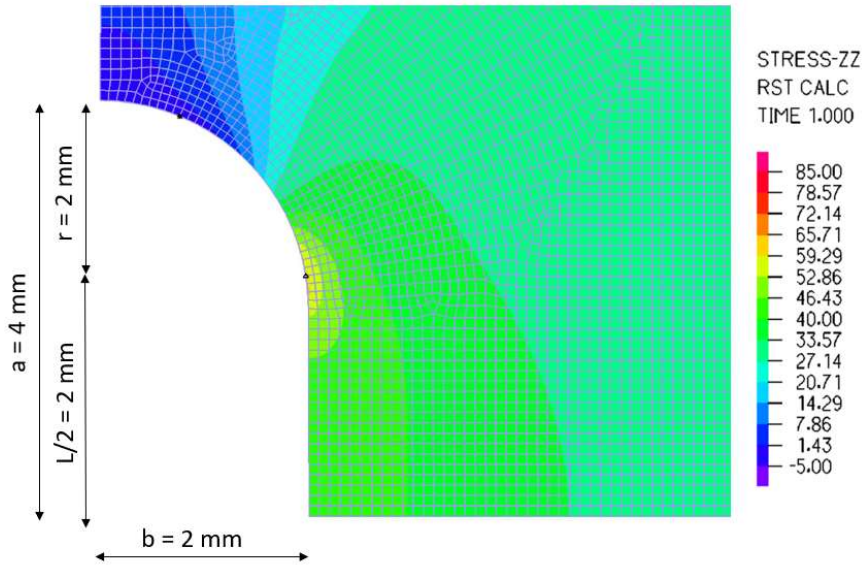

Fig. 56: Stress distribution of one-quarter plate with slotted hole (a=4 mm; b=2 mm; L/2=2 mm) YZ plane – detail

$\sigma_{theoretical}$[MPa]	$\sigma_{average}$[MPa]	K_t
25	58.95	2.36

$\sigma_{theoretical}$[MPa]	σ_{max}[MPa]	K_t
25	64.78	2.59

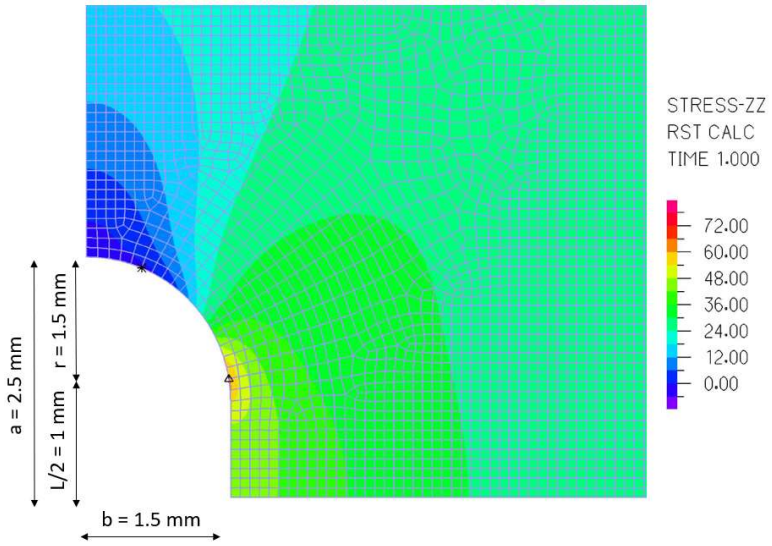

Fig. 57: Stress distribution of one-quarter plate with slotted hole (a=2.5 mm; b=1.5 mm; L/2=1 mm) YZ plane – detail

$\sigma_{theoretical}$[MPa]	$\sigma_{average}$[MPa]	K_t
25	56.61	2.26

$\sigma_{theoretical}$[MPa]	σ_{max}[MPa]	K_t
25	61.79	2.47

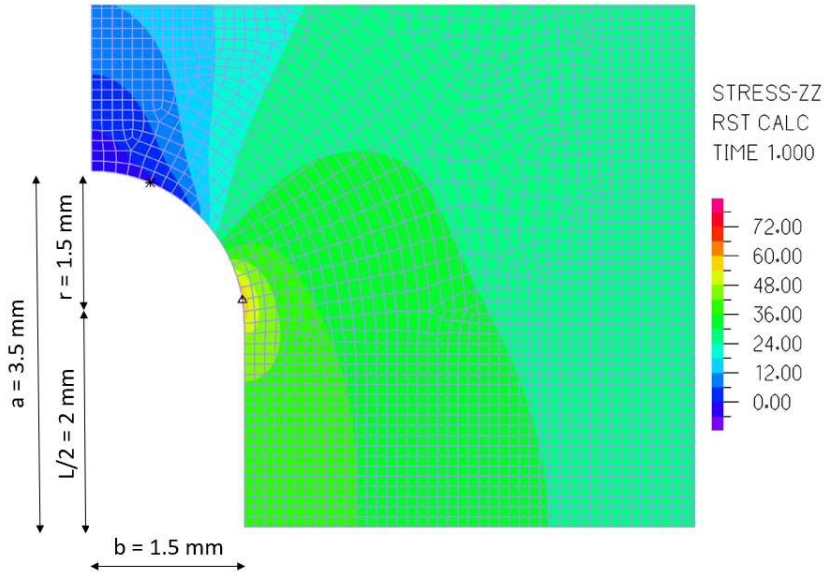

Fig. 58: Stress distribution of one-quarter plate with slotted hole (a=3.5 mm; b=1.5 mm; L/2=2 mm) YZ plane – detail

$\sigma_{theoretical}$[MPa]	$\sigma_{average}$[MPa]	K_t
25	54.21	2.17

$\sigma_{theoretical}$[MPa]	σ_{max}[MPa]	K_t
25	59.29	2.37

3.2 Smart Steel Bar FEM model with ADINA Structures

Having a good response from the plate model, in this part we have made some different model of "smart" steel bar with circular, elliptical and slotted hole, to understand how much the stress intensity factor is on the bar and how it changes, changing the form of the hole.

This Finite Element model that was crated represents a quarter of steel bar B450C Φ20, without ribs, considering two cavities, one to host the MEMS and others to take into account the space left for the electrical feed-through; The choice to create the one-quarter of steel bar is due because the cavity geometry is not symmetrical with respect to plane XZ. The cavity geometry is defined according to the real dimensions: in this FEM model, air cavity is represented by a quarter of cylinder with a diameter of 4 mm and a height of 15.5 mm. At the bottom there is a steel layer 1 mm thick, while at the top of the air cavity, another hole is modelled in order to represent the upper portion where the feed-through is placed: this is a quarter of cylinder with a diameter of 6 mm and an height of 3.5 mm (Battistoni, 2018).

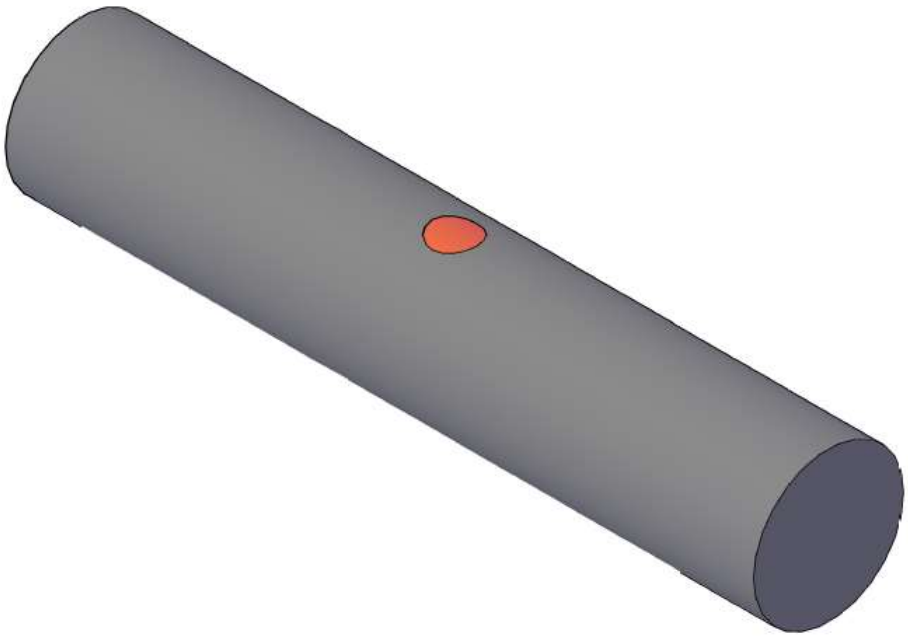

Fig. 59: Half of Φ20 Smart Steel Bar

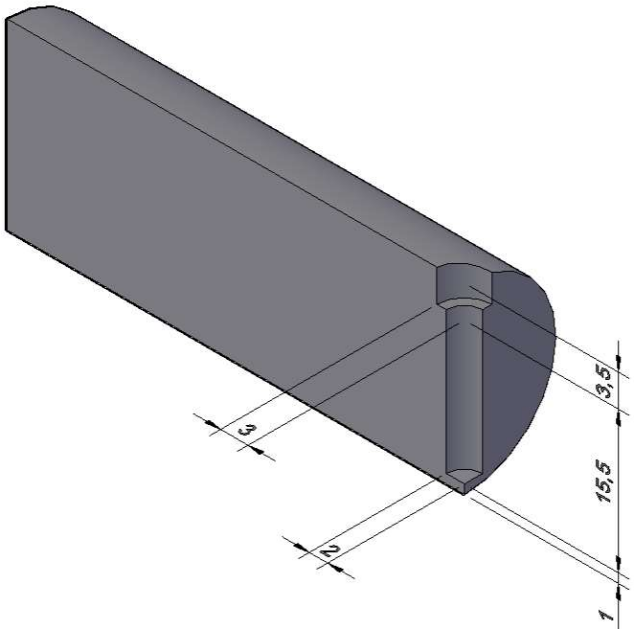

Fig. 60: A quarter of Φ20 Smart Steel Bar

For this analysis we have chosen a "plastic-multilinear" material (steel) that represent the real law obtained from the displacement control in the laboratory test in the previous campaign. The "plastic-multilinear" material (steel) input data are:

- $\mathrm{E} = 200000\ \mathrm{Mpa}$
- $\nu = 0.3$
- $\mathrm{d} = 7.85 * 10^{-6}\ \mathrm{kg/mm^3}$

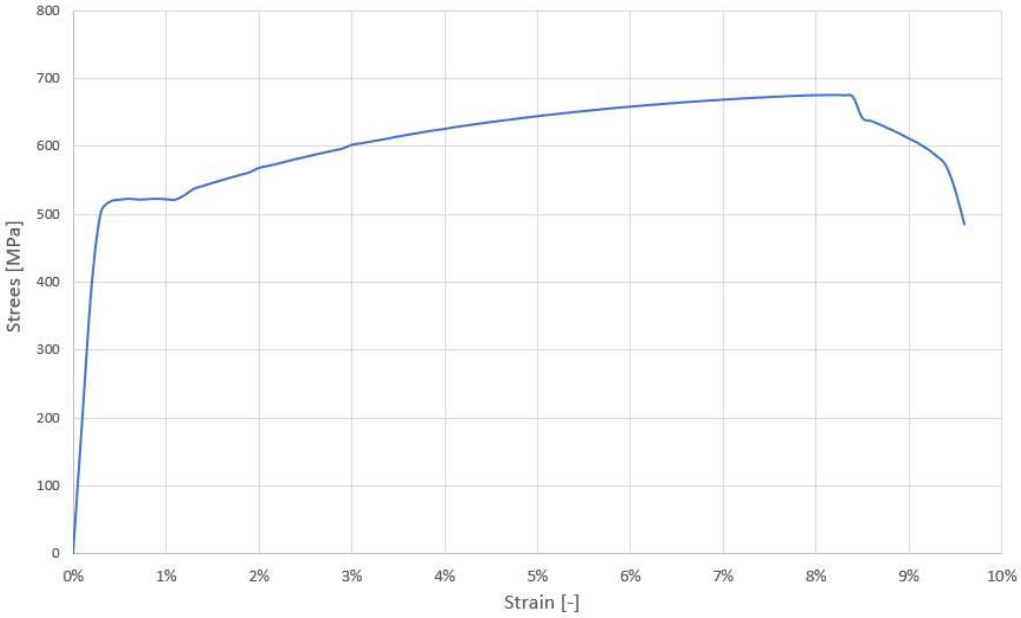

Fig. 61: Real plastic law from laboratory

So "plastic-multilinear" material (steel) is inserted and Element Group 1 is defined as a group of "3D solid" steel elements. The elements are generated with an "automatic mesh" tool, after defining the geometry of the model.
The length of the steel bar is 10 cm; is due to have a mesh as regular as possible and at the same time have a dissipation of the stress from the hole.
After we have applicated the load as displacement of 0.01 mm on the edge of quarter bar steel to leave the steel bar in the elastic field of the real law, because the maximum value of the stress intensity factor is in this part of the law, when the bar is already not in the plastic field. In the following pictures we can see the FEM model and its deformed shape.

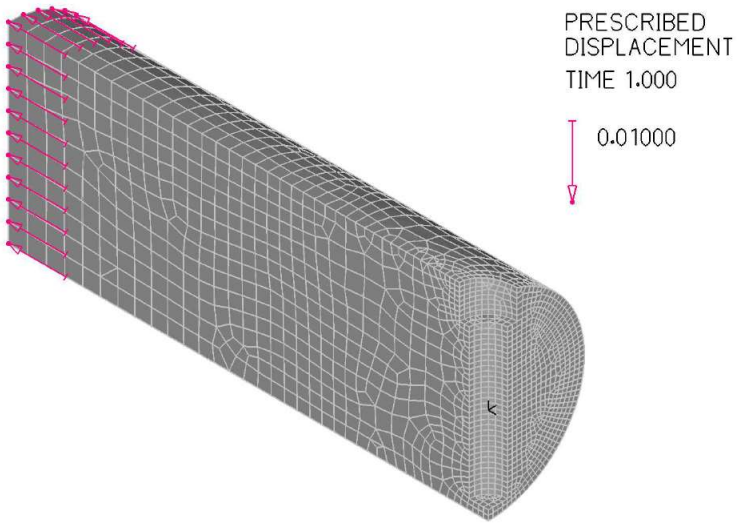

Fig. 62: One-quarter steel bar (EG1) geometry

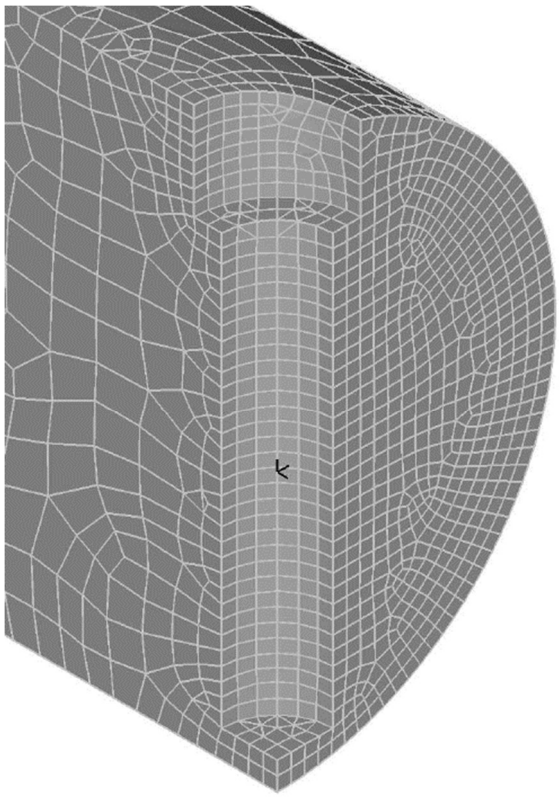

Fig. 63: One-quarter steel bar (EG1) geometry - detail

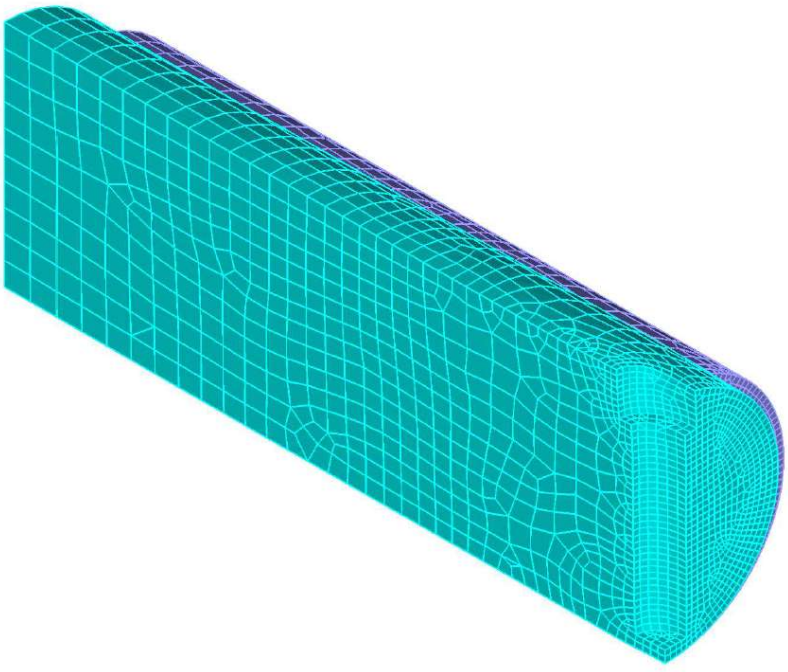

Fig. 64: Deformed one-quarter steel bar (EG1) axonometric projection

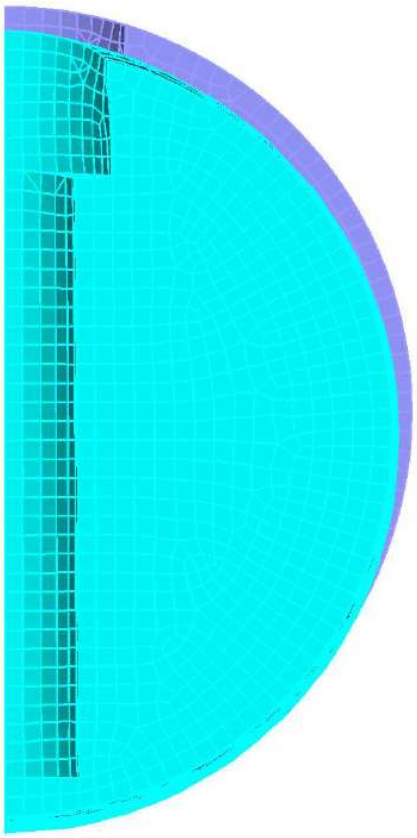

Fig. 65: Deformed one-quarter steel bar (EG1) orthogonal projection (XY)

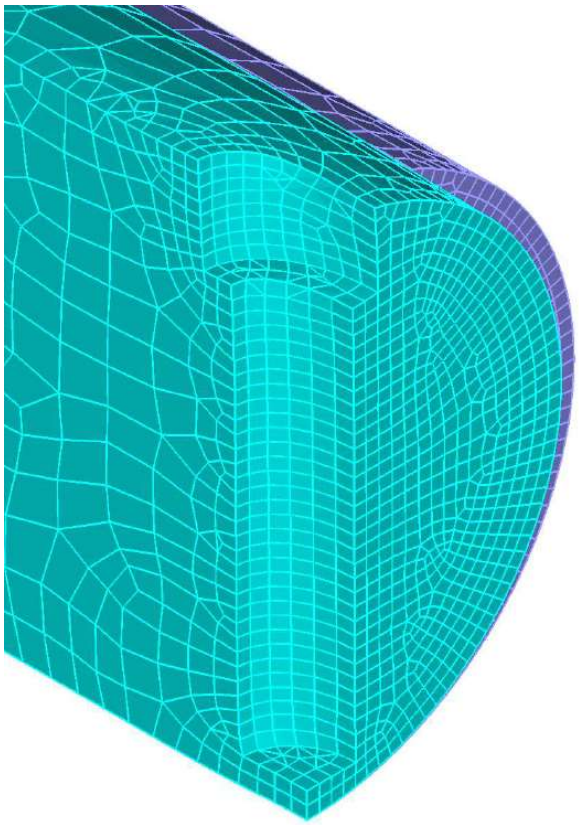

Fig 66: Deformed one-quarter steel bar (EG1) axonometric projection - detail

With the 0.01 mm of displacement the theoretical stress make in the bar is:

$$\sigma = \frac{\text{Displacement}}{\text{Lenght of the bar}} \cdot \text{Elastic module} = \frac{0.01\ [\text{mm}]}{50\ [\text{mm}]} \cdot 200000\ [\text{MPa}] = 40\ [\text{MPa}]$$

In the follow figure we can see the stress graphic output of the program. We can notice how the tension is really concentrated on the edge of the hole in the perpendicular direction of application of the load.

How in the case of the plate model we have reported two result of the stress:

- The absolute max value in the element;
- The average value in the element;

To find the stress intensity factor we have done the ratio between the maximum value of the stress near the hole, and the theoretical stress 40 MPa, that is also the stress in the generic element of the bar F.E.M model.

How in the case of the plate, we work of the form of the hole by varying the axes a and b.

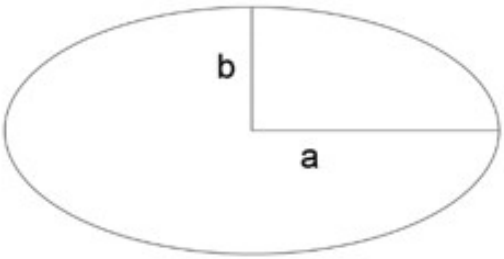

Fig. 67: Axes a and b of the hole

3.2.1 Circular, Elliptical and Slotted hole 2 mm width

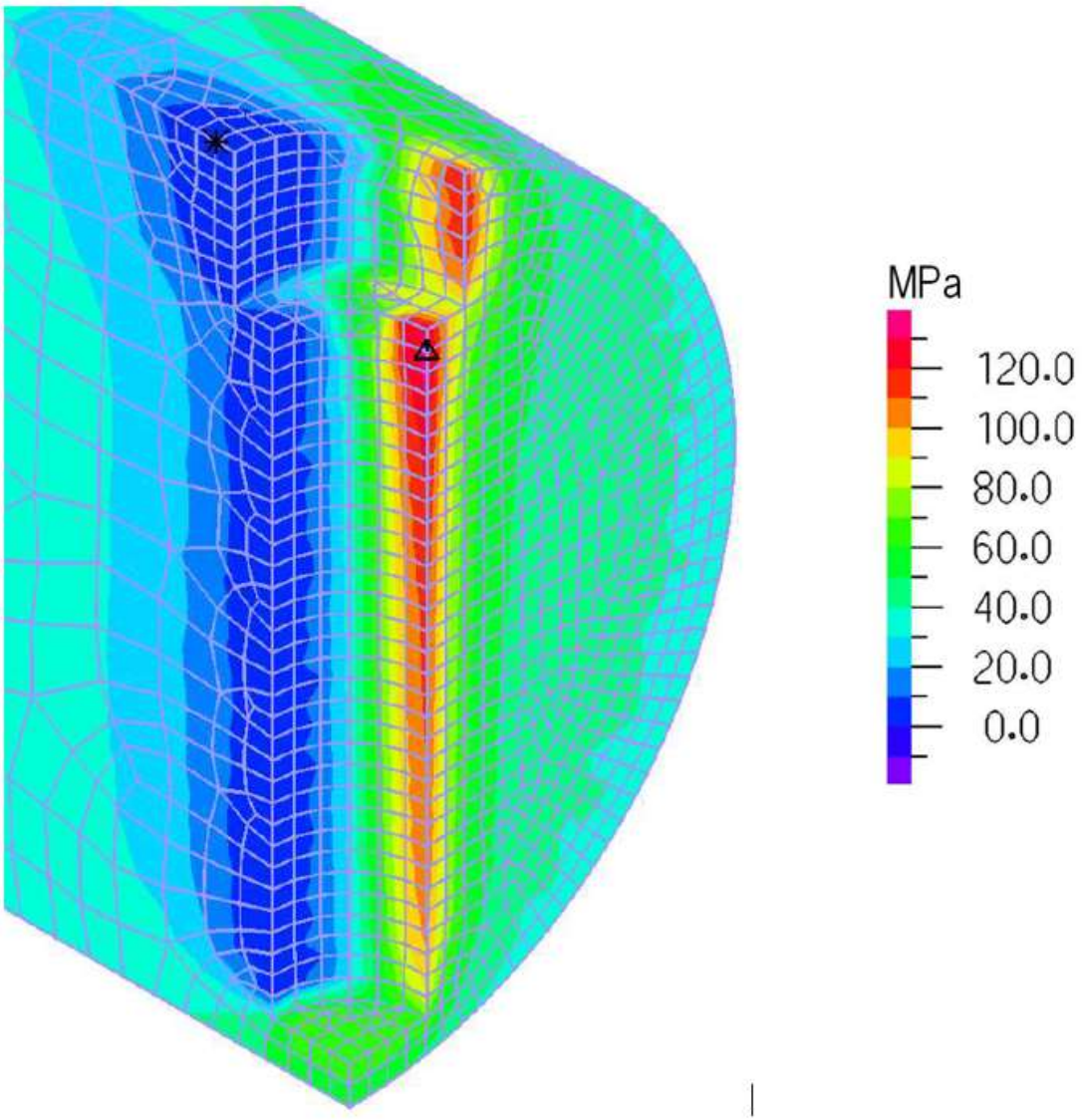

Fig. 68: Stress distribution of one-quarter steel bar with circular hole (a=2 mm; b=2 mm) axonometric projection – detail

$\sigma_{\text{theoretical full section}}$ [MPa]	$\sigma_{\text{average hole}}$ [MPa]	K_t
40	119.31	2.98

$\sigma_{\text{theoretical full section}}$ [MPa]	$\sigma_{\text{max hole}}$ [MPa]	K_t
40	137.6	3.44

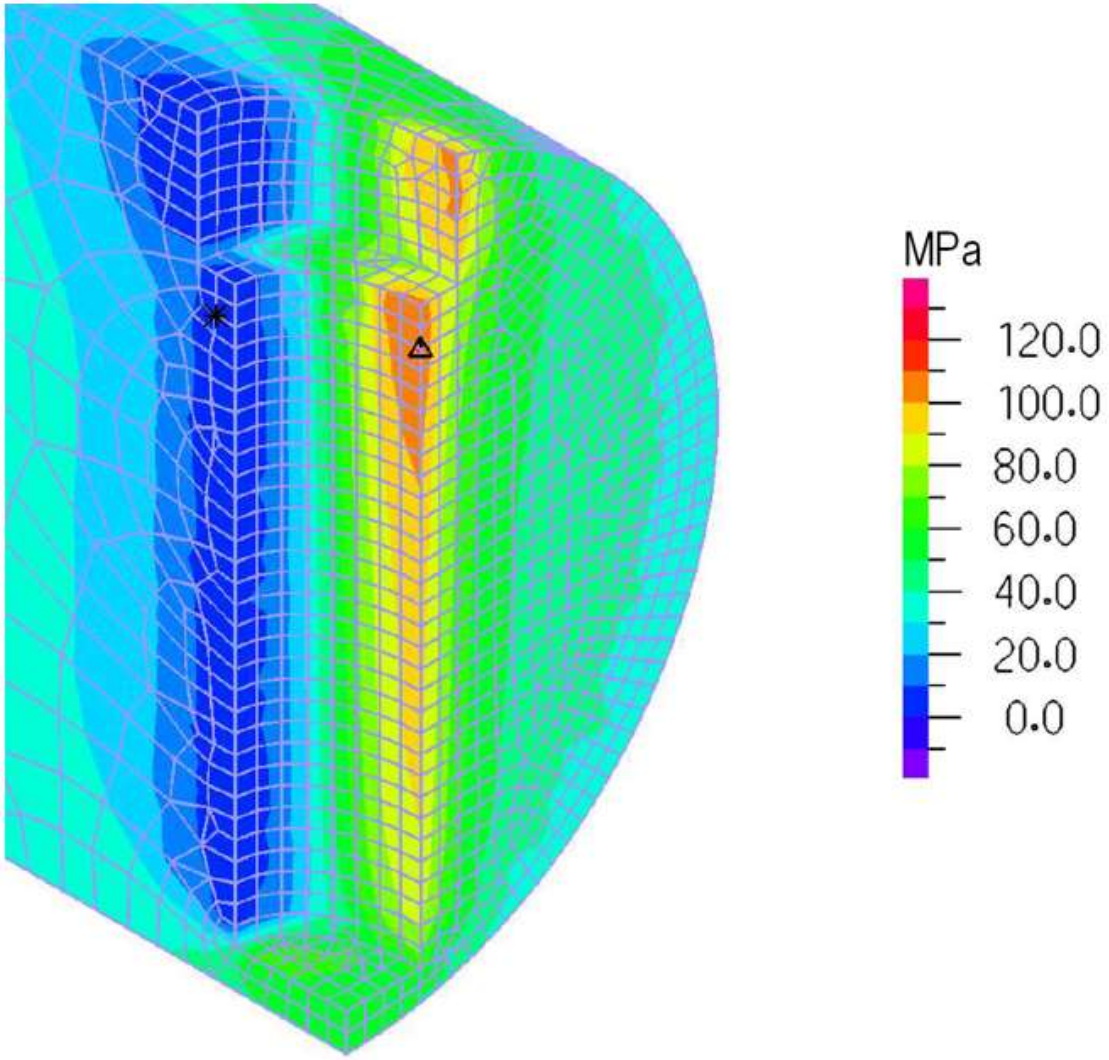

Fig. 69: Stress distribution of one-quarter steel bar with elliptical (a=3 mm; b=2 mm) axonometric projection – detail

$\sigma_{\text{theoretical}}$ [MPa] full section	σ_{average} [MPa] hole	K_t
40	103.00	2.58

$\sigma_{\text{theoretical}}$ [MPa] full section	σ_{max} [MPa] hole	K_t
40	110.90	2.77

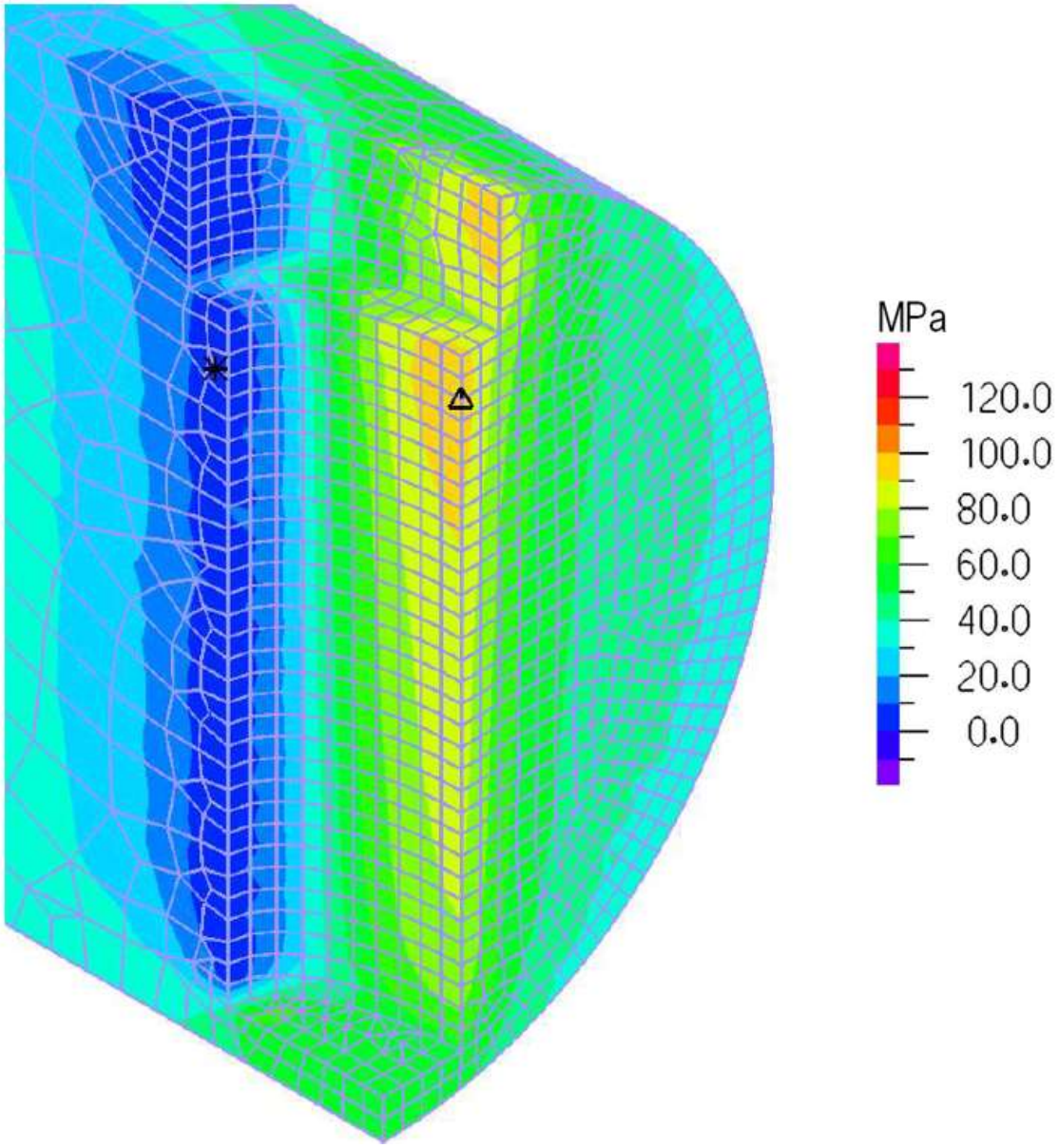

Fig. 70: Stress distribution of one-quarter steel bar with elliptical (a=4 mm; b=2 mm) axonometric projection – detail

$\sigma_{\text{theoretical}}$ [MPa] full section	σ_{average} [MPa] hole	K_t
40	92.59	2.31

$\sigma_{\text{theoretical}}$ [MPa] full section	σ_{max} [MPa] hole	K_t
40	97.61	2.44

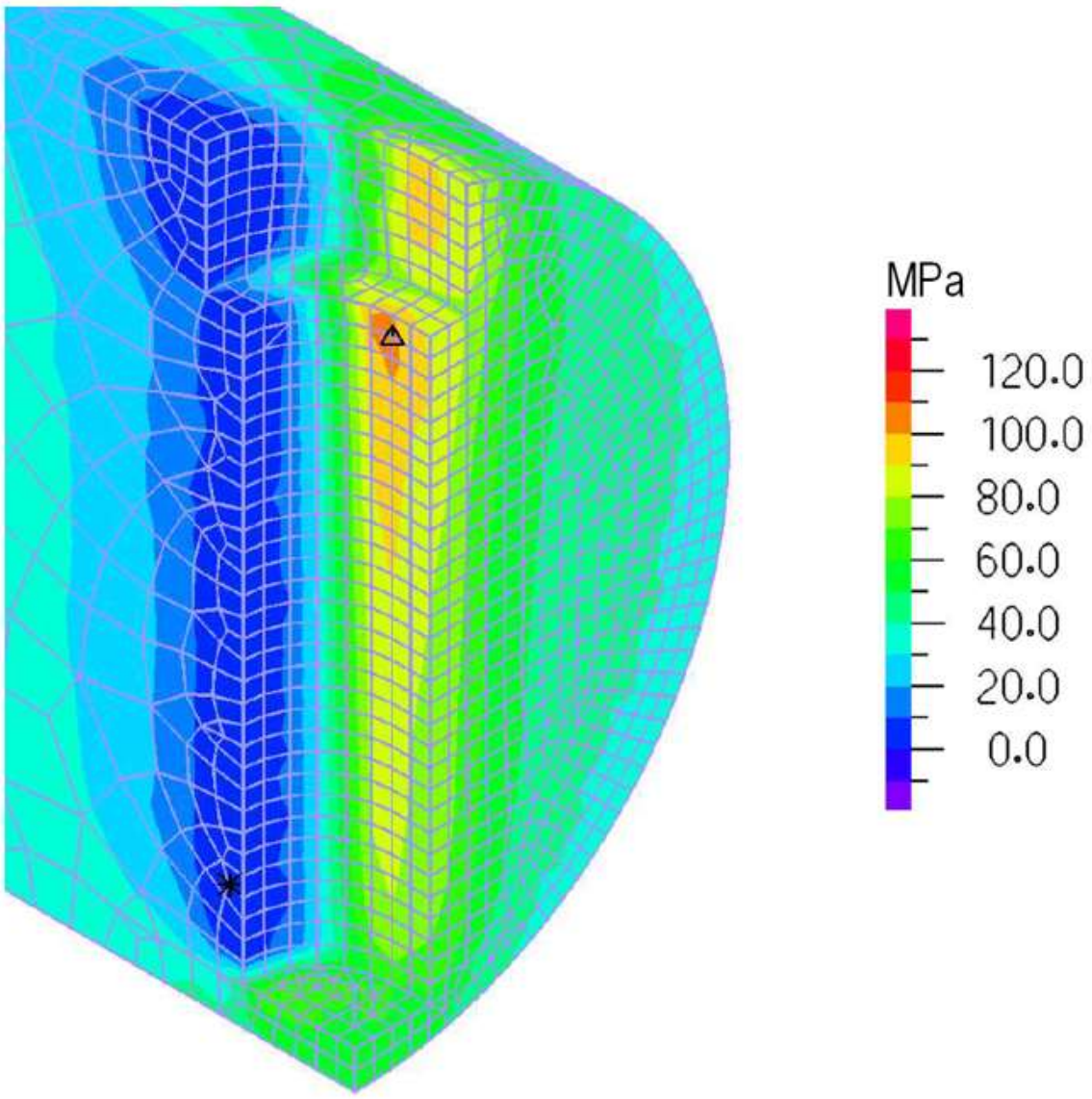

Fig: 71: Stress distribution of one-quarter steel bar with slotted hole (a=3 mm; b=2 mm; L/2=1 mm) axonometric projection – detail

$\sigma_{\text{theoretical}}$ [MPa] full section	σ_{average} [MPa] hole	K_t
40	96.88	2.42

$\sigma_{\text{theoretical}}$ [MPa] full section	σ_{max} [MPa] hole	K_t
40	109.7	2.74

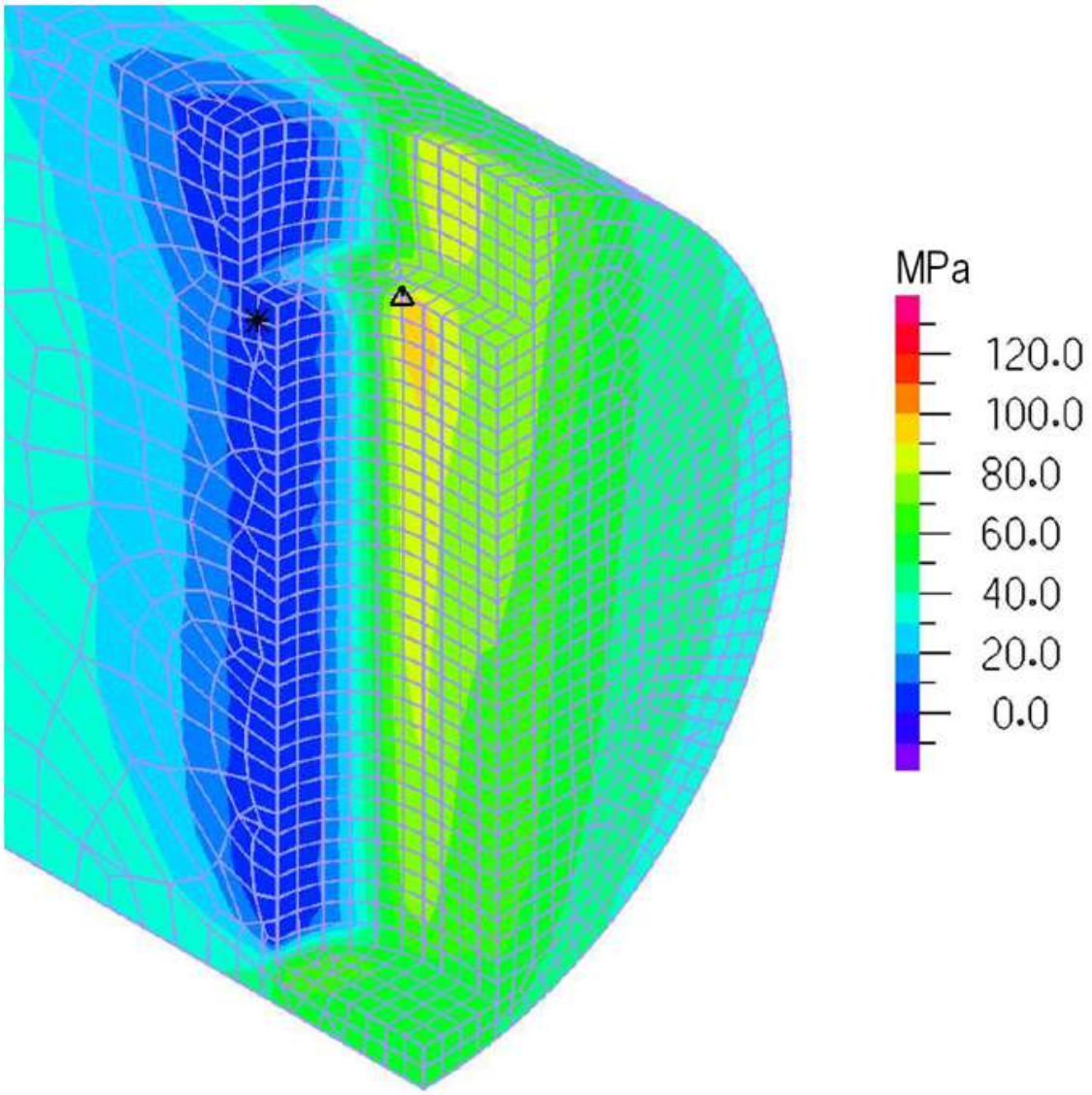

Fig. 72: Stress distribution of one-quarter steel bar with circular hole (a=4 mm; b=2 mm; L/2=2 mm) axonometric projection – detail

$\sigma_{\text{theoretical}}$ [MPa] full section	σ_{average} [MPa] hole	K_t
40	90.70	2.27

$\sigma_{\text{theoretical}}$ [MPa] full section	σ_{max} [MPa] hole	K_t
40	103.20	2.58

3.2.2 Circular, Elliptical and Slotted hole 1.5 mm width

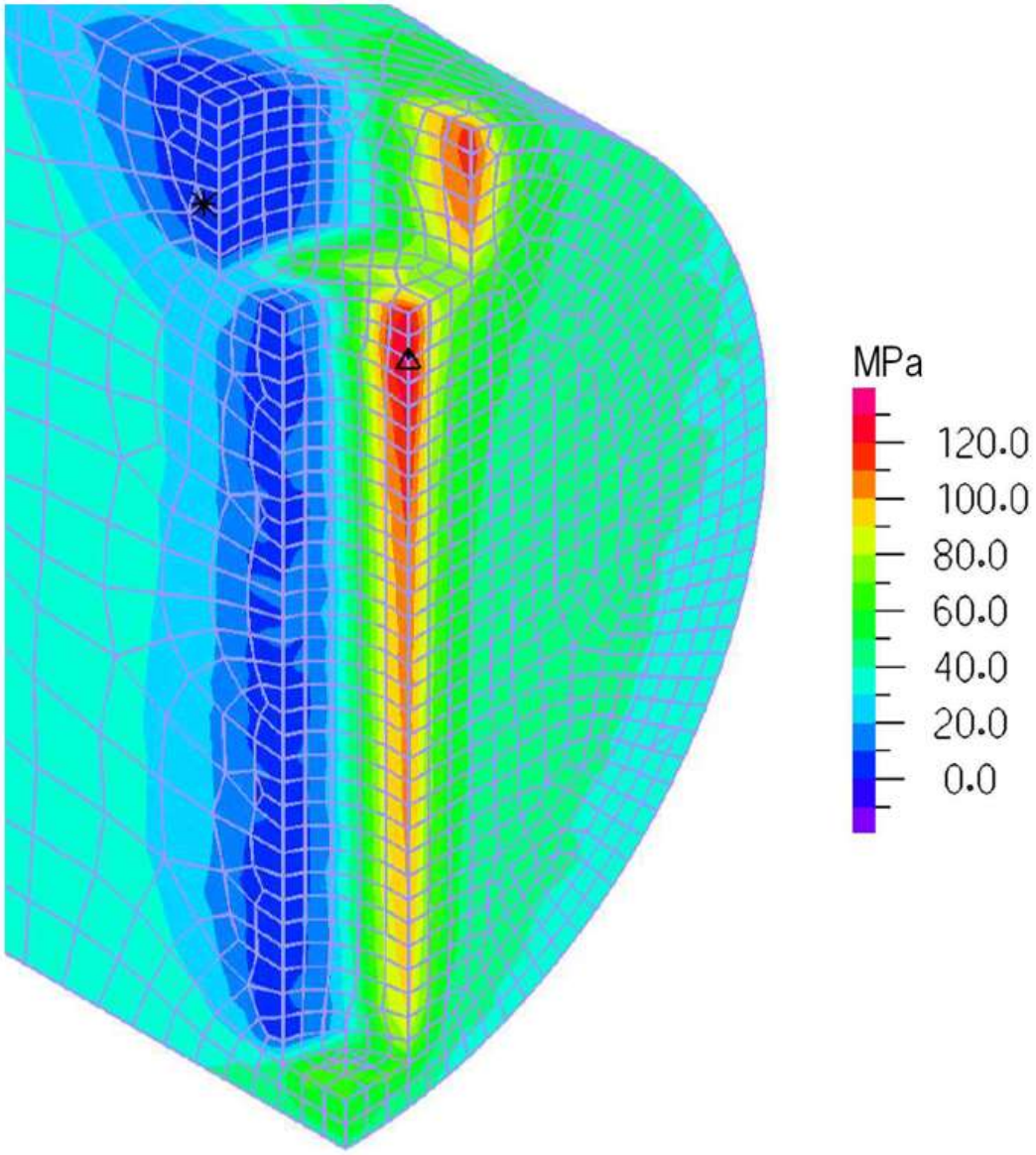

Fig. 73: Stress distribution of one-quarter steel bar with circular hole (a=1.5 mm; b=1.5 mm) axonometric projection – detail

$\sigma_{\text{theoretical}}$ [MPa] full section	σ_{average} [MPa] hole	K_t
40	112.66	2.82

$\sigma_{\text{theoretical}}$ [MPa] full section	σ_{max} [MPa] hole	K_t
40	132.60	3.32

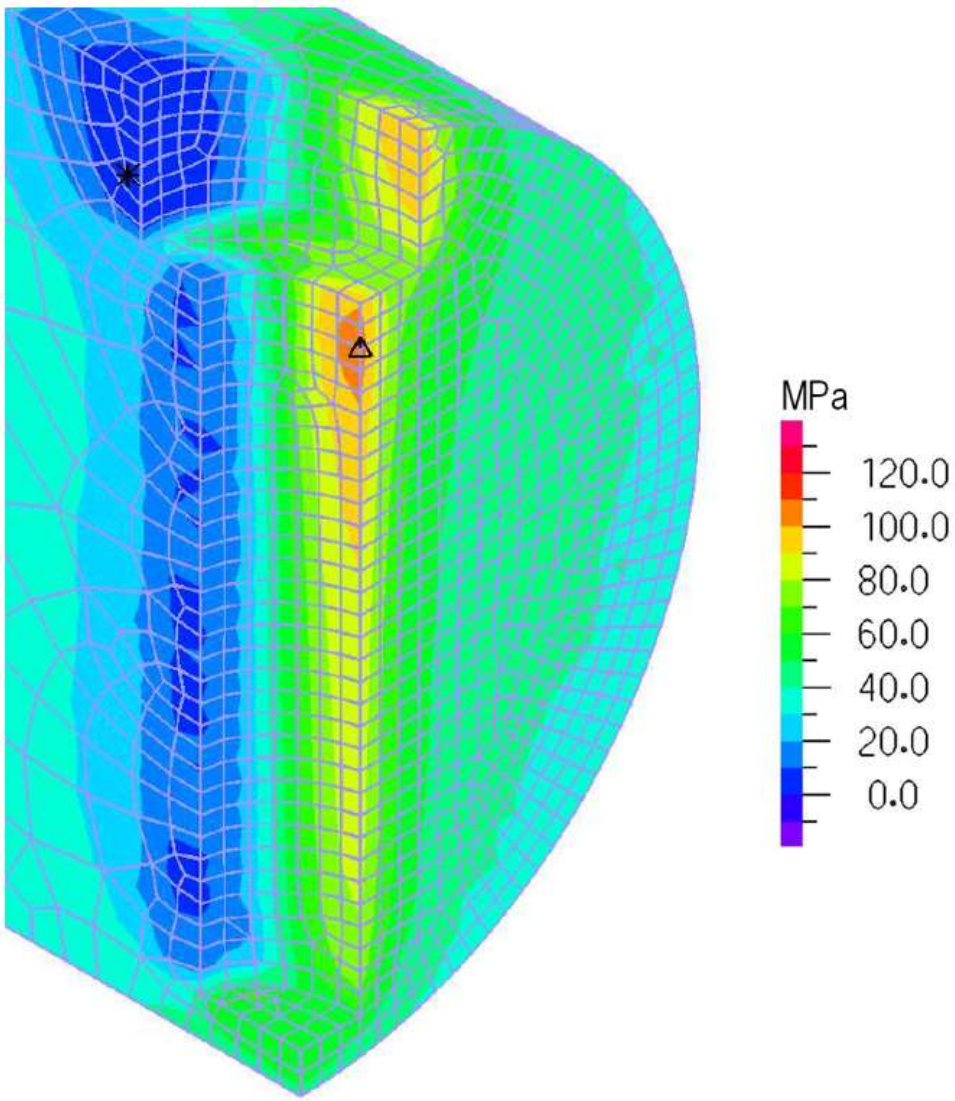

Fig. 74: Stress distribution of one-quarter steel bar with circular hole (a=2.5 mm; b=1.5 mm) axonometric projection – detail

$\sigma_{\text{theoretical full section}}$ [MPa]	$\sigma_{\text{average hole}}$ [MPa]	K_t
40	96.92	2.42

$\sigma_{\text{theoretical full section}}$ [MPa]	$\sigma_{\text{max hole}}$ [MPa]	K_t
40	105.3	2.63

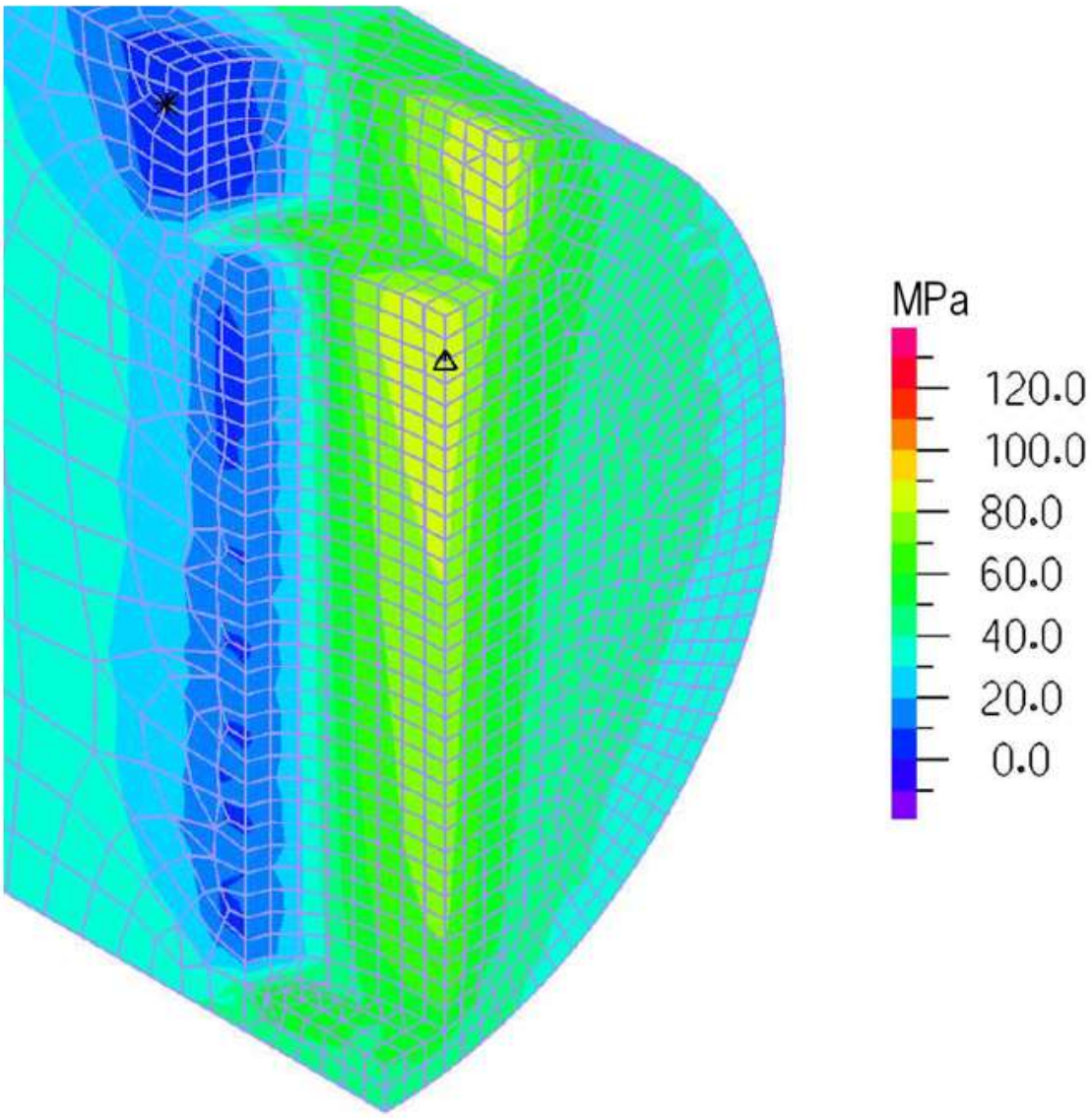

Fig. 75: Stress distribution of one-quarter steel bar with circular hole (a=3.5 mm; b=1.5 mm) axonometric projection – detail

$\sigma_{theoretical\ full\ section}$ [MPa]	$\sigma_{average\ hole}$ [MPa]	K_t
40	85.84	2.15

$\sigma_{theoretical\ full\ section}$ [MPa]	$\sigma_{max\ hole}$ [MPa]	K_t
40	90.60	2.27

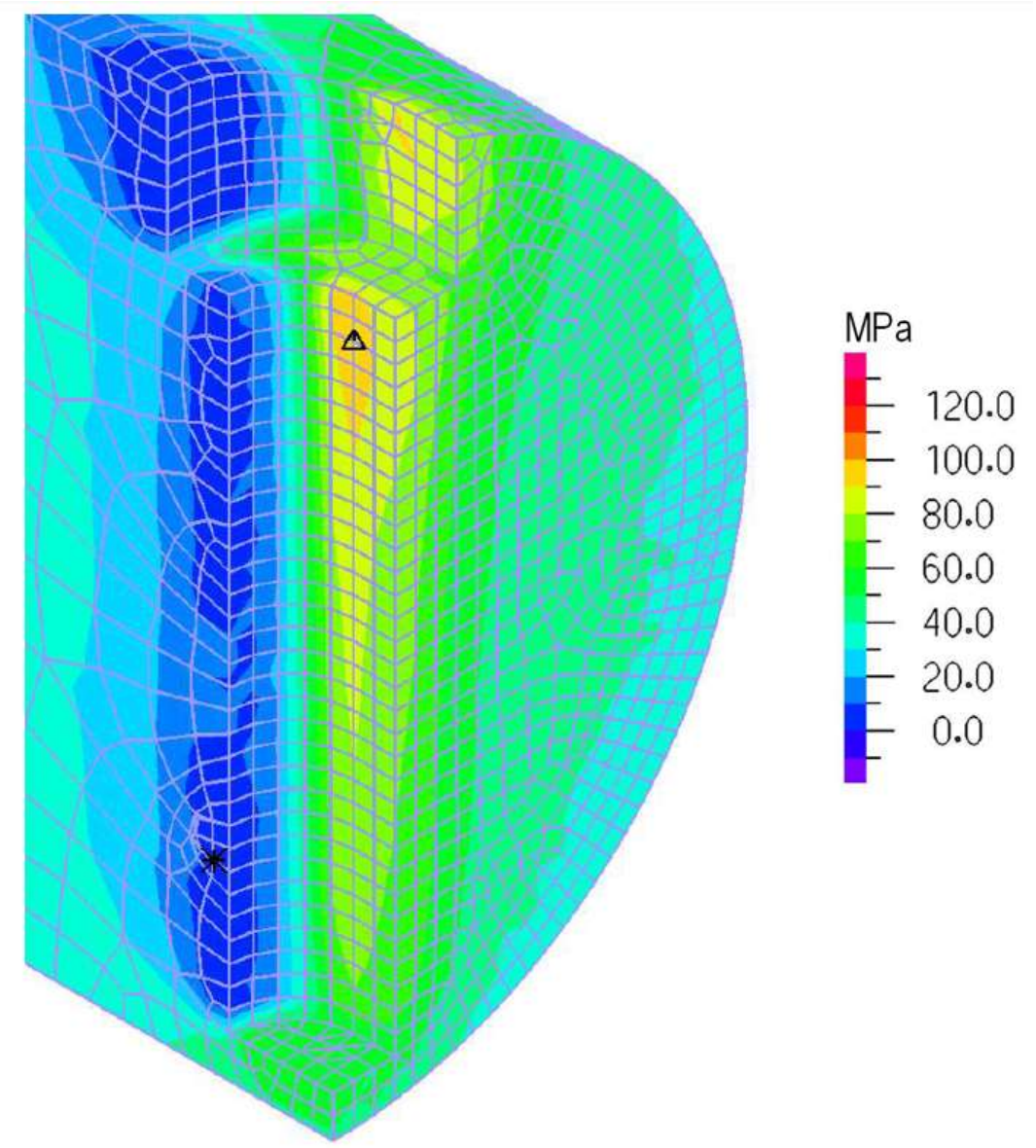

Fig. 76: Stress distribution of one-quarter steel bar with slotted hole (a=2.5 mm; b=1.5 mm; L/2=1 mm) axonometric projection – detail

$\sigma_{\text{theoretical}}$ [MPa] full section	σ_{average} [MPa] hole	K_t
40	91.23	2.28

$\sigma_{\text{theoretical}}$ [MPa] full section	σ_{max} [MPa] hole	K_t
40	99.03	2.48

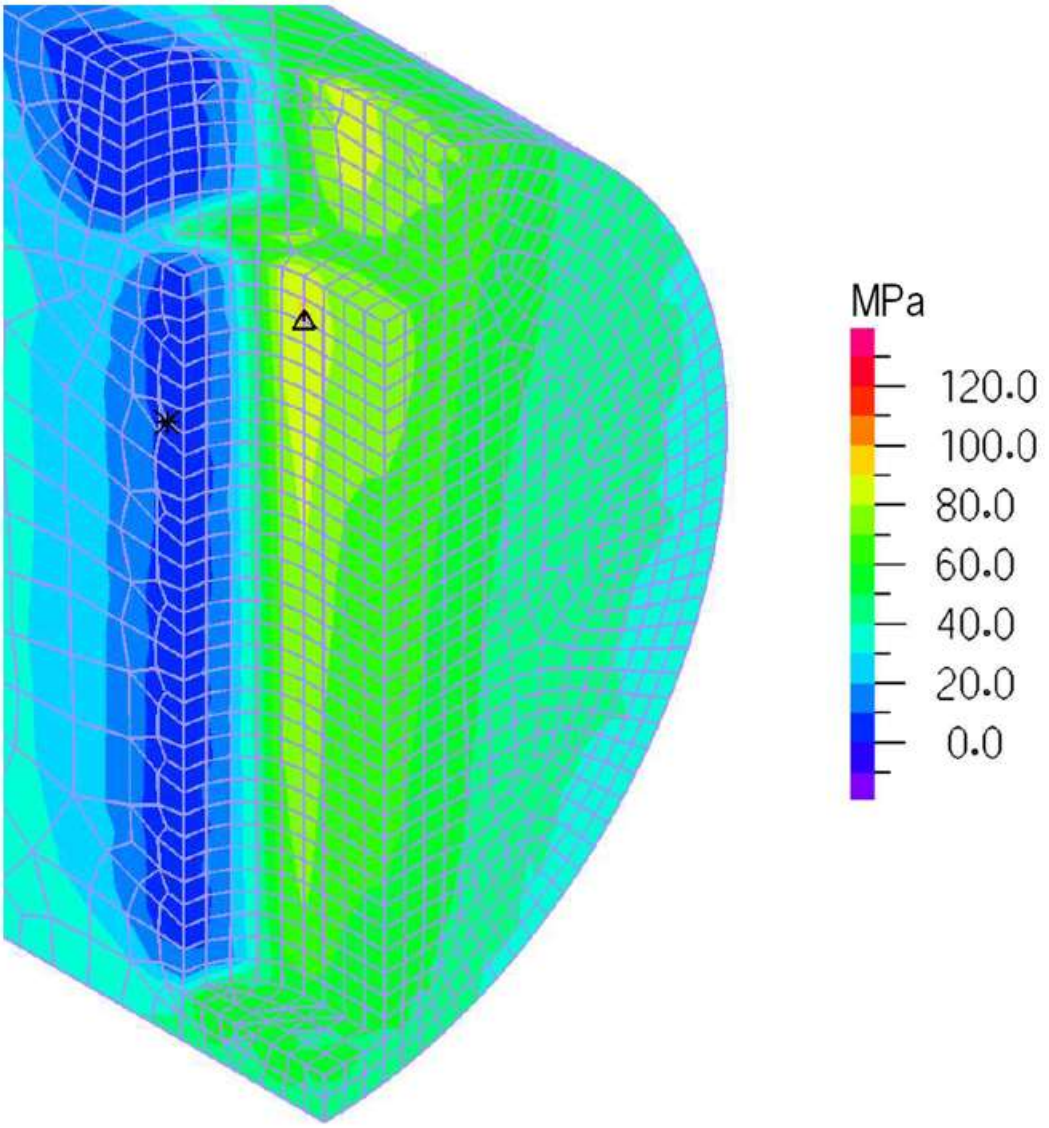

Fig. 77: Stress distribution of one-quarter steel bar with slotted hole (a=3.5 mm; b=1.5 mm; L/2=2 mm) axonometric projection – detail

$\sigma_{\text{theoretical}}$ [MPa] full section	σ_{average} [MPa] hole	K_t
40	84.06	2.10

$\sigma_{\text{theoretical}}$ [MPa] full section	σ_{max} [MPa] hole	K_t
40	92.22	2.31

3.3 Comparison of the F.E.M models

In the following table is possible to see all results from the F.E.M model. We can see that the numerical model has a good response both plate and "smart" bar and stretching the hole, the stress reduces itself in according with theoretical formulation. Is possible to see that doing a slotted hole the stress intensity factor is very close to a situation with the elliptical hole; so, making a slotted hole could be good and easy solution to lower the stress. Another solution to lower the stress is to reduce the dimension of the hole. Indeed, changing the radius of the hole from 2 mm to 1.5 mm, we notice a lower value of Kt.

Plate with radius hole of 2 mm	$K_{t,average}$	$K_{t,max}$
Plate circular hole (a=2; b=2)	2.97	3.29
Plate elliptical hole (a=3; b=2; L/2=1)	2.42	2.56
Plate elliptical hole (a=4; b=2; L/2=2)	2.14	2.22
Plate slotted hole (a=3; b=2; L/2=1)	2.46	2.70
Plate slotted hole (a=4; b=2; L/2=2)	2.36	2.59

Steel bar with radius hole of 2 mm	$K_{t,average}$	$K_{t,max}$
Bar circular hole (a=2; b=2)	2.98	3.44
Bar Elliptical hole (a=3; b=2; L/2=1)	2.58	2.77
Bar Elliptical hole (a=4; b=2; L/2=2)	2.31	2.44
Bar slotted hole (a=3; b=2; L/2=1)	2.42	2.74
Bar slotted hole (a=4; b=2; L/2=2)	2.27	2.58

Plate with radius hole of 1.5 mm	$K_{t,average}$	$K_{t,max}$
Plate circular hole (a=1.5; b=1.5)	2.84	3.09
Plate elliptical hole (a=2.5; b=1.5; L/2=1)	2.23	2.34
Plate elliptical hole (a=3.5; b=1.5; L/2=2)	1.93	2.00
Plate slotted hole (a=2.5; b=1.5; L/2=1)	2.26	2.47
Plate slotted hole (a=3.5; b=1.5; L/2=2)	2.17	2.37

Steel bar with radius hole of 1.5 mm	$K_{t,average}$	$K_{t,max}$
Bar circular hole (a=1.5; b=1.5)	2.82	3.32
Bar Elliptical hole (a=2.5; b=1.5; L/2=1)	2.42	2.63
Bar Elliptical hole (a=3.5; b=1.5; L/2=2)	2.15	2.27
Bar slotted hole (a=2.5; b=1.5; L/2=1)	2.28	2.48
Bar slotted hole (a=3.5; b=1.5; L/2=2)	2.10	2.31

We need to do some consideration about this result, because when we think about a reinforced bar for concrete, we know that the common steel bar is not a smooth bar, but on his surface, it has some ribs distributed along the entire length.
The ribs are realised in order to guarantee an optimal collaboration between the steel bar and the concrete, thereby to increase the contact surface between the two materials and avoiding pull out problems; the ribs directions are variable along the bar length and the combination of these different inclinations is a sort of code, which indicates additional information about the steel bar. That said, the ribs represent a geometric discontinuity and it is interesting to understand if they provoke high stresses concentration in bars. Thanks to a previous study (Nunes, 2014), is possible to understand how different bar's geometric characteristics influence the placement and the magnitude of these singularities.

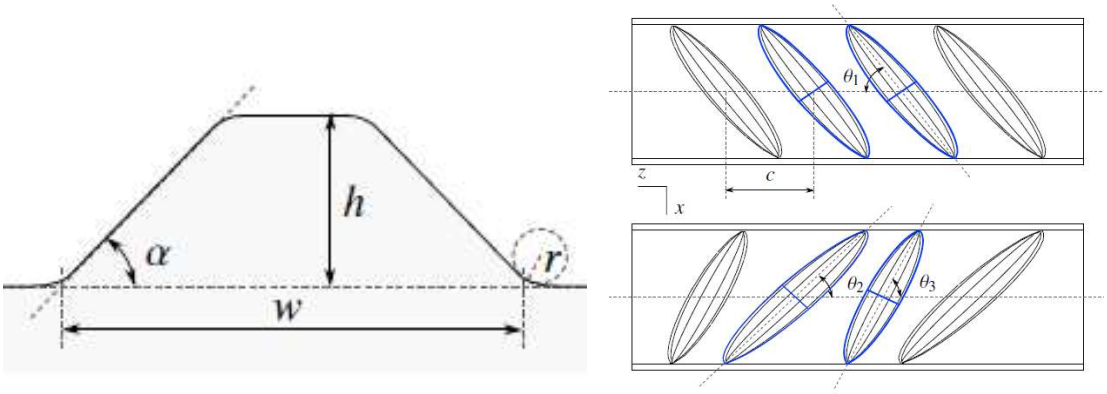

Fig. 78: conformation of general ribs on the steel bar

K_t is the factor defined as the ratio between the local stress at the rib and the stress assumed to be uniformly distributed over the total cross section. The max value of K_t is in the radius zone (r), where the bar connects to the rib. This part takes the name as Transition Line (TL); before and after TL, the maximum values are reduced a little and then the singularity ends when the geometry becomes regular again. The rib doesn't present stresses concentration and it is almost unloaded at its centre, because the stress flow mostly stays within bar's circumference.

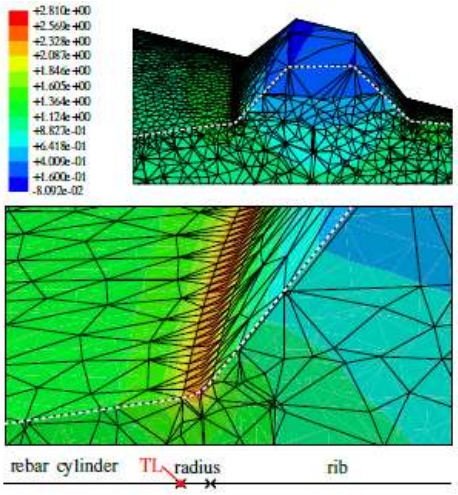

Fig. 79: Numerical result of the stress on the rib

According with the numerical result (Nunes, 2014), we can say that the most important parameters that influence the value of the stress concentration factor (K_t) are:

- r: an increase of curvature radius connecting rib and bar provokes a reduction of the maximum value of stresses concentration; doubling the radius, there is a decrease of about 15%;
- h: reduction a high of the rib has as consequence a decrease of the maximum value of stress and also an increase of the singularity zone width;
- D: the increase of bar diameter also influences the stresses concentration, by inducing a higher maximum value;
- c: a change of spacing has no significant influence, compared with to other parameters; however, a reduction of c, in case of non-uniform ribs it provokes an augmentation of the stress maximum value and so it is important to avoid this solution.
- θ: the ribs inclination has almost no influence on the maximum value of stresses concentration factor, but it changes its position along the Transition Line.

In the following picture we can see the numerical results from the previous study (Nunes, 2014), where are listed the PV (pick value: max value of Kt) and the PP (pick position) on each numerical model crated.

Models	Rib inclination θ					
	46°		54°		64°	
	PV	PP	PV	PP	PV	PP
D10h03r02	1.56	0.82	1.61	0.71	1.63	0.64
D10h08r02	1.90	0.82	1.90	0.73	1.89	0.63
D10h08r04	1.59	0.79	1.61	0.73	1.64	0.64
D10h15r02	2.44	0.76	2.36	0.73	2.37	0.67
D10h15r04	2.19	0.74	1.92	0.70	2.13	0.55
D10h08	2.15	0.81	2.27	0.75	2.25	0.65
D16h03r02	1.72	0.82	1.79	0.71	1.83	0.63
D16h08r02	2.09	0.81	2.15	0.76	2.15	0.68
D16h08r04	1.76	0.80	1.78	0.72	1.80	0.63
D16h08r08	1.53	0.79	1.54	0.73	1.56	0.63
D16h15r02	2.79	0.77	2.68	0.72	2.74	0.62
D16h15r04	2.28	0.76	2.18	0.70	2.26	0.53
D16h15r08	1.99	0.74	1.87	0.67	1.97	0.47
D16h08	2.45	0.81	2.48	0.76	2.48	0.68
D16h08r04c04	1.95	0.76	1.81	0.67	1.98	0.35
D16h08r04c12	1.74	0.82	1.75	0.75	1.77	0.68
D26h03r02	1.95	0.80	2.04	0.72	2.09	0.62
D26h08r02	2.46	0.82	2.45	0.75	2.50	0.68
D26h08r04	1.95	0.80	1.98	0.73	1.97	0.61
D26h08r08	1.66	0.80	1.70	0.72	1.71	0.65
D26h15r04	2.53	0.77	2.48	0.71	2.50	0.58
D26h15r08	2.19	0.75	2.07	0.67	2.15	0.52

Notes:
D16h08r04θ90 model: all ribs with the same inclination of 90°;
PV = 1.85 and PP = 0.5.

Fig. 80: Kt numerical result from (Nunes, 2014)

Among the presented results the worst situation is in the case with biggest height and lowest curvature radius, with a peak factor of 2.79. More in general the maximum values of this factor stand between 1.5 and 2.5, in relation to the different geometry situations, so commonly we can conclude that ribs usually double the stresses at the level of their connection to the bar.
These singularities are not significant to reduce bar strength and so this phenomenon doesn't affect bar's mechanical characteristics; so the presence of the hole in the “smart” bar reduce the full section increasing the stress, but the value are little bigger of the Kt value due to the ribs. However, will be needed to understand if this cavity could reduce the bar resistance e/o ductility and eventually find a solution about this problem, how for instance make a rib could be realised around the holed section in order to restore the total area of steel and avoid weaknesses

Chapter 4
4. Numerical study: fluid pressure inside the cavity

The aim of this part is to understand how the pressure change inside the fluid, due to a mechanical action, temperature and both mechanical and temperature together.

4.1 The low-cost sensor

The most common type of MEMS (Micro Electro-Mechanical Systems) is the barometric sensor which usually integrates pressure and temperature sensors. Thanks to their small dimension, this type of sensors are used in smartphones and smartwatches, IoT devices etc; one of the important point is that these sensor have a really low cost in the market around 2 $ (Tondolo, 2017).

Inside the cavity of the steel bar, we insert a MEMS sensor that is the LPS25H model that we use is an ultra-compact absolute piezoresistive pressure sensor. It includes a monolithic sensing element and an IC interface able to take the information from the sensing element and to provide a digital signal to the external world. The sensing element consists of a suspended membrane realized inside a single mono-silicon substrate. It can detect the absolute pressure and is manufactured using a dedicated process developed by ST. The membrane is very small compared to the traditionally built silicon micromachined membranes. Membrane breakage is prevented by an intrinsic mechanical stopper.

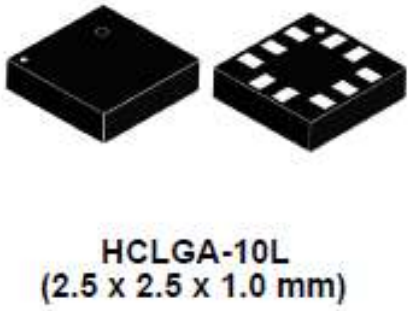

Fig. 81: LPS25H – MEMS pressure sensor

This sensor can measure the variation of pressure and temperature inside the fluid of the cavity. The most important features of this instrument about our job is the device sensibility, that is the smallest value of measure that the device can detect and the pressure range at which it works.

- $260\ to\ 1260\ hPa$ absolute pressure range;
- High-resolution mode: 1 Pa RMS;

4.2 Effect of mechanical action

In this part with ADINA program, we have built a F.E.M model to understand how the pressure variation changes inside the fluid in the cavity due to a mechanical action. All work thanks to the perfect gas law PV=nRT; when the bar is subject to any stress, the cavity deforms following the bar.

So, how we can see from the equation before, from the moment that the cavity is sealed, if occur an increase of cavity volume due to the tensile stress, the pressure goes down; instead if occur an decrease of cavity volume due to a compressive stress, the pressure goas up. So, the equation remains in equilibrium. The basic idea is to improve the sensibility of the barometric sensor, that mean to find a way to increase the pressure value inside the cavity. One solution is to put inside the cavity some incompressible fluid like oil, that has the bulk modulus much bigger than air. In this case the entire cavity deforms in the same way of before, but the air volume deform is much smaller than before and the pressure variation is much bigger than when in the cavity there is only air. With this idea we can raise the pressure variation inside the cavity.

4.2.1 F.E.M Model definition with ADINA Structures

In this part we have made a F.E.M model as close as possible to the reality, to understand better the behaviour of the smart bar. The F.E.M model is built totally with ADINA Structures and it is made a steel part that represents Ø20 steel bar with a cavity where inside there is a fluid part.

The cavity geometry is defined according to the real dimensions: in this F.E.M model, air cavity is represented by a quarter of cylinder with a diameter of 4 mm and a height of 15.5 mm. At the bottom there is a steel layer 1 mm thick, while at the top of the air cavity, another hole is modelled in order to represent the upper portion where the feed-through is placed: this is a quarter of cylinder with a diameter of 6 mm and an height of 3.5 mm (Battistoni, 2018).

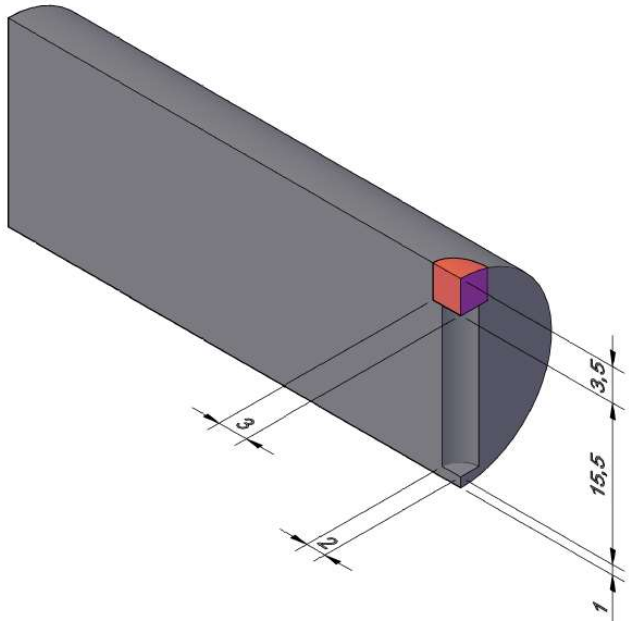

Fig. 82: A quarter of F20 Smart Steel Bar

The electrical feed-through is not modelled, because it doesn't give significant contribution in terms of stiffness. In this case, air volume in one-quarter-bar model is 48.69 mm^3, while air occupies 194.78 mm^3 in the entire cylindrical cavity (Battistoni, 2018).

For this analysis we have chosen a "plastic-multilinear" material (steel) that represent the real law obtained from the displacement control in the laboratory test in the previous campaign.

The "plastic-multilinear" material (steel) input data are:

- Young's Modulus: $E = 200000$ Mpa
- Poisson's ratio: $\nu = 0.3$
- Density: $d = 7.85 * 10^{-6}\ kg/mm^3$

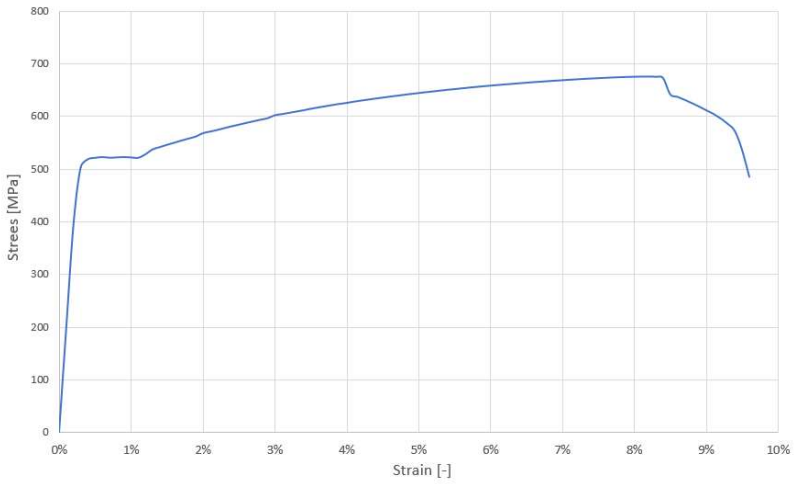

Fig. 83: The "plastic-multilinear" law obtained from the displacement control in the laboratory test

So, a "plastic-multilinear" material (steel) is inserted and Element Group is defined as a group of "3D solid" steel elements (Meshing→Elements Group). The elements are generated with an "automatic mesh" tool (Meshing→Mesh Density→Create Mesh), after defining the geometry of the model, that is a quarter of steel bar with a length of 50 cm and a diameter of 20 mm, cut for symmetry reasons by two planes (XY-YZ). The main different from the previous model (Battistoni, 2018) is that the mesh near the hole is denser to have a better resolution. The cavity stands at the middle of the bar, so at the edge of one-quarter-bar models.

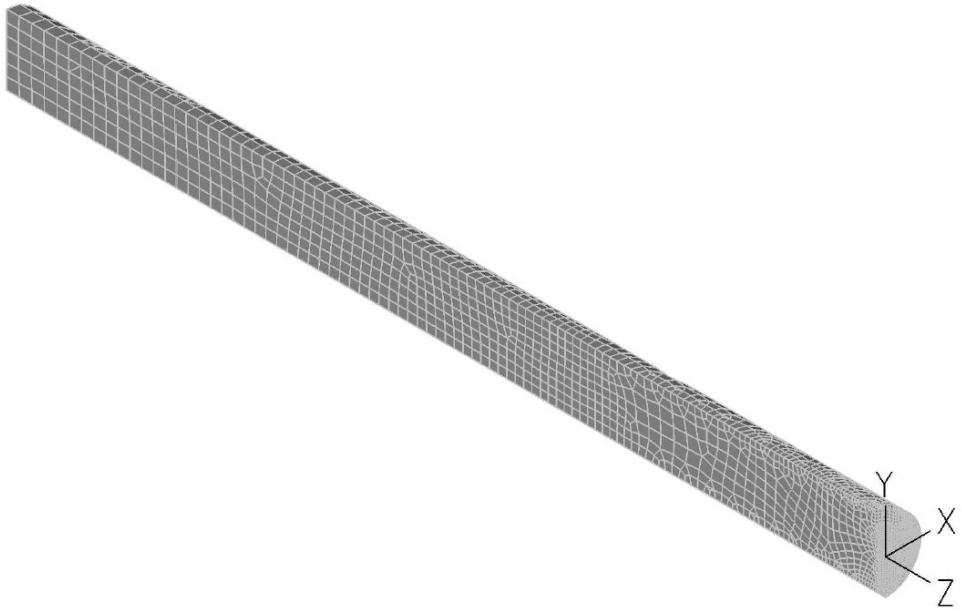

Fig. 84: One-quarter steel bar geometry

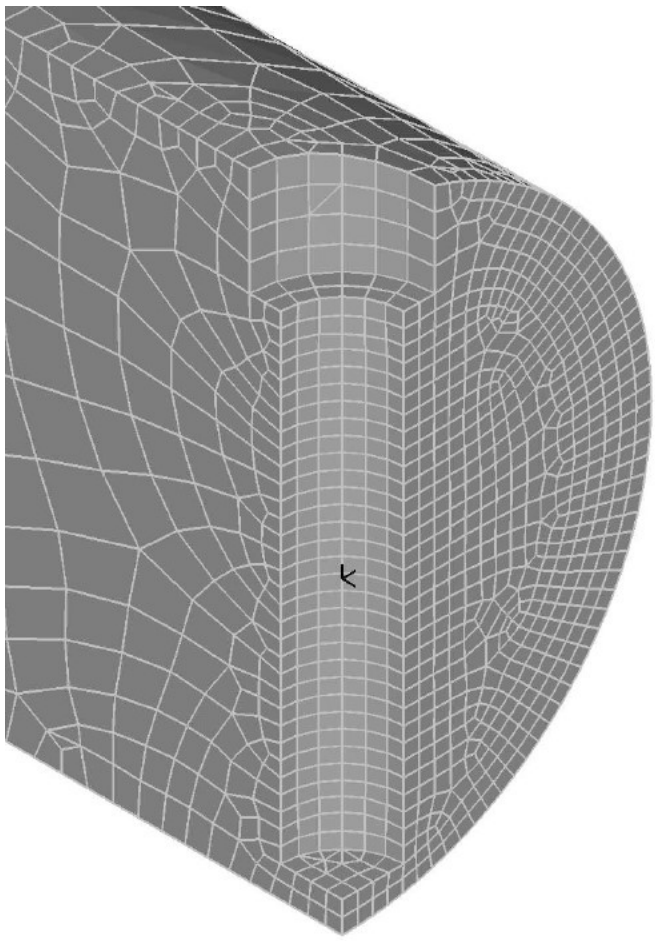

Fig. 85: One-quarter steel bar geometry - detail

The boundary conditions are defined by applying fixities on nodes: each one of the two faces generated by cutting the bar with planes have translation constrained along their respective orthogonal direction. Nodes lying on plane XY have translation along Z-axis fixed and nodes on plane YZ have translation fixed along X-axis (Model→Boundary conditions→Define fixity→Apply Fixity on interested body faces).

The fluid inside the cavity is air and it is defined with a “Potential-based Fluid” material with the following features:

- Bulk modulus: 0.142 MPa;
- Density: $1.2 * 10^{-9}\,\mathrm{kg/mm^3}$;

Element Group is defined as group of "3D fluid" elements and then elements composing the fluid model are generated, a quarter of air cylinder with a height of 15.5 mm and a diameter of 4 mm, cut for symmetry reasons by two planes as done before. This fluid cylinder fits in the lower cavity left by the steel bar model and the two elements group share the nodes located along the interfaces between them (Battistoni, 2018); to share the nodes with the steel part, the element of the fluid group are built manually, before inserting the nodes (Meshing→Nodes→Define→Import) and after defining the elements with the relative nodes (Meshing→Elements Nodes→Import); the other two vertical faces are automatically restrained by boundary conditions alike the ones applied on neighbour faces, while the top face is closed by a thin cap, realised of "3D solid" elements and made with an “Elastic isotropic” material with low stiffness (3000 Pa). This thin cap was built manually, doing share the nodes with the steel part and the fluid part. It is used to simulate the closing contribution given by the feed-through element, but without giving additional stiffness to the drilled portion (Battistoni, 2018). How with the steel part, the boundary condition has been applied on the interest nodes of the thin cap; nodes lying on plane XY have translation along Z-axis fixed and nodes on plane YZ have translation fixed along X-axis (Model→Boundary conditions→Apply on Nodes).

How we can see in the following chapter, we need to simulate the incompressible fluid like oil inside the cavity. To do this, we define a new “3D Fluid” element group with a “Potential-based Fluid” material with a bulk modulus much bigger than air (2200 MPa) to simulate it. So, we replace the air element with the incompressible fluid elements.

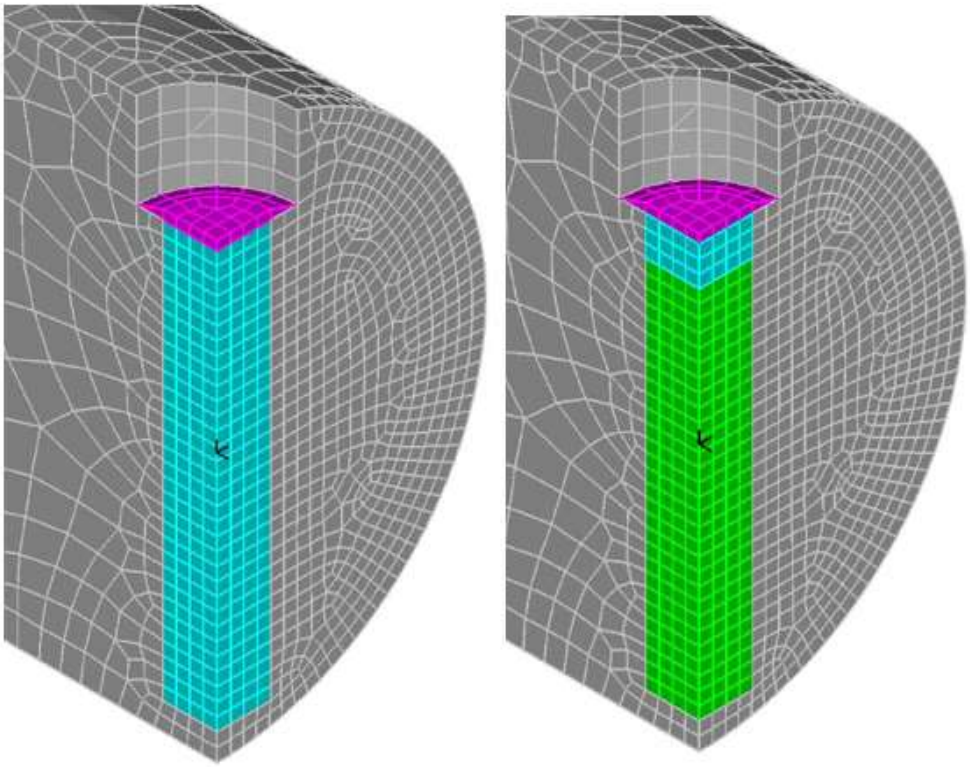

Figure 86: One-quarter steel bar geometry with air and oil – detail

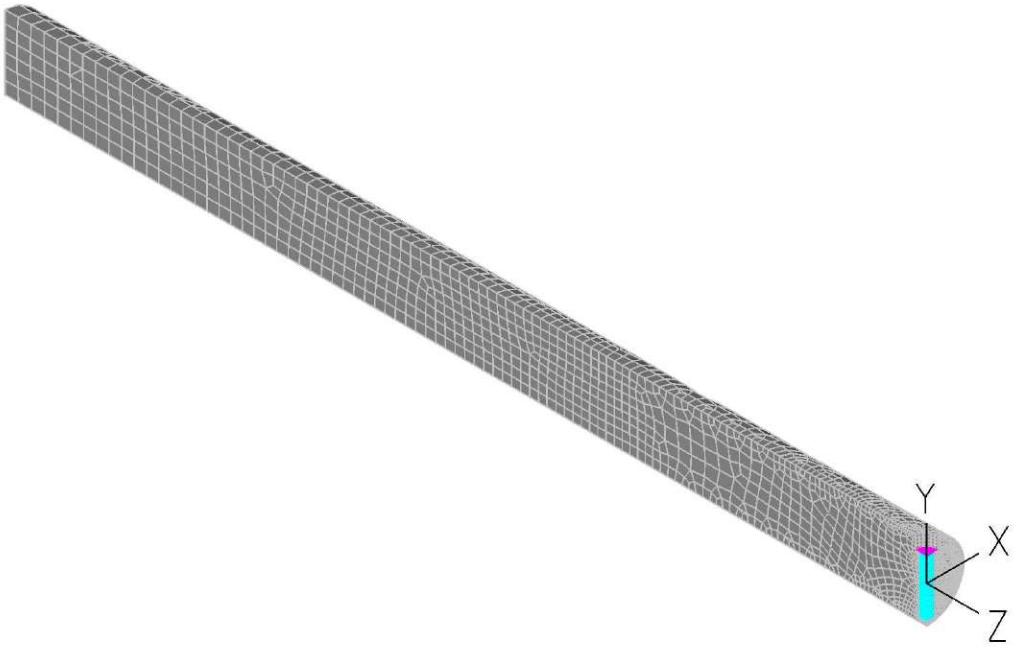

Fig. 87: One-quarter steel bar – complete model with air

4.2.2 Pressure in the fluid: elastic field

How we can see from the features of the MEMS, the minimum pressure variation that this device can feel is 1 Pa.

This is very important, because to have a good sensibility in the field of civil engineering, regard the structural monitoring, we need to detect 1 με of strain on the "smart" bar under study. For this, the device must capture the pressure variation of 1 Pa each time the bar feels 1 με of strain. In other words, the variation of 1 Pa in the air must be at least equivalent to the variation of 1 με on the bar.

The solution to reach the goal, is to fill the cavity that host the MEMS with an incompressible fluid, such as oil that has a bulk modulus much bigger than air.

So, we must understand how much oil we can put inside the cavity to have a resolution of $1\ \text{Pa} = 1\ \mu\varepsilon$.

First, we need to understand the variation of the air pressure inside the cavity for each με on the steel bar, when in the cavity there is only air. We have applied on the edge of the bar a displacement of 0.0125 mm in 50 different steps, with the aim that for each steps the increment of strain on the bar is precisely 1 με. In the follows table we can see the displacement applied on the edge in each step and the correspondence strain and stress.

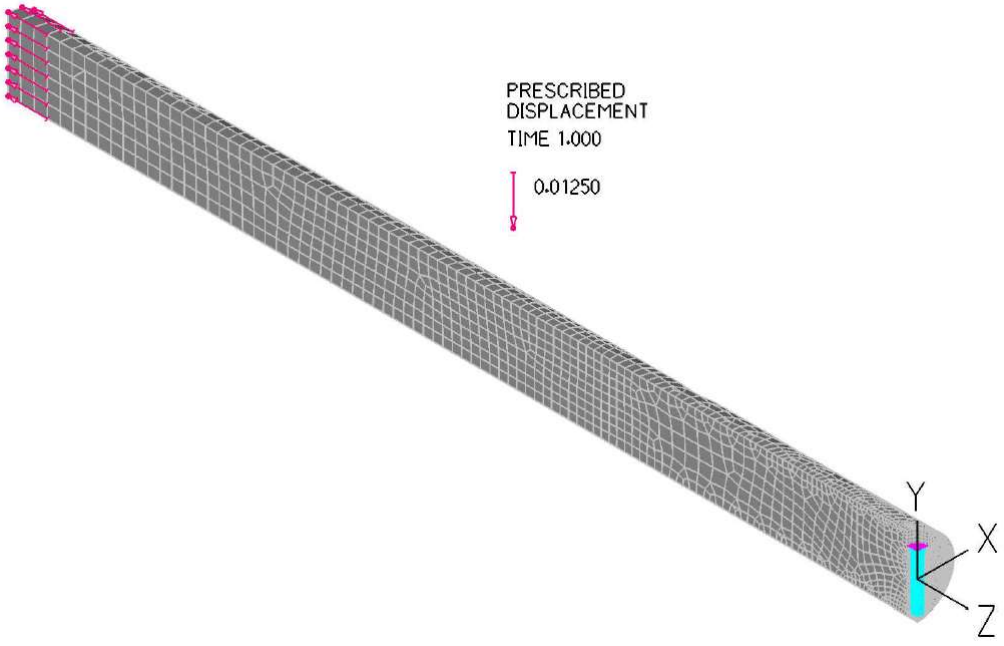

Fig. 88: One-quarter steel bar (complete model) - applied displacement

With this very small displacement the steel bar is in the elastic field and the pressure variation from one step to the follow, is linear. We have applied a tensile stress on the steel bar, so according with perfect gas law (PV=nRT) the volume of the cavity became little bigger and the pressure goes down. To simplify, in the following table we consider the absolute value of pressure variation.

		Result obtained from FEM model		
Time steps	Displ. applied on the edge [mm]	με [-]	$\sigma_{\text{full section}}$ [MPa]	Absolute value of pressure variation [Pa]
0	0.00000	0	0.0	0.000
1	0.00025	1	0.2	0.225
2	0.0005	2	0.4	0.449
3	0.00075	3	0.6	0.674
4	0.001	4	0.8	0.899
5	0.00125	5	1.0	1.123
6	0.0015	6	1.2	1.348
7	0.00175	7	1.4	1.573
8	0.002	8	1.6	1.797
9	0.00225	9	1.8	2.022
10	0.0025	10	2.0	2.247
11	0.00275	11	2.2	2.471
12	0.003	12	2.4	2.696
13	0.00325	13	2.6	2.921
14	0.0035	14	2.8	3.145
15	0.00375	15	3.0	3.370
16	0.004	16	3.2	3.595
17	0.00425	17	3.4	3.819
18	0.0045	18	3.6	4.044
19	0.00475	19	3.8	4.269
20	0.005	20	4.0	4.493
21	0.00525	21	4.2	4.718
22	0.0055	22	4.4	4.943
23	0.00575	23	4.6	5.167
24	0.006	24	4.8	5.392
25	0.00625	25	5.0	5.617
26	0.0065	26	5.2	5.841
27	0.00675	27	5.4	6.066
28	0.007	28	5.6	6.291
29	0.00725	29	5.8	6.515
30	0.0075	30	6.0	6.740
31	0.00775	31	6.2	6.965
32	0.008	32	6.4	7.190
33	0.00825	33	6.6	7.414
34	0.0085	34	6.8	7.639
35	0.00875	35	7.0	7.864
36	0.009	36	7.2	8.088
37	0.00925	37	7.4	8.313
38	0.0095	38	7.6	8.538
39	0.00975	39	7.8	8.762
40	0.01	40	8.0	8.987
41	0.01025	41	8.2	9.212

42	0.0105	42	8.4	9.436
43	0.01075	43	8.6	9.661
44	0.011	44	8.8	9.886
45	0.01125	45	9.0	10.111
46	0.0115	46	9.2	10.335
47	0.01175	47	9.4	10.560
48	0.012	48	9.6	10.785
49	0.01225	49	9.8	11.009
50	0.0125	50	10.0	11.234

How we can see from the solution of FEM model, the pressure variation from one step to another is $|0.225|$ Pa. With a simple proportion we can understand how much percentage of air and oil we must have in the cavity, to achieve the required sensibility.

$$\frac{V_{tot} = 100}{V_{air} = ?} * 0.225 \text{ Pa} = \text{n Pa} \quad \rightarrow \quad V_{air} = \frac{100 * 0.225}{\text{n Pa}} \quad \rightarrow \quad V_{oil} = 100 - V_{air}$$

Theory consideration		
Level of sensibility	**Volume of Air [%]**	**Volume of Oil [%]**
$1\ \mu\varepsilon = 1$ Pa	22.50	77.50
$1\ \mu\varepsilon = 2$ Pa	11.25	88.75

How we can see in the previous table, if we want to reach the sensibility of $1\ \mu\varepsilon = 1$ Pa, we must fill the cavity with 77.50% of oil. If we want double sensibility, we need 88.75% of oil in the cavity.

In the following table is reported the value of pressure obtained with the FEM analisys when the cavity is empty and the relative theoretical pressure variation if we fill the cavity with the incompressible fluid.

	Absolute Value of air pressure obtained from FEM model	**Absolute Value of air pressure obtained from theory consideration**	
με [-]	**Olio 0% Aria 100% [Pa]**	**Olio 77.50% Aria 22.50% [Pa]**	**Olio 88.75% Aria 11.25% [Pa]**
0	0.000	0	0
1	0.225	1	2
2	0.449	2	4
3	0.674	3	6
4	0.899	4	8
5	1.123	5	10
6	1.348	6	12

7	1.573	7	14
8	1.797	8	16
9	2.022	9	18
10	2.247	10	20
11	2.471	11	22
12	2.696	12	24
13	2.921	13	26
14	3.145	14	28
15	3.370	15	30
16	3.595	16	32
17	3.819	17	34
18	4.044	18	36
19	4.269	19	38
20	4.493	20	40
21	4.718	21	42
22	4.943	22	44
23	5.167	23	46
24	5.392	24	48
25	5.617	25	50
26	5.841	26	52
27	6.066	27	54
28	6.291	28	56
29	6.515	29	58
30	6.740	30	60
31	6.965	31	62
32	7.190	32	64
33	7.414	33	66
34	7.639	34	68
35	7.864	35	70
36	8.088	36	72
37	8.313	37	74
38	8.538	38	76
39	8.762	39	78
40	8.987	40	80
41	9.212	41	82
42	9.436	42	84
43	9.661	43	86
44	9.886	44	88
45	10.111	45	90
46	10.335	46	92
47	10.560	47	94
48	10.785	48	96
49	11.009	49	98
50	11.234	50	100

If we want to see the problem from the stress, we can notice that with the incompressible fluid in the cavity, for each MPa on the bar, our device fells a pressure variation of 5.03 Pa with 77.50% of oil or 10.06 Pa with 88.75% of oil.

Theory consideration		
Variation of pressure for each MPa on the steel bar	**Olio 77.50% Aria 22.50%**	**Olio 88.75% Aria 11.25%**
$\frac{\text{Press. Aria [Pa]}}{\sigma\_el\_teorico[MPa]}$	5.03	10.06

To control the feasibility of the theory model and to understand which is the best percentage of oil with the model that we have built, we have made three differents attemps. The choice of the following percentage of oil depends on the mesh built and it must be bigger than the percentage of 88.75% from theory consideration, to have at least a sensibility of 1 με = 2 Pa. The value of the F.E.M model will confront with the theroy consideration.

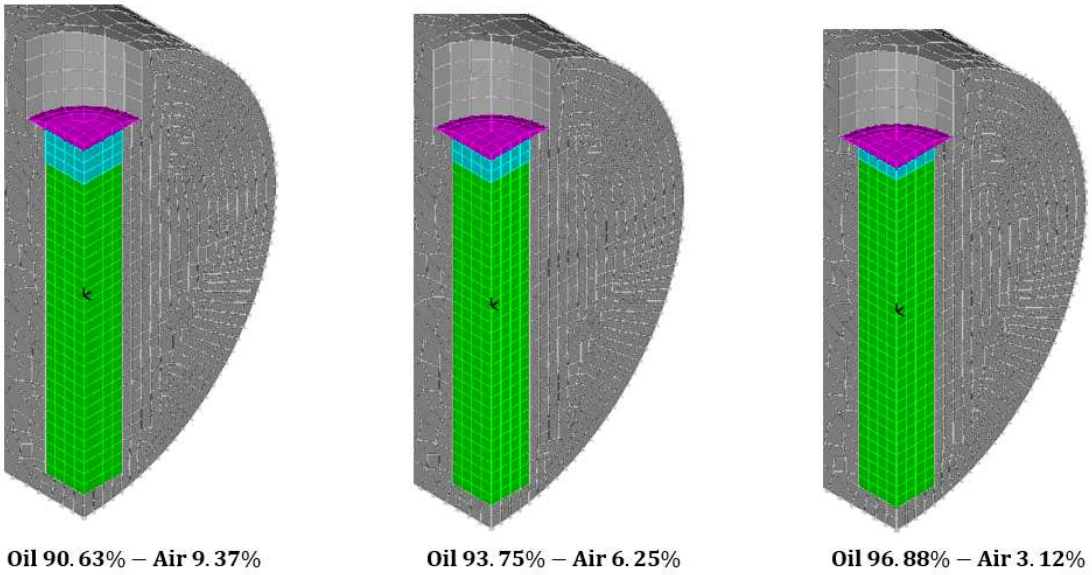

Fig. 89: Cavity filled with incompressible fluid

In the folowing table we can see the probably level of sensibility that we obtained with the proportion formulation of theroy consideration.

Percentage of Oil and Air in our FEM model		Result obtained from theory consideration using the proportion formulation	
Volume of Air [%]	**Volume of Oil [%]**	**Theory variation of pressure each step** $\frac{100 * 0.225}{V_{air}} = n$ **Pa**	**Theory Level of sensibility**
9.37	90.63	2.40	1 με = |2.40 |Pa
6.25	93.75	3.60	1 με = |3.60| Pa
3.12	96.88	7.21	1 με = |7.21 |Pa

Is possible to do this reasoning, for each percentage of incompressible fluid inside the cavity. With the following picture is possible to understand the benefit of the oil inside the cavity. We can notice that increase the percentage of the oil, the value of the pressure inside the cavity rise not proportionally and became very high when the cavity is almost fill.

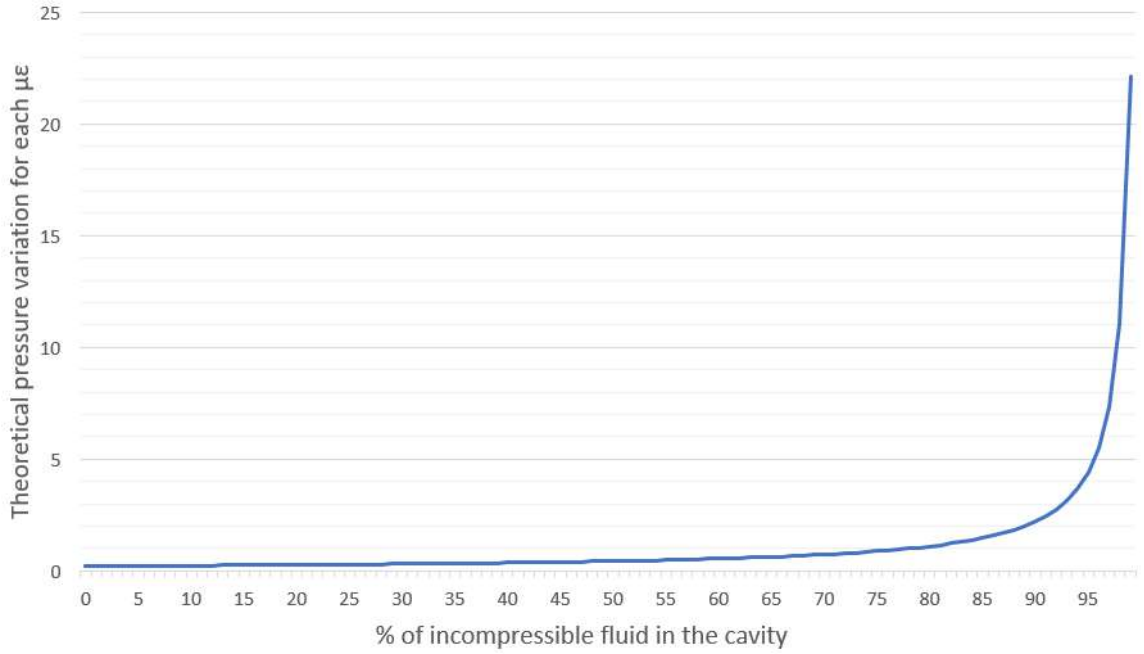

Fig. 90: Trend of increase sensibility with oil inside the cavity

In the next table there are the result obtained from the FEM model. How we can see, the value of pressure variation from the FEM model is in according with the theory consideration:

- Oil 90.63%: |2.39| Pa instead of |2.40| Pa;
- Oil 93.75%: |3.56| Pa instead |3.60| Pa;
- Oil 96.88 %: |7.08| Pa instead |7.21| Pa;

	Absolute Value of Air pressure obtained from the FEM model		
με [-]	**Oil 90.63% Air 9.37 % [Pa]**	**Oil 93.75% Air 6.25 % [Pa]**	**Oil 96.88% Air 3.12 % [Pa]**
0	0.00	0.00	0.00
1	2.39	3.56	7.08
2	4.79	7.12	14.16
3	7.18	10.69	21.24
4	9.57	14.25	28.32
5	11.97	17.81	35.40
6	14.36	21.37	42.49
7	16.75	24.93	49.57
8	19.15	28.49	56.65
9	21.54	32.06	63.73
10	23.93	35.62	70.81
11	26.33	39.18	77.89
12	28.72	42.74	84.97
13	31.11	46.30	92.05
14	33.51	49.87	99.13
15	35.90	53.43	106.22
16	38.29	56.99	113.30
17	40.69	60.55	120.38
18	43.08	64.11	127.46
19	45.47	67.68	134.54
20	47.87	71.24	141.62
21	50.26	74.80	148.70
22	52.65	78.36	155.79
23	55.05	81.92	162.87
24	57.44	85.49	169.95
25	59.83	89.05	177.03
26	62.23	92.61	184.11
27	64.62	96.17	191.19
28	67.01	99.73	198.27
29	69.41	103.30	205.36
30	71.80	106.86	212.44
31	74.19	110.42	219.52
32	76.59	113.98	226.60
33	78.98	117.55	233.68
34	81.37	121.11	240.76
35	83.77	124.67	247.85
36	86.16	128.23	254.93
37	88.55	131.79	262.01
38	90.95	135.36	269.09
39	93.34	138.92	276.17
40	95.73	142.48	283.26
41	98.13	146.04	290.34

42	100.52	149.61	297.42
43	102.91	153.17	304.50
44	105.31	156.73	311.58
45	107.70	160.29	318.67
46	110.09	163.86	325.75
47	112.49	167.42	332.83
48	114.88	170.98	339.91
49	117.27	174.54	347.00
50	119.67	178.11	354.08

The pressure increase is linear in each case, because we are in the elastic field; in the following picture we can see the trend of the pressure for the theory model and the numerical model, for different percentage of oil.

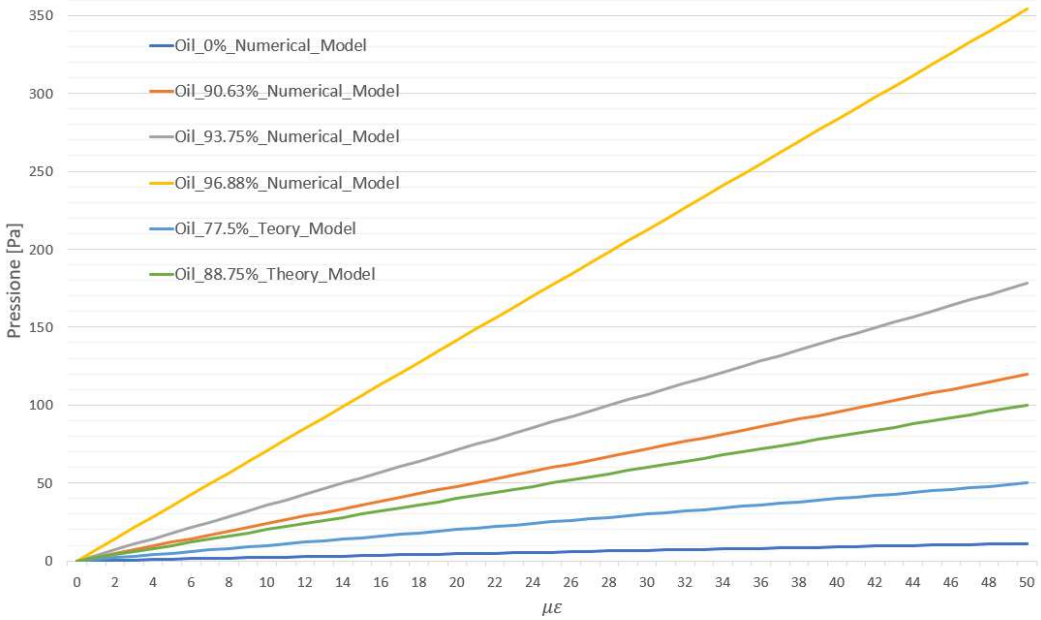

Fig. 91: Pressure variation with different percentage of oil in the cavity

The following table describes how much the pressure became bigger when in the cavity there is some incompressible fluid. The maximum rise of pressure obtained from the F.E.M model, is when the percentage of oil is 96.88% and it is 32.05 time than the situation of empty cavity.

Value of pressure increase from the situation with the cavity without oil				
	Oli 0% Air 100%	**Oil 90.63% Air 9.37 %**	**Oil 93.75% Air 6.25 %**	**Oil 96.88% Air 3.12 %**
$\frac{V\_tot}{V\_air}$	$\frac{100}{100} = 1$	$\frac{100}{9.37} = 10.67$	$\frac{100}{6.25} = 16$	$\frac{100}{3.12} = 32.05$

So, for each MPa on the steel bar, the pressure increase is very high and depend of the percentage of oil inside the cavity.

Result obtained from the FEM model				
Increase the pressure for each increase stress on the steel bar	**Olio 0% Aria 100%**	**Oil 90.63% Air 9.37 %**	**Oil 93.75% Air 6.25 %**	**Oil 96.88% Air 3.12 %**
$\frac{\text{Press. Aria [Pa]}}{\sigma\_el\_teorico[MPa]}$	1.13	12.06	17.94	35.67

4.2.3 Pressure in the fluid: plastic field

In this part we want to understand what happen to a steel bar, when it is subject to a bigger stress. This because, how we have explained in the chapter 3, near the hole the stress intensity factor can rise the value of the stress that could occur the first plasticization.

To understand what happened in the full section and in the section with the hole, we have considered the same F.E.M model described before and we have applied on the edge a displacement of 0.75 mm. The stress in the full section should be:

$$\sigma = \varepsilon \cdot E = \frac{\Delta L}{L} \cdot E = \frac{0.75\ mm}{250\ mm} \cdot 200000\ MPa = 600\ MPa$$

In the following table we can see the result of 50 steps from the F.E.M model. We can notice that when the full section is in the elastic field at level of 1191 με, that correspond to 228 MPa, in the section with the hole occur the first plasticization. After, when the full bar begins the plasticization, the section with the hole have reached a level of 18532 με.

	Result obtained from FEM model with "plastic-multilinear" material					
	Stress and strain in the generic element of the full section			Stress and strain in the element near the hole		
Steps [-]	**Accum. eff. plastic. strain [-]**	**με [-]**	**σ [MPa]**	**Accum. eff. plastic. strain [-]**	**με [-]**	**σ [MPa]**
0	0.0%	0	0	0.0%	0	0
1	0.0%	66	13	0.0%	170	33
2	0.0%	132	25	0.0%	339	66
3	0.0%	198	38	0.0%	509	99
4	0.0%	264	51	0.0%	678	131
5	0.0%	329	63	0.0%	848	164
6	0.0%	395	76	0.0%	1018	197
7	0.0%	461	89	0.0%	1189	229
8	0.0%	527	101	0.0%	1360	262
9	0.0%	593	114	0.0%	1531	294
10	0.0%	659	127	0.0%	1703	326

11	0.0%	725	139	0.0%	1877	358
12	0.0%	791	152	0.0%	2071	385
13	0.0%	857	165	0.0%	2266	413
14	0.0%	924	177	0.0%	2472	437
15	0.0%	990	190	0.0%	2684	459
16	0.0%	1057	203	0.0%	2917	476
17	0.0%	1125	215	0.0%	3179	491
18	0.0%	1191	228	0.1%	3443	505
19	0.0%	1258	240	0.1%	3740	510
20	0.0%	1326	253	0.1%	4060	513
21	0.0%	1394	265	0.2%	4392	515
22	0.0%	1463	278	0.2%	4755	517
23	0.0%	1534	291	0.2%	5152	518
24	0.0%	1610	305	0.3%	5575	519
25	0.0%	1689	320	0.3%	6041	519
26	0.0%	1771	335	0.4%	6550	519
27	0.0%	1855	351	0.5%	7118	519
28	0.0%	1938	367	0.5%	7765	519
29	0.0%	2017	382	0.6%	8500	519
30	0.0%	2106	397	0.7%	9379	519
31	0.0%	2249	412	0.8%	10413	521
32	0.0%	2422	430	0.9%	11616	526
33	0.0%	2617	451	1.1%	13073	533
34	0.0%	2817	472	1.2%	14837	543
35	0.0%	2976	490	1.4%	16592	551
36	0.1%	3142	505	1.6%	18532	559
37	0.1%	3448	509	1.9%	20932	569
38	0.1%	3838	515	2.2%	23920	579
39	0.2%	4321	520	2.5%	27464	592
40	0.2%	4915	521	2.9%	31495	603
41	0.3%	5583	523	3.4%	35843	615
42	0.4%	6286	523	3.8%	40342	625
43	0.4%	7015	522	4.3%	44908	634
44	0.5%	7775	523	4.8%	49487	641
45	0.6%	8559	523	5.2%	54046	648
46	0.7%	9367	523	5.7%	58588	654
47	0.7%	10202	523	6.2%	63075	659
48	0.8%	11077	522	6.6%	67561	663
49	0.9%	11958	527	7.1%	72154	662
50	1.0%	12836	535	7.6%	77122	646

The following picture represent the bheavior of the section with the hole and the generic full section; both in the following picture and in the table above, we have indicate with orange color the moment when occur the plasticization of the section with the hole and with the green color when occur the plasticization of the full section.

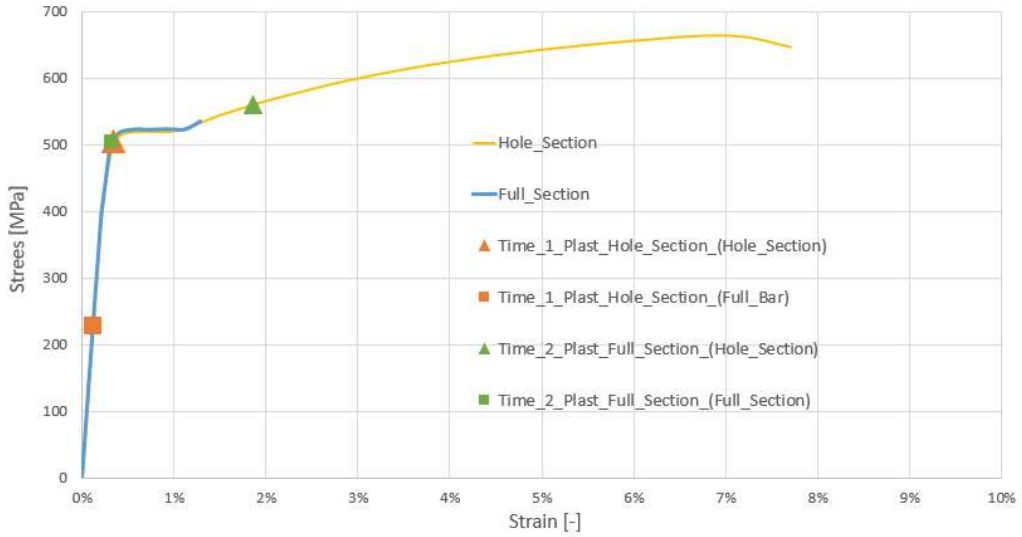

Fig. 92: Stress-Strain Graph of element of the F.E.M model

How we can see from the following graph, the pressure variation is very big, due to a plasticization, because the variation of cavity volume is much bigger than in the elastic field; the behaviour from linear became nonlinear when the deformation of the cavity increases after the plasticization.

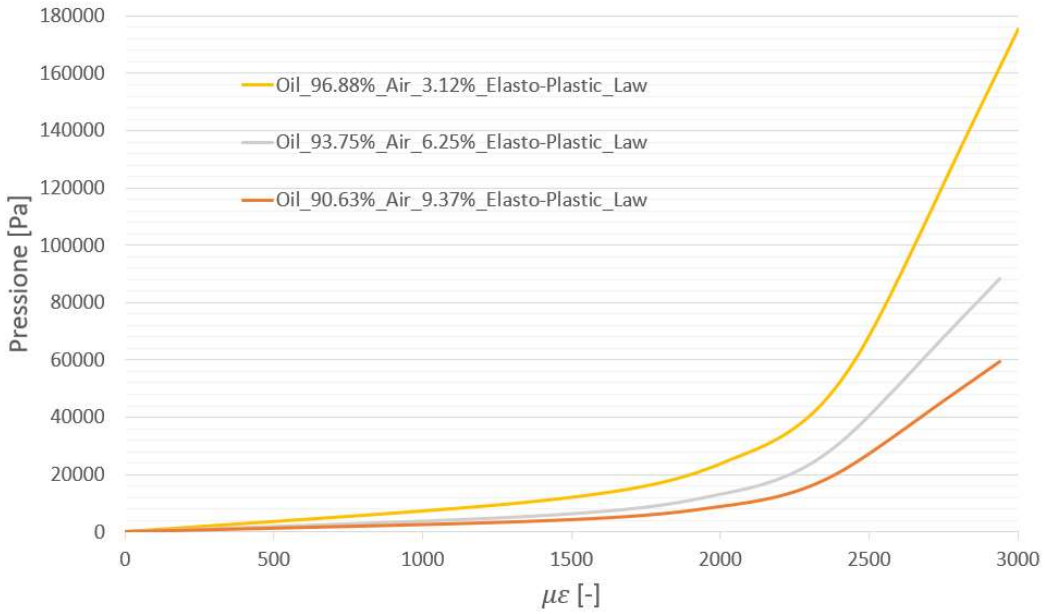

Fig. 93: Trend of Pressure variation at the beginning of the plastic field

So, we need to control that the pressure variation is inside the MEMS pressure range. For the tensile stress we consider the maximum value of pressure with this displacement applied, namely when the steel bar has reached a strain of 7.7%; for compression stress we considered the pressure value at level of 0.5 % of strain, namely when the concrete breaks.

Is possible to notice that the only value of pressure that remain inside the range of the MEMS device, is the situation with 90.63 % of incompressible fluid inside the cavity.

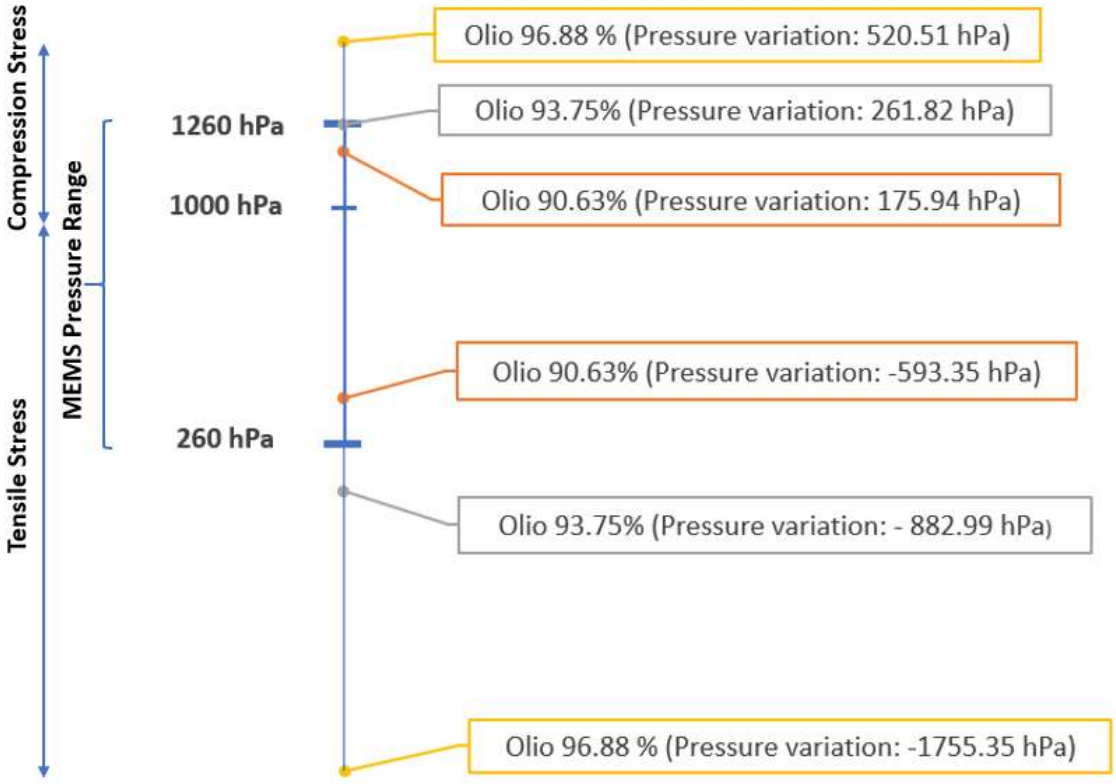

Fig. 94: MEMS Range of pressure with pressure variation

Take into account the F.E.M model with 90.63% of oil in the cavity, that is the only one which stay inside the MEMS pressure range, to understand better the behaviour of the pressure inside the cavity, we have done a comparison from two different law:

- "Isotropic linear elastic" material;
- A "plastic-multilinear" material;

The behaviour of the pressure in first case is always linear, instead the behaviour of the second case is linear until one grade of strain, and after becoming non-linear cause of the first plasticization around the hole.

Calculating the angular coefficient doing:

$$\text{Angle coefficient} = \frac{\text{pressure step}(\,i+1) - \text{pressure step}\,(i)}{\Delta\mu\varepsilon}$$

If we do the different between the angle coefficient obtained from the result of “plastic multilinear” material and “isotropic linear elastic” material, we can notice the point where the pressure behaviour became non-linear; so, this point is when occur the first plasticization near the hole.

	Result obtained from FEM model with “plastic-multilinear" material		Result obtained from FEM model with "Isotropic linear elastic" material		
Steps [-]	**Oil 90.63% Air 9.37 % [Pa]**	**Angle coefficient [-]**	**Oil 90.63% Air 9.37 % [Pa]**	**Angle coefficient [-]**	**Difference of Angle coefficient [-]**
0	0	-	0	-	-
1	143.62	2.4	143.30	2.4	0.0
2	287.28	2.4	286.59	2.4	0.0
3	430.97	2.4	429.89	2.4	0.0
4	574.71	2.4	573.19	2.4	0.0
5	718.48	2.4	716.48	2.4	0.0
6	862.28	2.4	859.78	2.4	0.0
7	1006.20	2.4	1003.07	2.4	0.0
8	1150.40	2.4	1146.37	2.4	0.0
9	1294.93	2.4	1289.66	2.4	0.0
10	1439.76	2.4	1432.96	2.4	0.0
11	1584.91	2.4	1576.25	2.4	0.0
12	1730.59	2.4	1719.54	2.4	0.0
13	1877.51	2.4	1862.83	2.4	0.0
14	2026.82	2.5	2006.11	2.4	0.1
15	2179.51	2.5	2149.40	2.4	0.2
16	2335.66	2.6	2292.68	2.4	0.2
17	2495.66	2.7	2435.96	2.4	0.3
18	2657.77	2.7	2579.24	2.4	0.3
19	2824.33	2.8	2722.52	2.4	0.4
20	2997.32	2.9	2865.79	2.4	0.5
21	3179.57	3.0	3009.06	2.4	0.6
22	3372.71	3.2	3152.33	2.4	0.8
23	3580.55	3.5	3295.59	2.4	1.1
24	3806.85	3.8	3438.86	2.4	1.4
25	4052.52	4.1	3582.11	2.4	1.7
26	4320.38	4.5	3725.37	2.4	2.1
27	4616.46	4.9	3868.62	2.4	2.5
28	4949.43	5.5	4011.87	2.4	3.2
29	5329.86	6.3	4155.12	2.4	4.0
30	5775.97	7.4	4298.36	2.4	5.0
31	6314.44	9.0	4441.60	2.4	6.6
32	6956.32	10.7	4584.83	2.4	8.3
33	7727.83	12.9	4728.07	2.4	10.5
34	8600.83	14.6	4871.29	2.4	12.2
35	9427.55	13.8	5014.52	2.4	11.4
36	10368.80	15.7	5157.73	2.4	13.3
37	11549.60	19.7	5300.95	2.4	17.3
38	13069.90	25.3	5444.16	2.4	23.0

39	15054.90	33.1	5587.37	2.4	30.7
40	17593.80	42.3	5730.57	2.4	39.9
41	20735.20	52.4	5873.77	2.4	50.0
42	24470.40	62.3	6016.96	2.4	59.9
43	28612.60	69.0	6160.15	2.4	66.7
44	32947.70	72.3	6303.33	2.4	69.9
45	37375.30	73.8	6446.51	2.4	71.4
46	41865.50	74.8	6589.68	2.4	72.5
47	46298.80	73.9	6732.85	2.4	71.5
48	50657.10	72.6	6876.02	2.4	70.3
49	54982.20	72.1	7019.18	2.4	69.7
50	59334.90	72.5	7162.33	2.4	70.2

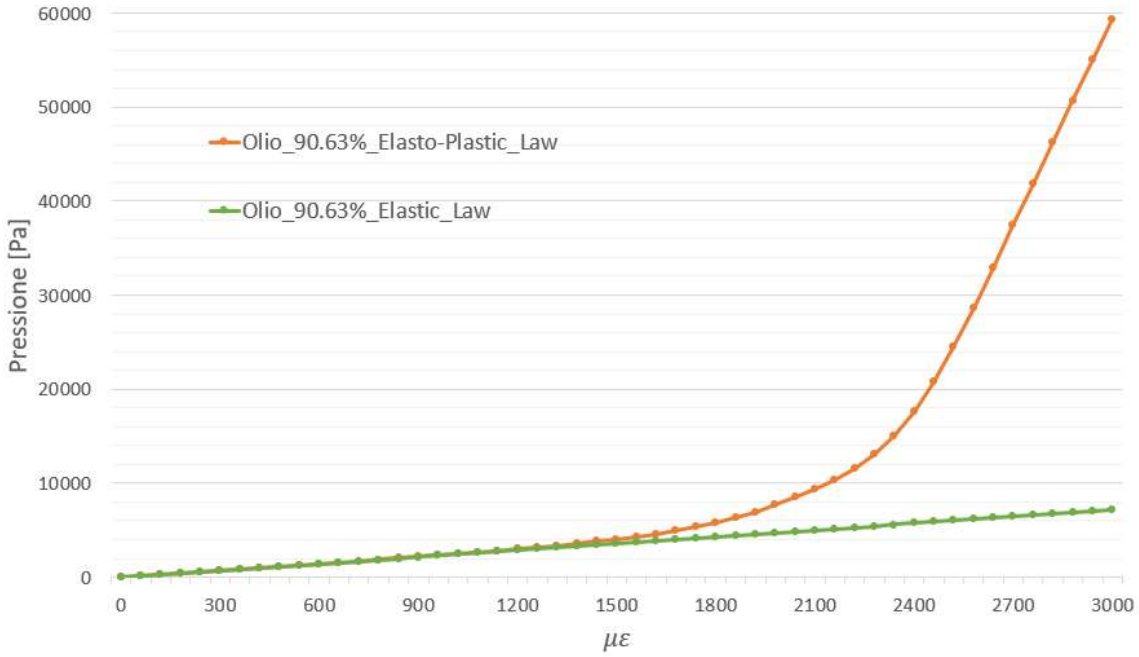

Fig. 95: Compare pressure trend with elastic and plastic law

4.3 Effect of temperature

Until this point, we only speak about mechanical action. These loads, from the point of the make stress inside the structure are the most important, because are loads that can able to damage it during his lifetime. Of course, together with this load there is also the environment effect like the temperature effect, that change the stress inside the structure. This temperature effect could be relevant or not but is needed to understand what happen to the structure when the daily temperature change.

In our case, with the "smart" steel bar, thanks to MEMS can catch the temperature and pressure variation, is needed to understand the pressure change due temperature variation, because in this way will be able to separate the temperature effect from the mechanical action effect on the structure. We want to sensitize the "smart" bar only with the mechanical action effect and purify it from temperature effect.

4.3.1 FEM model definition with ADINA FSI

In the previous chapter, we have described the “smart” steel F.E.M model. This model is built with only ADINA Structures, where the fluid part is made with a “potential-based fluid”; from the point of pressure the model works properly, but only if we apply the pressure or displacement loads; instead, when we apply a temperature load the fluid part doesn’t catch the variation of pressure due of the temperature effect.

For this, is needed to do a combine analysis with ADINA FSI (Fluid-Structure Interface). So, the built model is the same that we have described in the chapter 3.2, but the steel part is built in ADINA Structures and the fluid part is built in ADINA CFD (Computational Fluid Dynamic). This combined analysis is the only way to understand how the pressure change in the fluid due to temperature effect.

4.3.1.1 Steel bar definition in ADINA Structures

How we have explained in the chapters before, a "plastic-multilinear" material (steel) is inserted and Element Group is defined as a group of "3D solid" steel elements. The elements are generated with an "automatic mesh" tool, after defining the geometry of the model, that is a quarter of steel bar with a length of 50 cm and a diameter of 20 mm, cut for symmetry reasons by two planes (XY-YZ). The cavity stands at the middle of the bar, so at the edge of one-quarter-bar models (Battistoni, 2018).

We will do a transient analysis, so is needed to set ADINA Structure from Static to Dynamic-Implicit with CFD. With the implicit Transient Dynamics, we have chosen the default integration method (Bathe) deselecting the use of Automatic time stepping.

Doing a temperature analysis, in the ADINA Structure is needed define the initial condition of temperature. Assuming to be in standard condition, we have defined the initial temperature of 273 K (Model→Initial Conditions→Define→Apply).

With this FSI analysis, is needed to define the fluid-structure interface, namely the parts of the structure that are in contact with the fluid. Only the parts arounds the cavity and the bottom part of the feed-through are in contact with the fluid. So, the FSI boundary are imposed on this part.

Here we need to pay attention to the number of FSI boundary; because the numbers of the FSI boundary must be the same number of the FSI boundary in the fluid model to have a consistent solution. Indeed, how is explained in the follow chapter, we have only one FSI boundary in the fluid model, so is needed to have only one FSI boundary also in the structure model. Because the solid part in contact with the fluid is the steel inside the cavity and the bottom part of the feed-through, is needed to join the face-element to make the only one FSI boundary. To do this, we have defined the “Element Face Set” where is possible to insert the face element, both of steel part and feed-through part, making one face where applying the FSI boundary (Model→Boundary Conditions→FSI Boundary→Apply to Element Face Set). Of course, the other boundary condition is the same of the model described in the chapter 3.2.

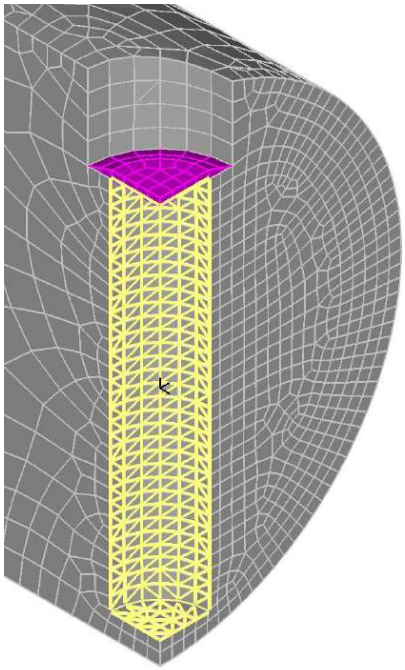

Fig. 96: One-quarter steel bar (EG1) geometry with FSI boundary - detail

4.3.1.2 Fluid cavity definition with ADINA CFD

In ADINA CFD, we have built the air cavity in the same way of the chapter 4.2.1, namely inserting manually the nodes and the elements.

So, the "3D Fluid" group are created setting the flow type inside the group as "Low-Speed Compressible" and the air material as "Laminar Material" with the follow features was assigned:

- Viscosity: 2e-5 N-s/m^2
- Density: 1.2 Kg/m^3
- Bulk Modulus: 142000 Pa
- Coef. Of Volume Expansion: 0.0036 °C^-1
- Thermal Conductivity: 0.025 W/m-°C
- Specific Heat at Constant Pressure: 1006 J/Kg-°C
- Specific Heat at Constant Volume: 700 J/Kg-°C

We have done a transient analysis; so, is important to change the default "Steady-State" to "Transient"; is also needed to change from "CFD Only" to "with Structures" from the moment that we will do an FSI analysis. To apply the perfect gas law, we must specify the flow assumption to use. The program gave us some solution, but to work properly is needed to set the flow model as "Laminar" and the flow type as "Low Speed Compressible", with "no thermal coupling" (Model→Flow Assumption→Specify Flow Assumption). With this flow type is required to define the initial conditions of the fluid model.

So, assuming to be in standard condition we have set the initial condition as follow:

- Initial temperature: 273 K;
- Initial Pressure: 100000 Pa;

For this analysis we can choice between two elements: FCBI and FCBI-C.

- The FCBI is able to use in 3D elements and all the variables are defined at corner nodes. If we use these elements in the window of the Specify flow assumption, we need to set the temperature equation to heat transfer. To give the initial condition on these elements, is needed apply these on the corner of the elements, so each node must have the initial condition (Model→Initial Conditions→Apply on Nodes).

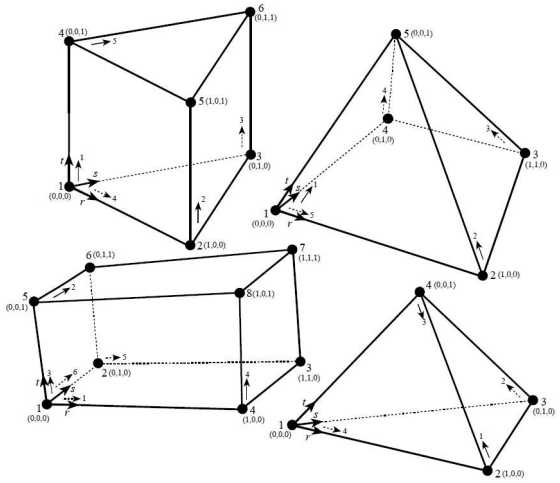

Fig. 97: FCBI elements

- The FCBI-C is able to use in 3D elements and all degrees of freedom are defined at centre of elements. If we use these elements in the window of the Specify flow assumption, we need to set the temperature equation to total energy and to have a better solution is needed to work on numerical tolerance. For these elements we have to define the initial conditions, but whereas the all degree of freedom is in centre of each element, is needed to create the element set (Meshing→Elements→Element Set). In this way all the elements are join in one group and is possible to give them the initial condition. Before this, is needed to set this possibility switching from Geometry to Geometry/Element (Control→Miscellaneous Options→and set "Geometry/Element" for the voice "ALE Boundaries and Special BC Defined on").

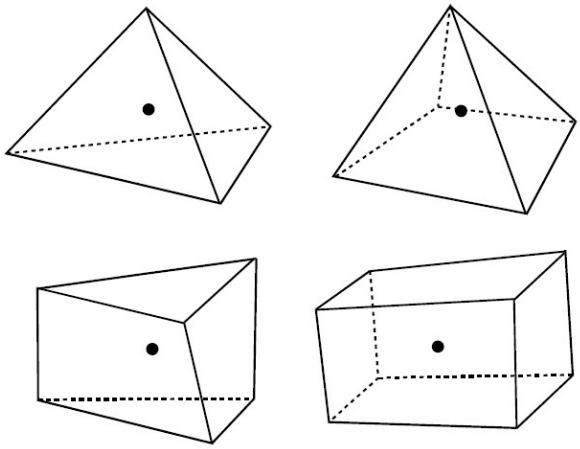

Fig. 98: FCBI-C elements

For the boundary condition, the program give us the possibility to define the SBC (Special Boundary Condition). We have defined two type of boundary condition:

- Wall: on the elements faces that are on the symmetry face. This condition doesn't give the possibility of the face to move in each direction.
- Fluid-Structure Interface: on the elements faces that are in contact with the structure part.

To apply this boundary is needed to create some Element-Face Set (Meshing→Elements→Elements-Face Set) for each face part of the fluid, and after is possible to define and apply the boundary on this Element-Face Set (Model→Special Boundary Condition).
About the oil elements, was create another "3d Fluid" group, with the same material of air, but setting the flow type inside the group as "Incompressible" to the behaviour of the oil like incompressible fluid.

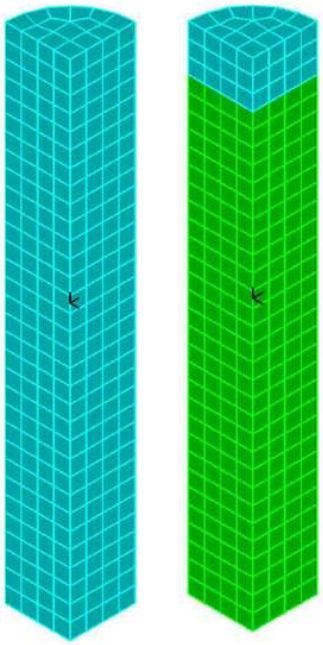

Fig. 99: One-quarter of cavity with air and oil - detail

4.3.2 FSI analysis: Temperature effect

To understand the pressure changes due to the temperature effect, we need to increase the temperature of 1 K. So, we want to change the temperature from the initial temperature from 273 K to the temperature of 274 K, in two specific case:

- When the cavity is empty: 100% of Air and 0% of Oil;
- When in the cavity is fill of oil: 9.37% of Air and 90.63% of Oil;

Before that, is needed to apply the load temperature of 274 K on both fluid and structure model. After the application of the load, to do the combined analysis is require generating the ADINA CFD and ADINA Structures data file. To do this, for both file (CFD and Structures) is needed to click the data file solution icon, make sure that the Run Solution button is unchecked and click Save.

After the previous passage is possible to do the FSI analysis (Solution→Run Adina FSI→Click the Start bottom→ then hold down the Ctrl key and select the Structure and CFD file→Then click Start).

From the theory point, when the cavity is fill of air, if I rise the temperature of 1 K, the pressure should be increase of the ratio of initial condition, that it is the coefficient of volume expansion of the air. This value is:

$$\frac{\text{Initial Pressure}}{\text{Initial Temperature}} = \frac{100000\ \text{Pa}}{273\ \text{K}} = 366\ \frac{\text{Pa}}{\text{K}}$$

So, for each temperature degree, the pressure should change of $\pm 366\ \text{Pa/K}$. In the same way, if I put the oil inside the cavity the volume of air reduces, but if I apply 1 K of temperature the initial condition and the coefficient of volume expansion of the air are the same of the situation of the cavity without oil. At the end, the variation of temperature should be always 366 Pa/K, because no matter how much the air volume is, but the important value is the coefficient of volume expansion.

The results using the FCBI or FCBI-C elements is very close, but the solution time with FCBI-C elements is very long. The following results has been obtained with FCBI elements.
How we can see from the following picture, with the empty cavity the pressure variation, applying the temperature load of 1 K, is 363 Pa instead 366 Pa. This result could be correct, because the temperature effect does increase the air pressure of 366 Pa, thanks to the coefficient of volume expansion, but the temperature load is applied also on the steel bar and cause an expansion of the bar as well. Obviously, the cavity follows the bar, and his volume inside became bigger than before, causing the little decrease of pressure to keep the equilibrium of the perfect gas law. This decrease of pressure in this case is calculated from the F.E.M model around 3 Pa, so the total increase of the pressure is 366-3=363 Pa.

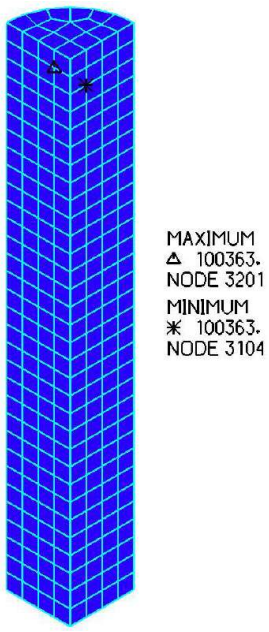

Fig. 100: Pressure inside the cavity with air due to a temperature effect

When the oil is inside the cavity, how we have explained before, the 1 K cause the increase of temperature of 366 Pa in the air, regardless how much is the air volume. But how we know the temperature load is applied also on the steel bar and it cause the expansion of the bar and of the cavity.
The expansion of the latter is the same of when the cavity is empty, but the volume of the air is only 9.37% of the cavity, instead of 100%. This involves, that decrease of pressure is much bigger than before. When we are in the elastic field, we have estimated in the chapter 4.2.2, that the variation of the pressure when the oil is in the cavity with a percentage of 90.63% is 10.67 time bigger than of 0% of oil. So, the decrease of pressure should be about 3*10.67=32.01 Pa. In the F.E.M model the decrease of pressure is 40 Pa, close for the theory consideration. So, the total decrease of pressure is 366-40=326 Pa.

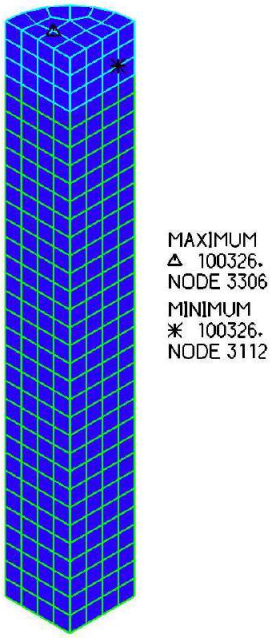

Fig. 101: Pressure inside the cavity with air and oil due to a temperature effect

Considering a range of temperature between 10°C (283 K) to 30°C (303 K), is possible to plot the pressure variation due to temperature effect with and without incompressible fluid. Both trends are linear, but the angular coefficient is different due to a presence of the oil. The different between angular coefficients is 363-326=37 Pa.

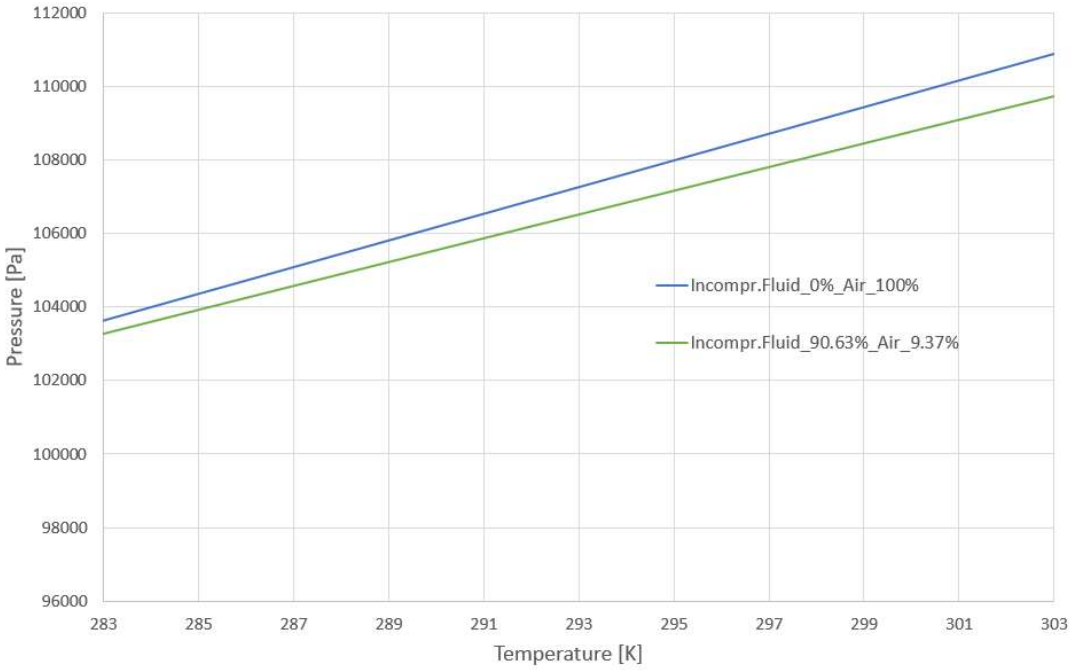

Figure 102: Trend of pressure variation due temperature effect

4.4 Effect of Temperature with mechanical action

In the previous chapter we have analyzed the mechanical action and temperature effect, separately. In this part we will try to study these effects together to understand if is possible to separate the variation of pressure inside the cavity due to a temperature effect and due to a mechanical action. To do this analysis, we have done an FSI analysis, using the same model described before, applying both and together the temperature and pressure load.

- Temperature load: in the steel bar inside the concrete is more difficult to reach a temperature of 0 °C (273 K). So, the choice about the range of temperature to apply of our model is between 10°C (283 K) to 30°C (303 K);
- Pressure load: to see the effect of the mechanical action, we have applied on our model different range of pressure load, in a range from 0 MPa to 400 MPa.

This load has been applied before when the cavity was empty (100% Aria – 0% Olio) and after with the oil inside the cavity (9.37% Aria – 90.63% Oil). In the following picture, we can see the effect of the load and temperature together when the cavity is empty. How we can see the trend for each pressure load is linear and all the lines are parallel.

The temperature affects only the angular coefficient, that is about 363 Pa, namely the variation of pressure due of one degree of temperature change. The main problem in this case, is the difficult to divide the temperature effect from the pressure load effect, because all the lines are very close, and the range of pressure variation is very tight.

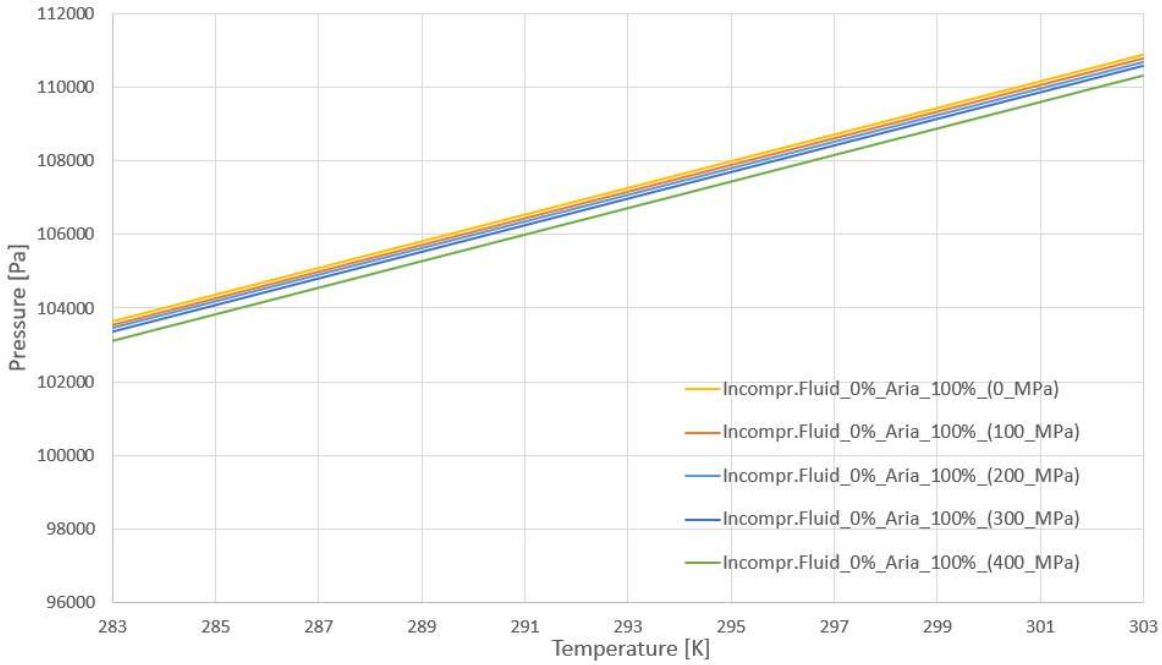

Fig. 103: Temperature and Mechanical action with empty cavity

Instead, when inside the cavity there is the incompressible fluid, the situation is different. How we can see from the following picture, the lines of different pressure loads are always parallel, and the angular coefficient is about 326 Pa, little lower then when the cavity is empty, due to presence of the oil, how we have explained in the previous chapter. We can see the really benefit of the oil that allow to separate the pressure load effect from the temperature effect. This effect is amplified when the bar is near to the plastic field, because the volume of the cavity became more larger caused from big deformation and with the oil, the pressure change is very big, how happen with the jump of 400 MPa.

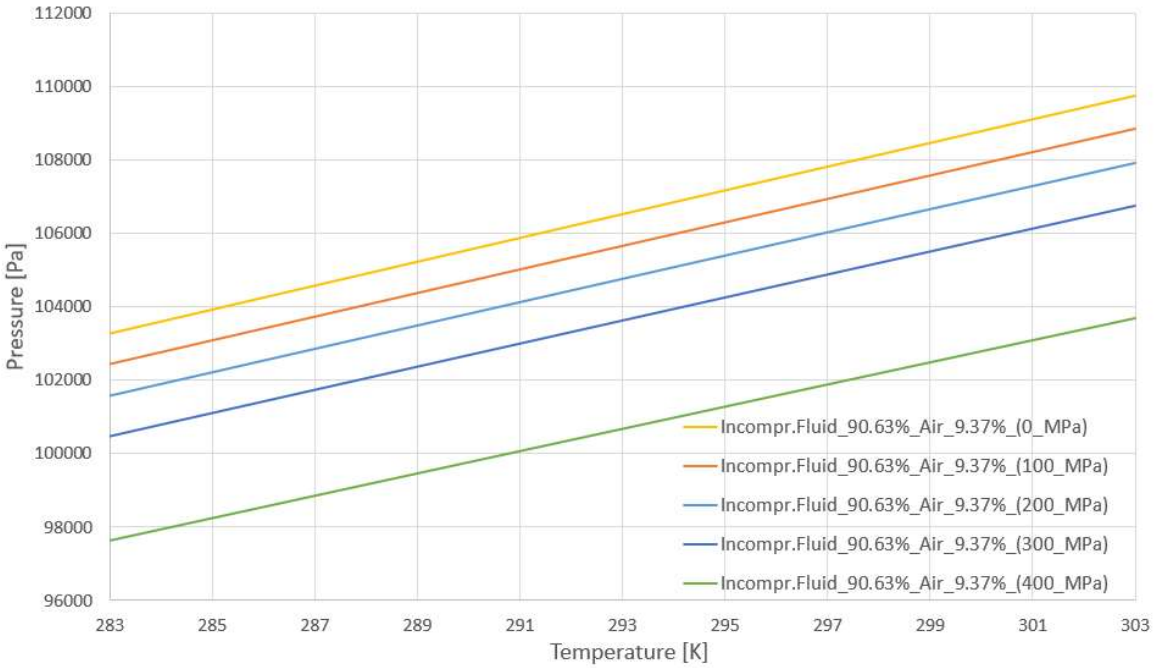

Fig. 104: Temperature and Mechanical action with oil inside the cavity

Chapter 5
5. Experimental study

In this chapter we are going to analyze the "S3 system" in a “smart” steel bar by means of a complete experimental study to understand the pressure variation due to a temperature effect. This experiment was made with only air inside the cavity; so, in the following part we will compare the results obtained from the numerical part with the results obtained from the experimental data.

Experimental setup

To analyze the pressure and temperature variation, we have considered a 50 cm segment length of “smart” steel bar equipped with three sensors of S3 System.

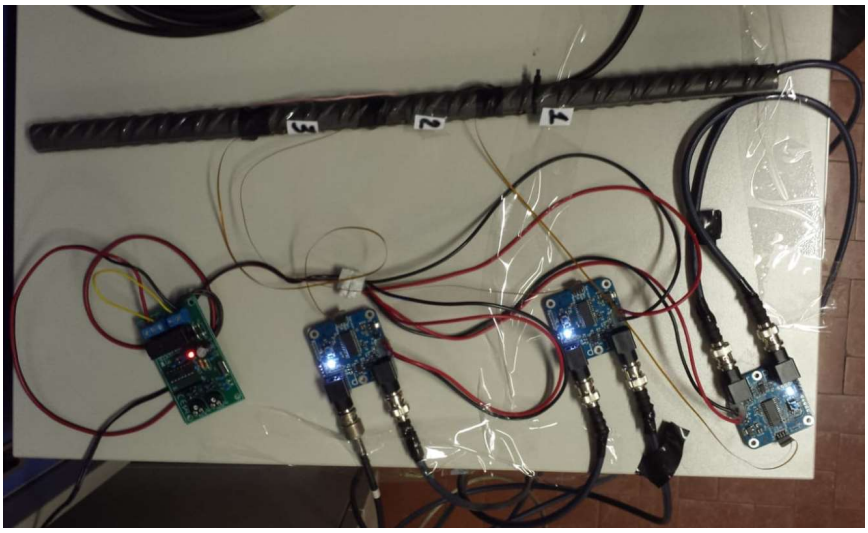

Fig. 105: Acquisition system

The bar is subjected only to ambient temperature variation in a non-controlled environment, to control the pressure and temperature variation during the day. Each sensor is completely sealed in the cavity. The sensors are connected with a soft PCB (Printed Circuit Board), to the external board, that is a digital to analog converter (DAC). These boards must be powered and in turn supply the sensor by acquiring data from the sensor itself. Is possible to interrogate these boards individually or simultaneously thanks to the use of a BNC cables. So, the signals are acquired through BNC connection from the National Instrument board (NI 6001).

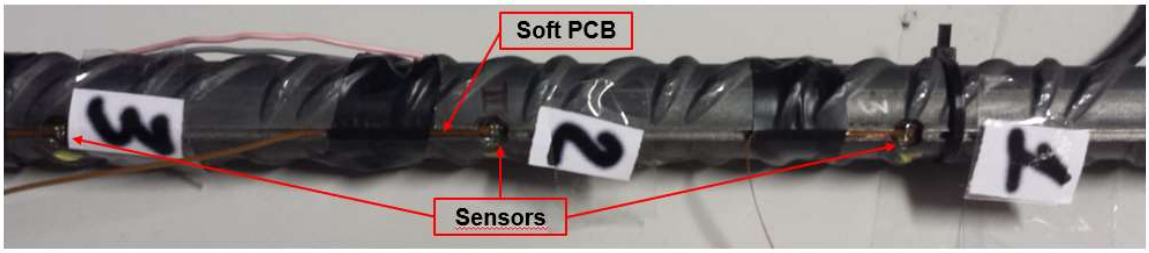

Fig. 106: “Smart” steel bar equipped with three sensors - detail

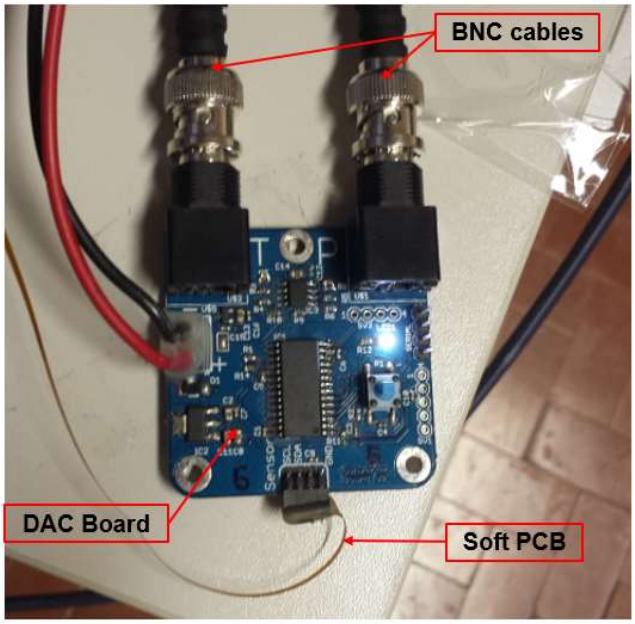

Fig. 107: Digital to analog converter board (DAC) - detail

We have used the VM188 board of Valleman Modules, that is require a power supply but is able to active the system in a determinate range of time. We have done two types of acquisition:

- one minutes each hour;
- ten minutes each hour.

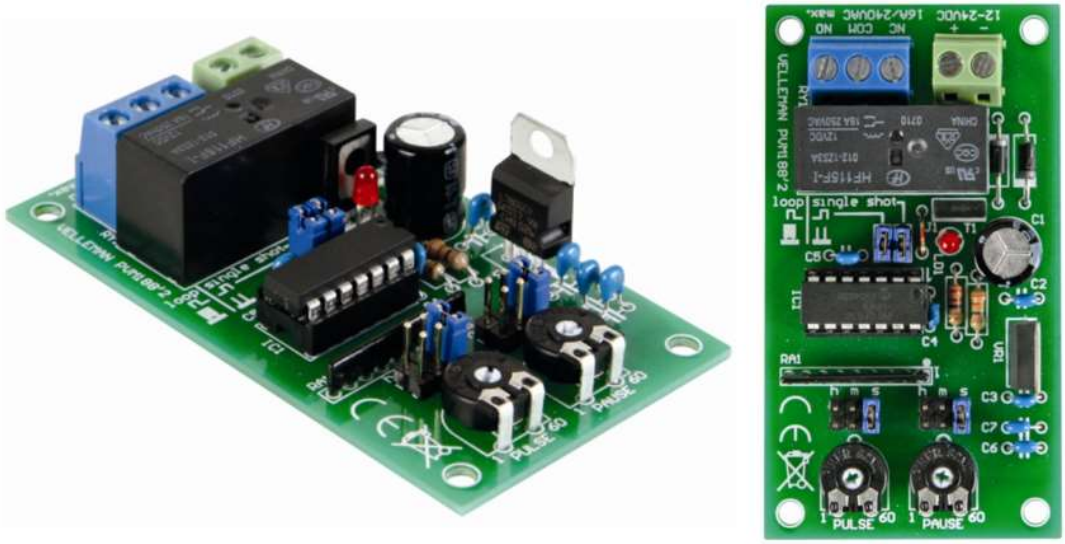

Fig. 108: VM188 board - detail

We have used MATLAB, where inside there is a very large reading window, in which the activation of the boards through the VM188 has been synchronized. What happens is, that the VM188 turns on in the range of interest and turns on the whole system, acquiring signals, until the system is turned off. During this procedure, MATLAB acquires data in Volts before the system is turned on, when the system is on and after when the system is turned off.

To take the part of the signal when the system is turned on, the whole signal is treated on MATLAB and the part where the Volts have a very low value is cut off, meaning that at that time there was no acquisition in progress. In the following picture is possible to see one acquisition of ten minutes and the relative interesting part with the pressure and temperature Volt value around 5.

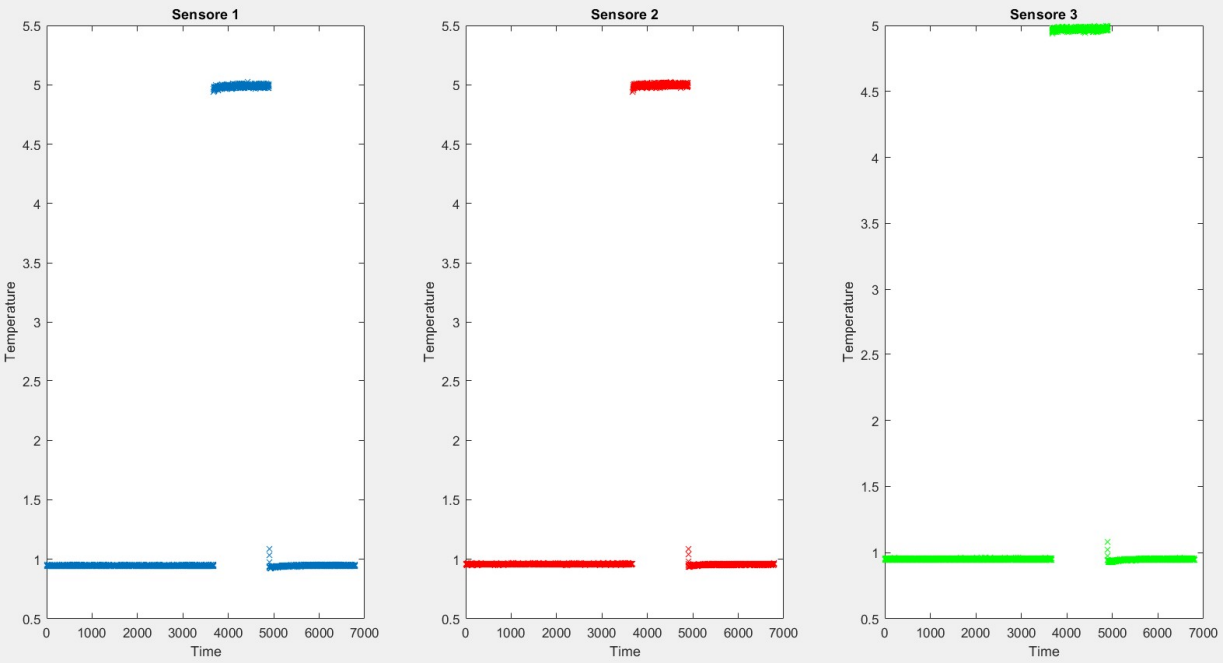

Fig. 109: Temperature value in Volt over time of three sensors for a single ten minutes acquisition

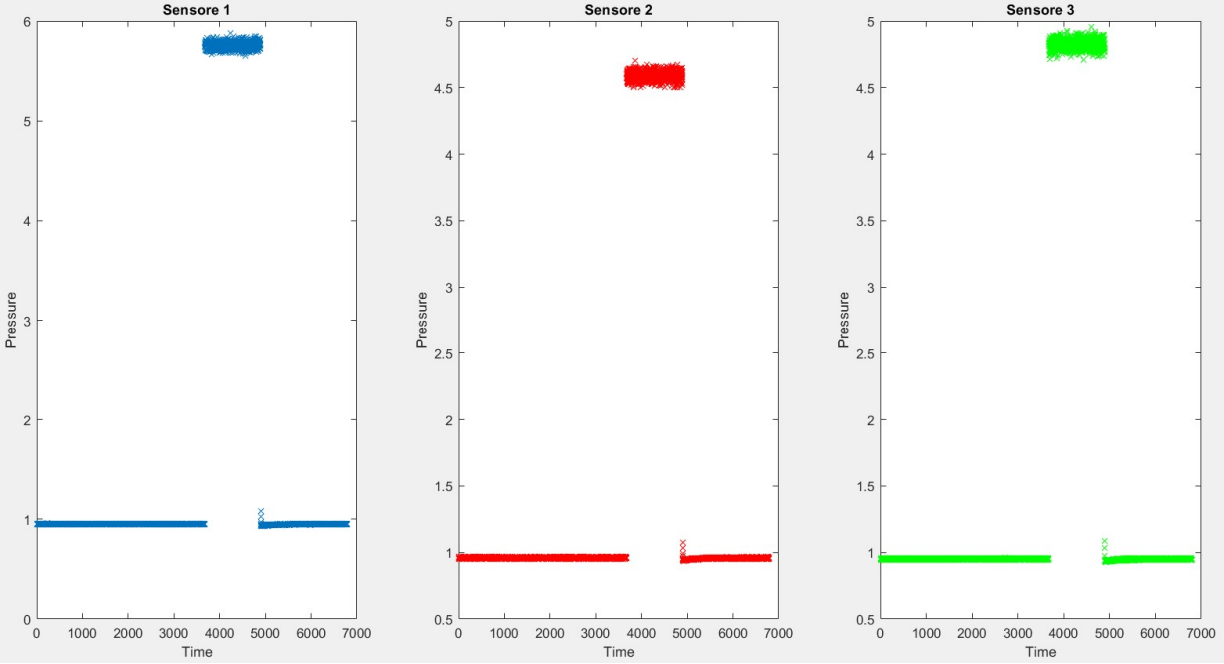

Fig. 110: Pressure value in Volt over time of three sensors for a single ten minutes acquisition

We have applied a third-order one-dimensional median filter to the input vector of each acquisition and a mobile average of hundred following values, to have a cleaner signal.

Is needed to change the output in Volt to Pascal and Kelvin. To do this is necessary to have the initial temperature and pressure value inside the cavity, before to begin the experiment, namely in the moment that the cavity is sealed; these values are the following:

P1 = 97163 Pa	T1 = 23.2 °C	T1 = 296.35 K
P2 = 80311 Pa	T2 = 23.2 °C	T2 = 296.35 K
P3 = 78528 Pa	T3 = 23.1 °C	T3 = 296.25 K

5.1 Ten minutes acquisition

The measurement system has been set to catch the data of temperature and pressure from each sensor for ten minutes each hour during the day, with a frequency of 2 Hz. Totally we have analyzed 426 acquisition.
Graphing the variation of pressure due to a variation of temperature, we have done a liner regression of the data to understand how much the pressure variation due to temperature effect is, namely the angular coefficient of the trend.

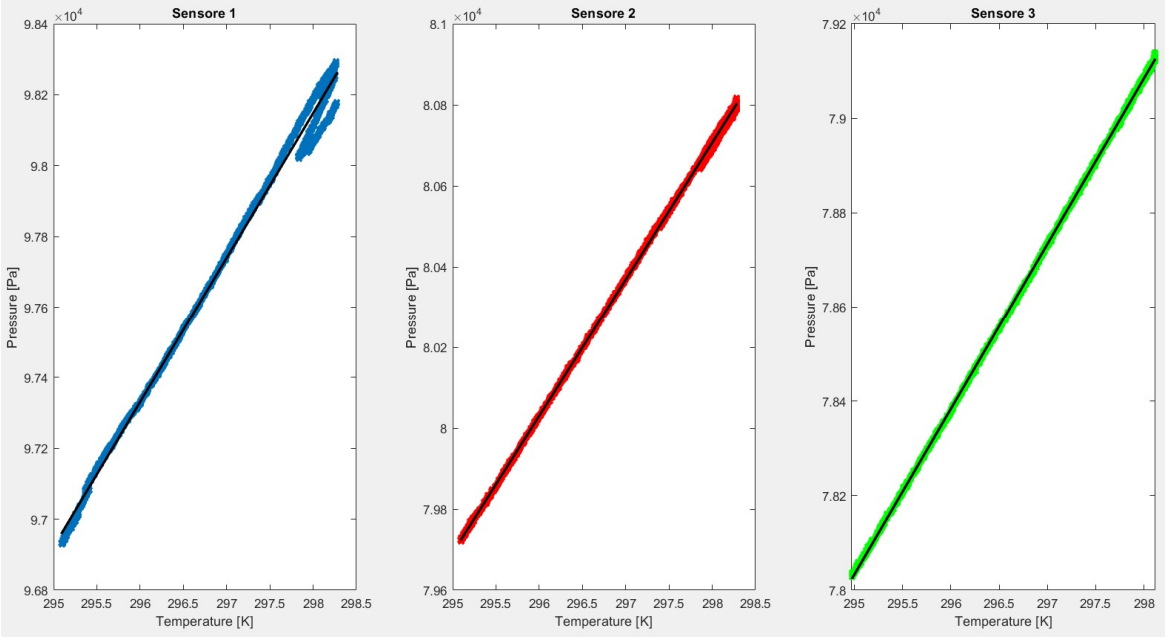

Fig 111: Trend Temperature - Pressure over time (600 seconds)

Sensor 1	Y = **408.63***X + 87993.60	Variation of **408.63** Pa for each Kelvin
Sensor 2	Y = **338.31***X + 72299.62	Variation of **338.31** Pa for each Kelvin
Sensor 3	Y = **350.44***X + 70376.03	Variation of **350.44** Pa for each Kelvin

From the numerical result, when in the cavity there is only air, we have obtained a value of pressure change for each Kelvin of 363 Pa. The angular coefficient from the experimental results from the sensor number two and three is close to the numerical result and the different is probably due to a dispersion of the data; but the trend is linear as in the numerical model. In the latest acquisitions we can see that the temperature has risen and then it has fallen again.

Theoretically, for each degree of temperature should be correspond a precise value of pressure and everything should be on the same line; but working with real devices, which have errors, some hysteresis is born, and we don't have a perfect straight line.

Only for the first sensor we have a big different, and the acquisition data does not allow us to make a compare from numerical result and probably is due to a not perfectly sealed of the system inside the cavity. Indeed, the hysteresis is more accentuated, and the angular coefficient is more different than the other sensors.

Is possible to obtain the cavity volume variation, using the perfect gas law as follow:

$$P_0 \cdot V_0 = n \cdot R \cdot T_0 \qquad (P_0 + \Delta P) \cdot (V_0 + \Delta V) = n \cdot R \cdot (T_0 + \Delta T)$$

doing the ratio between this equation we obtain the percentage variation of the volume.

$$\frac{P_0 + \Delta P}{P_0} \cdot \frac{V_0 + \Delta V}{V_0} = \frac{T_0 + \Delta T}{T} \rightarrow \left(1 + \frac{\Delta P}{P_0}\right) \cdot \left(1 + \frac{\Delta V}{V_0}\right) = \left(1 + \frac{\Delta T}{T_0}\right)$$

$$\frac{\Delta V}{V_0} = \frac{\left(1 + \frac{\Delta T}{T_0}\right)}{\left(1 + \frac{\Delta P}{P_0}\right)} - 1$$

The results are reported in the following pictures.

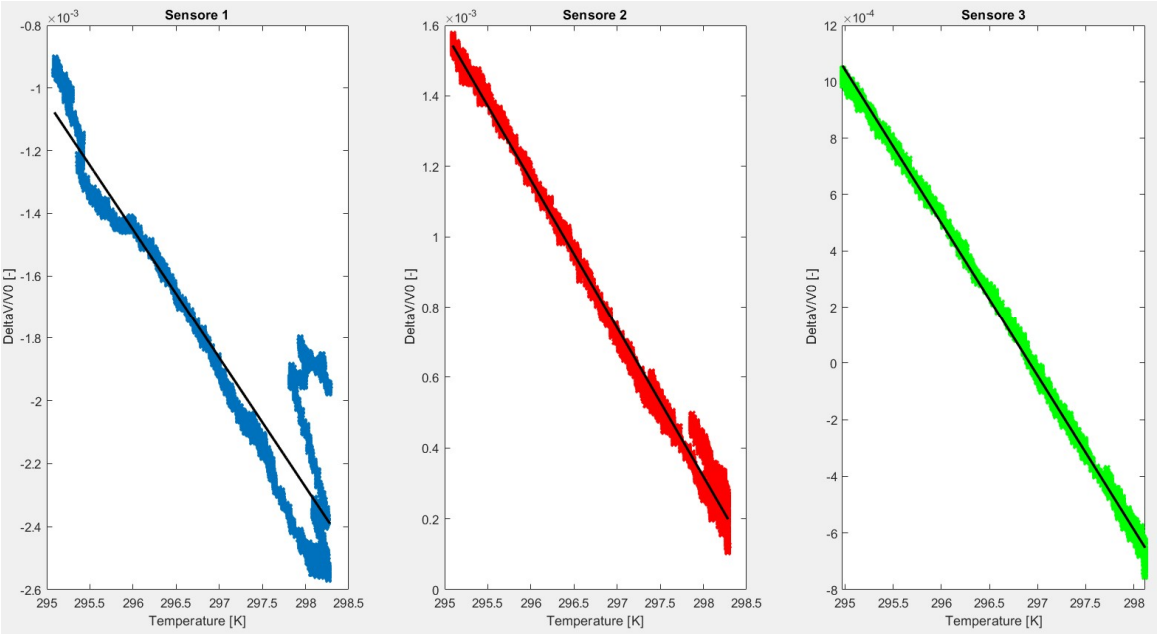

Fig. 112: Trend Temperature - Volume variation over time (600 seconds)

Sensor 1	Y = - **0.00041***X + 0.120
Sensor 2	Y = - **0.00042***X + 0.125
Sensor 3	Y = - **0.00054***X + 0.161

How we can see the trend is linear and the angular coefficient is negative. This is correct because, following the perfect gas law, we have seen that when the temperature increases the pressure raise as well, but to maintain the equilibrium of the law, the volume must decrease.

In the following picture we can see the trend of $\Delta V/V$ obtained in the previous campaign (Tondolo, 2018) in the controlled environment, where the temperature has been change from -20°C to 20°C. The trend is not linear but is possible to see it only with the big range of temperature variation. However, if we consider the temperature variation between 10°C to 20°C in Fig.113, obviously the range of temperature is no the range that we have in Fig. 112, but the trend in this zone is similar.

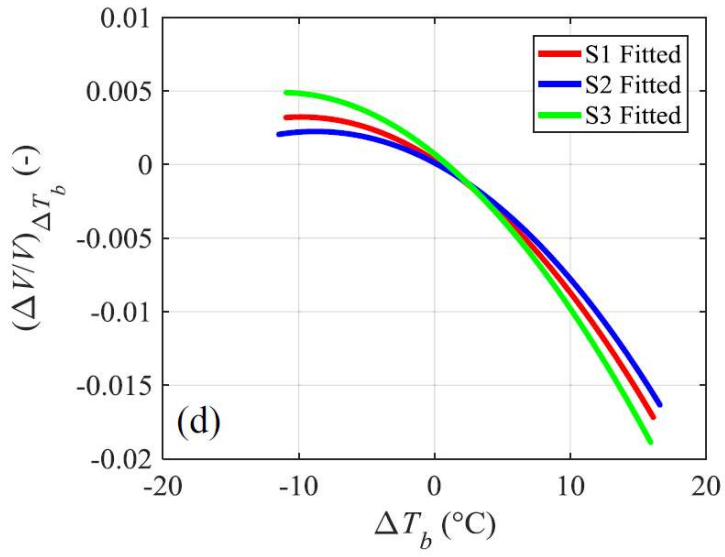

Fig. 113: Graph of Temperature - Volume variation of previous campaign (Tondolo, 2018)

In the following pictures is report the trend of pressure and temperature variation over time. Is possible to notice that the trend has the same form for both, due to following the perfect gas law.

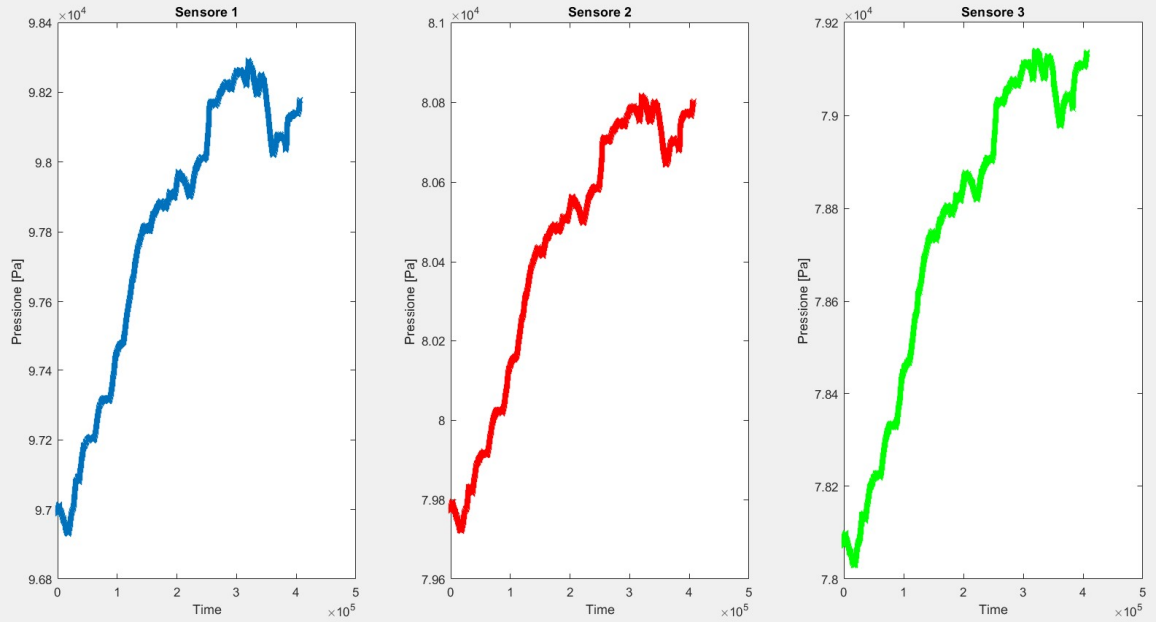

Fig. 114: Pressure variation over time of three sensors

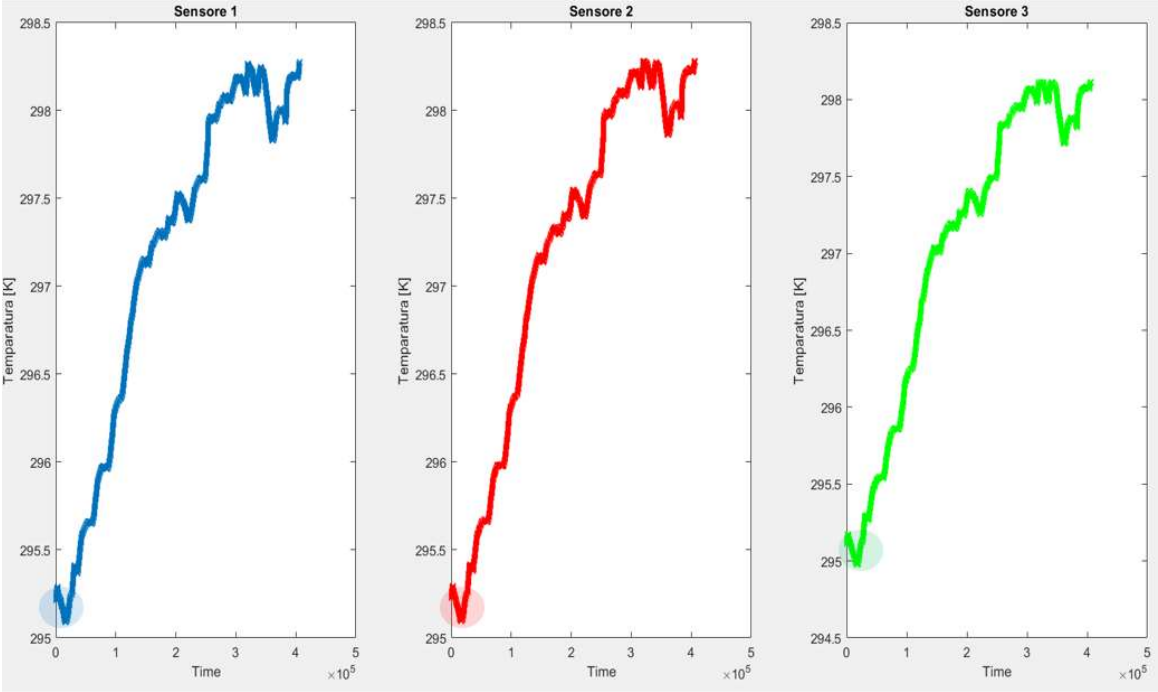

Fig. 115: Temperature variation over time of three sensors

Consider only a little part of the acquisition (circle part of the Fig.115) is possible to notice better that at the beginning of each acquisition we have a raise of temperature for few seconds, and after the trend become almost constant (Fig. 116). This is due probably to the overheating of the MEMS sensor during its switching on. So, we have evaluated how much the increase of temperature is, doing the difference between the average of the last 30% data of the acquisition and the lowest value of the temperature, that should be at the beginning of the acquisition.

From the analysis we have seen that the maximum raise of temperature is about 0.02 K. So, there isn't a big variation of temperature and this doesn't affect the pressure variation.

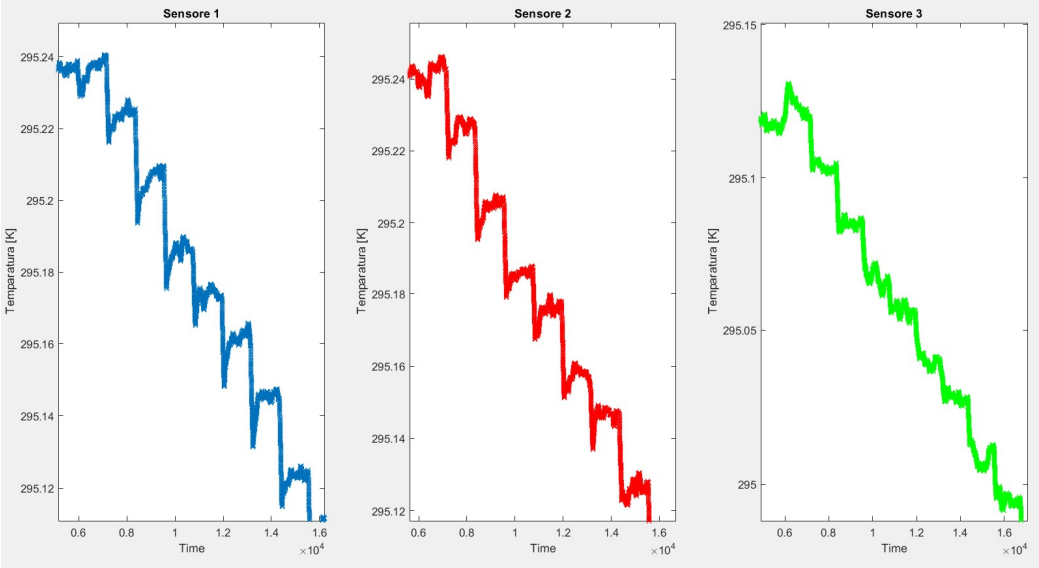

Fig. 116: Temperature variation over time of three sensors – zoom of some acquisitions

5.2 One minute acquisition

The measurement system has been set to catch the data of temperature and pressure from each sensor for one minute each hour during the day, with a frequency of 10 Hz. Totally we have analyzed 310 acquisition.

The results are very similar to the previous acquisitions of ten minutes, but how we have explained in the previous chapter, only in the first sensor the results aren't correct.

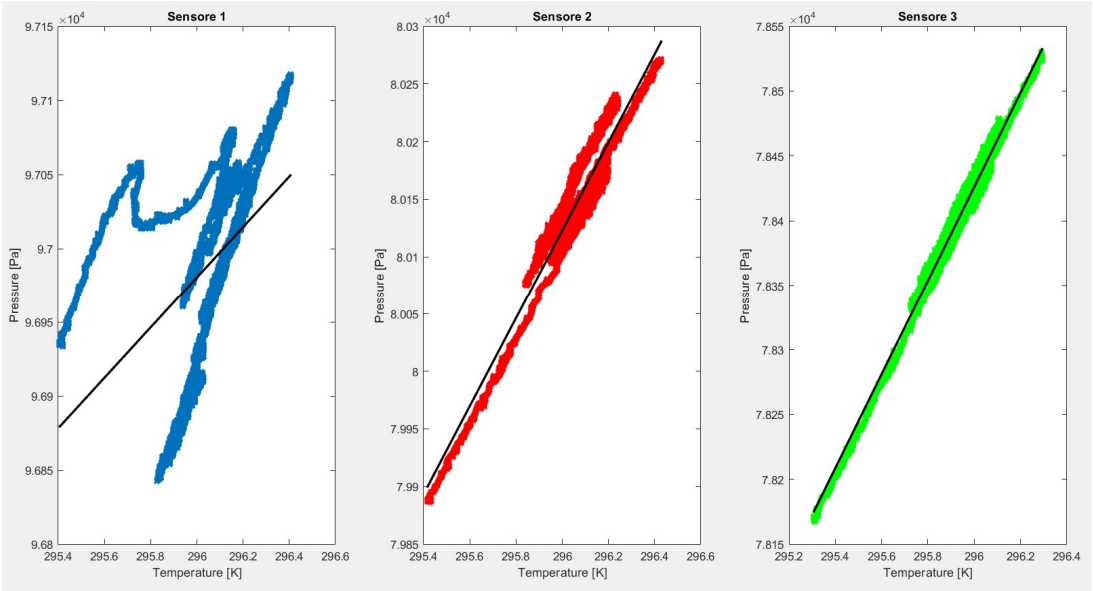

Fig. 117: Trend Temperature - Pressure over time (60 seconds)

Sensore 1	Y = 170.41*X + 93086.68	Variation of 170.41 Pa for each Kelvin
Sensore 2	Y = 382.41*X + 71384.72	Variation of 382.41 Pa for each Kelvin
Sensore 3	Y = 362.72*X + 70138.10	Variation of 362.72 Pa for each Kelvin

How we can see from the result the trend of the sensor number 2 and 3 is correct, and the angular coefficient of sensors 3 is almost egual to 363 Pa from the numerical result.

As before, is possible to obtain the cavity volume variation, using the follow expression:

$$\frac{\Delta V}{V_0} = \frac{\left(1 + \frac{\Delta T}{T_0}\right)}{\left(1 + \frac{\Delta P}{P_0}\right)} - 1$$

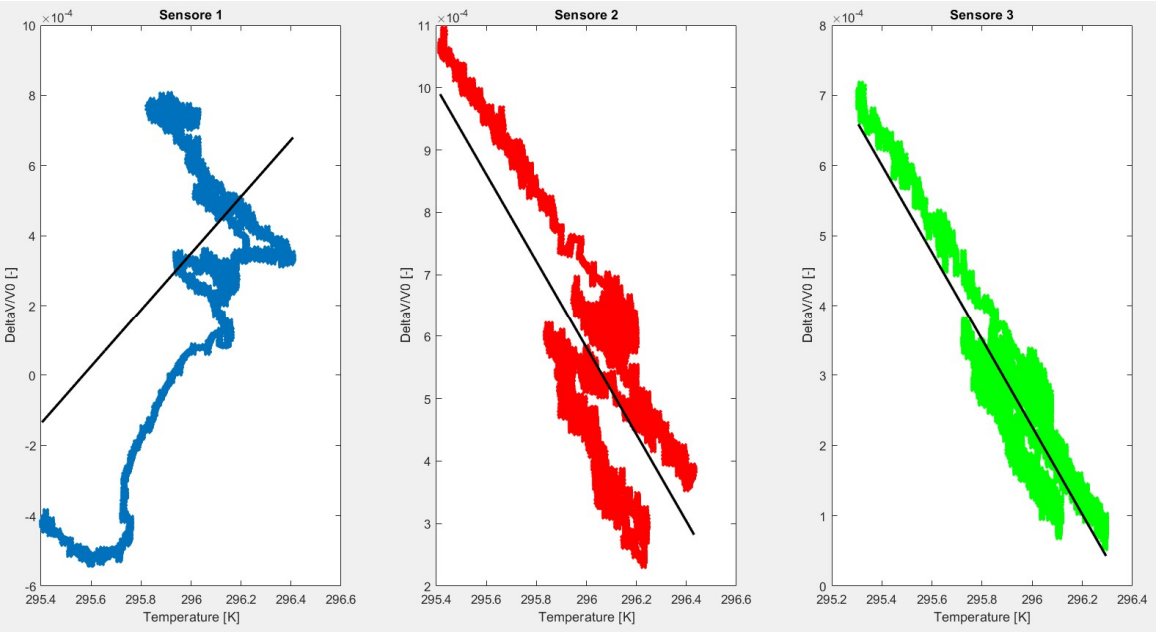

Fig. 118: Trend Temperature - Volume variation over time (60 seconds)

Sensore 1	Y = + **0.00081***X - 0.239
Sensore 2	Y = - **0.00069***X + 0.206
Sensore 3	Y = - **0.00062***X + 0.184

Is possible to see the wrong trend of the first sensor. Instead the trend of the other sensor could be correct and they are similar.

In the following pictures we have plotted the pressure and temperature variation trend, over time. How in the ten minuts acquisition the trend has the same form, following the perfect gas law.

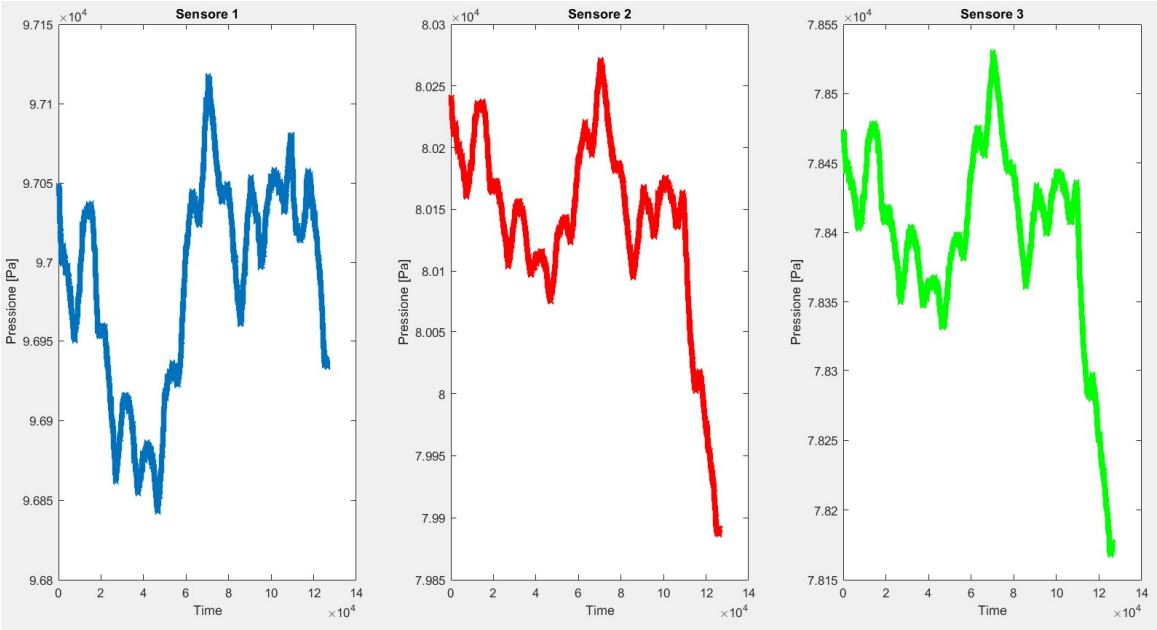

Fig. 119: Pressure variation over time of three sensors

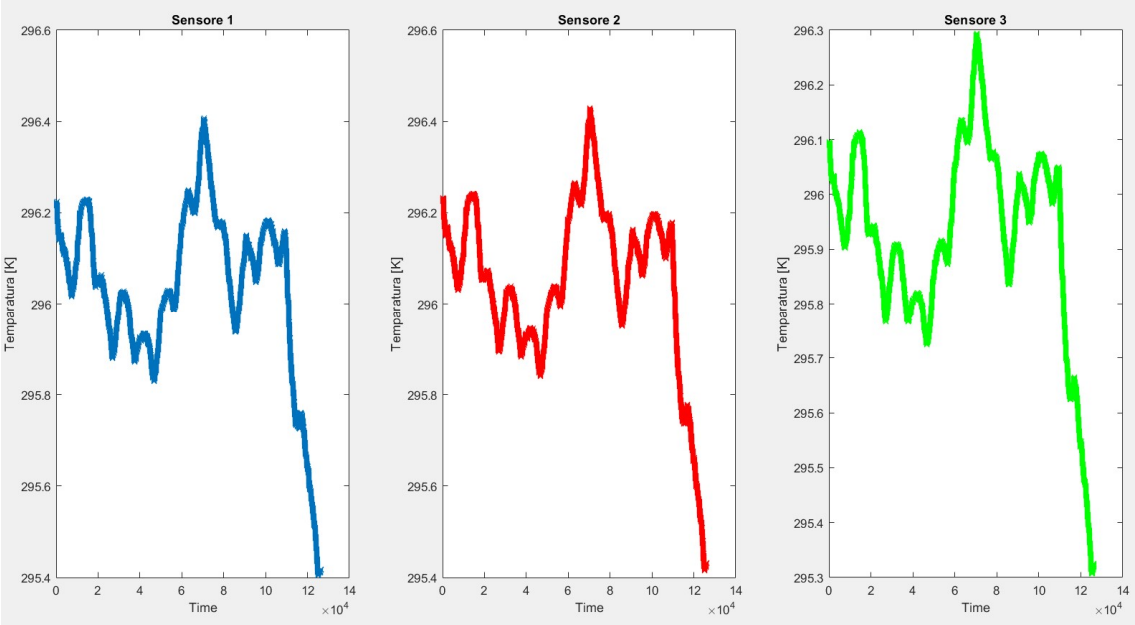

Fig. 120: Temperature variation over time of three sensors

Conclusions

The “S3 System” is one of the new smart technology, under study, for structural health monitoring. In this master thesis, numerical and experimental test have been made to further its development. We have reported a summary of the results.

The “S3 System” consists in a classic steel bar for reinforced concrete, with a circular cavity obtained as a transversal drilled hole, filled with a fluid and hosting an ordinary low-cost embedded Micro Electro-Mechanical Systems (MEMS) sensor. The cavity is a discontinuity on the steel bar. Thanks to the numerical study, we have evaluated the stress intensity factor (Kt), trying to understand how much the stress increase near the hole is. We have seen from the numerical result, that the highest value of Kt is when the hole is circular; but stretching one of the axes of the hole from circular to elliptical form the Kt value goes down, according with theory consideration. We have seen that with the hole slotted of 2 mm, the Kt value could reduce itself of about 30%. These results are good because the steel bar is no perfectly smooth bar, but on his surface, it has some ribs distributed along the entire length. These ribs made an increase of stress, but the value of Kt due to these discontinuities is close the Kt value due to the hole, once it is slotted.

The S3 System can read the deformation of the steel bar, measuring the pressure change inside the cavity. So, we have analysed the pressure inside the air to improve the sensibility of the system. Indeed, the MEMS inside the cavity is able to read pressure and temperature change, but the minimum value of pressure variation that can read is 1 Pa. To have a good resolution, is necessary that the system could see με variation on the steel bar. So, it is needed that we have at least a variation of 1 Pa each με on the steel bar. Therefore, in order to improve the sensibility, it is assumed to fill the cavity with a percentage of incompressible fluid to raise the variation of pressure during a mechanical action. From the numerical model results, we observed that the required sensibility is reached filling the cavity with the incompressible fluid at least of 77.50% of the total volume of the cavity.

Analysing the pressure change due to temperature effect, theoretically it makes a linear pressure change of 366 Pa. From the numerical result, with or without the presence of the incompressible fluid, the pressure variation due to temperature effect is within the range of 326-363 Pa. This result is good because without the incompressible fluid the pressure change due to a mechanical action is very similar to a pressure change due to a temperature variation, so is very difficult to split the two effects; instead the presence of the incompressible fluid in the cavity is beneficial to increase the sensibility only in presence of a mechanical action, allowing to lower temperature rate from the response of the system temperature effect. The numerical result of pressure changes due to temperature effect, when the cavity is empty, are compared with the experimental result obtained from the campaign of measure where one “smart” bar is subjected only to ambient temperature variation in a non-controlled environment. From the comparison, is possible to observe that the numerical model works properly, and its results are close to the experimental outputs.

Bibliography

Abuella H. An Innovative Implementation of Visible Light Sensing for Quantifying the Dynamic Response of Bridge Girders [Journal]. - 2019.

Battistoni Francesco Nerio Structural Health Monitoring using low cost sensors: experimental and numerical study [Journal]. - 2018.

Ceylan Halil A Feasibility Study on Embedded Micro-Electromechanical Sensors and Systems (MEMS) for Monitoring Highway Structures [Journal]. - 2011.

Dutta Susom A Review of Fiber Optic Sensing Technologies for Bridge Health Monitoring [Journal]. - 2019.

Geokon [Online] // https://www.geokon.com/. - 2020.

Hou S. A PZT-based smart aggregate for compressive seismic stress monitoring [Journal]. - 2012.

Inaudi D. Fiber Optic Sensors for Structural Health Monitoring [Conference]. - 2017.

Lezgy-Nazargah M. Design and fabrication of a new fiber-cement-piezoelectric composite sensor for measurement of inner stress in concrete structures [Journal]. - 2019.

Liu Tiejun Research on Piezoelectric Monitoring Method of Working Stress of Concrete Structures [Journal]. - 2019.

Nagayama Tomonori Structural Health Monitoring Using Smart Sensors [Journal]. - 2007.

Nunes Marina Rocha Pinto Portela Material and geometrical characterisation of quenched and self-tempered steel reinforcement bars [Journal]. - 2014.

Olivera Jesús An Embedded Stress Sensor for Concrete SHM Based on Amorphous Ferromagnetic Microwires [Journal]. - 2014.

Pochettino O. Infrastructural Internet-of-things Using Quasi-self-powered Structural Health Monitoring Sensors [Journal]. - 2019.

Rácz Zoltán Soft elastomeric capacitive sensor for structural health monitoring [Journal]. - 2016.

Rainieri C. Issues in SHM of existing bridges: from periodic checks to continuous structural health and performance assessment [Journal]. - 2019.

Smartec [Online] // https://smartec.ch/en/. - 2020.

Taheri Shima A review on five key sensors for monitoring of concrete structures [Journal]. - 2019.

Tondolo F Embedded system for measurements of strain/stress in one-dimensional elements. Patent n° 102016000118077, Italy [Patent]. - 2016.

Tondolo F. Smart reinforcement steel bars embedded with low-cost MEMS sensors for strain monitoring [Journal]. - 2017.

Tondolo F. Smart reinforcement steel bars with low-cost MEMS sensors for the structural health monitoring of RC structures [Journal]. - 2018.

Ye Xijun An Improved Step-Type Liquid Level Sensing System for Bridge Structural Dynamic Deflection Monitoring [Journal]. - 2019.